Engineered microwave control for trapped ions

Von der Fakultät für Mathematik und Physik der
Gottfried Wilhelm Leibniz Universität Hannover

zur Erlangung des Grades

Doktor der Naturwissenschaften
- Dr. rer. nat. -

genehmigte Dissertation von

Dipl.-Ing. Martina Wahnschaffe geb. Carsjens

2016

Referent:	Prof. Dr. Christian Ospelkaus Institut für Quantenoptik, Hannover
Korreferent:	Prof. Dr. Piet Oliver Schmidt Institut für Quantenoptik, Hannover
Tag der Promotion:	03.06.2016

Abstract

This thesis describes concepts and models, numerical simulations and experiments in the field of quantum information processing with trapped ions. While in typical ion-trap experiments, focused laser beams are used to implement quantum logic operations, this thesis is concerned with direct microwave control of atomic hyperfine qubits in a near-field approach. Here, the control fields originate from conductors embedded into a scalable trap structure. This approach holds the potential to implement high-fidelity quantum logic operations because of superior classical control, relaxed cooling requirements, the elimination of spontaneous emission as a fundamental source of decoherence and because of the integration of the control mechanism into a scalable microstructure. In order to realize the elementary operation of multi-qubit quantum logic (the motional sideband transition), the near-field approach requires an oscillatory microwave field which exhibits a large spatial amplitude gradient and only a small oscillatory offset field at the location of the ion(s). Here, I describe how a single meander-shaped microwave electrode is able to provide the aforementioned field configuration. Such a field configuration can be fully described using five parameters, which characterize the strength and orientation of the zero and first order terms of the near-field, as well as its polarization. The ratio of the strength of the zero to first order terms describes the ratio of carrier to sideband transition Rabi rates, similar to a Lamb-Dicke parameter in the laser-based approach. Thus, it can be used to optimize the design of the meander-shaped electrode integrated in a trap structure. The design is obtained using state-of-the-art full-wave numerical simulations performed with Ansys HFSS. The simulations precisely model the current distribution in all trap electrodes, accurately accounting for proximity and skin effects. This design is optimized for addressing a field-independent transition in $^9Be^+$ at about 1 GHz. Furthermore, this thesis presents an experimental setup to trap and manipulate ions in surface-electrode ion traps. It describes the implementation of a field-independent qubit for long coherence times, as well as a calibration trap used for validating simulations. Here, a single $^9Be^+$ ion is used as a high resolution quantum sensor to measure the magnetic field distribution through energy shifts induced in the hyperfine structure of its ground state. The comparison with simulations shows an agreement at the sub-micron and few-degree level. Finally, recent work on an evolved trap design and the development of a multi-layer trap with integrated near-field control is discussed. Both designs benefit from the results obtained in this work.

Keywords: Quantum information processing, trapped and laser-cooled ions, hyperfine qubits, microstructures, microwave near-fields

Zusammenfassung

In dieser Arbeit werden Konzepte und Modelle sowie numerische Simulationen und Experimente im Bereich der Quanteninformationsverarbeitung mit gespeicherten Ionen diskutiert. Während die Implementierung von Quantenlogikoperationen typischerweise anhand fokussierter Laserstrahlen erfolgt, befasst sich diese Arbeit mit der direkten Kontrolle von Qubits in atomaren Hyperfeinzuständen mittels der Mikrowellen-Nahfeldmethode. Die notwendigen Kontrollfelder werden von integrierten Leitern in einer skalierbaren Fallenstruktur erzeugt. Aufgrund der hervorragenden Kontrollierbarkeit von Mikrowellenfeldern, verringerter Kühlanforderungen, der Vermeidung von spontaner Emission als einer fundamentalen Dekohärenzquelle und der Integration der Kontrollmechanismen in skalierbare Mikrostrukturen birgt dieser Ansatz das Potential, Quantenlogikoperationen mit geringer Fehlerrate zu implementieren. Zur Realisierung der elementaren Multi-Qubit-Logikoperation (des Bewegungsseitenbandübergangs) benötigt die Nahfeldmethode ein oszillierendes Mikrowellenfeld, welches eine möglichst große räumliche Inhomogenität und nur ein geringes Restfeld am Ort des Ions aufweist. Diese Feldkonfiguration kann, wie hier beschrieben, mit einer einzelnen Elektrode in Mäandergeometrie erzeugt werden und lässt sich mittels fünf Parametern vollständig beschreiben. Die Parameter charakterisieren die Stärke und Orientierung der nullten und ersten Ordnung des Nahfeldes, sowie dessen Polarisation. Das Verhältnis der Stärken von nullter und erster Ordnung beschreibt hier das Verhältnis der Rabi-Frequenzen von Träger- zu Seitenbandübergängen und ist vergleichbar mit dem Lamb-Dicke Parameter im laserbasierten Ansatz. Es kann daher für die Optimierung der Mäandergeometrie, welche in die Fallenstruktur integriert ist, genutzt werden. Elektromagnetische numerische Simulationen, welche die Stromverteilung in den Fallenelektroden unter Berücksichtigung des Skin- und des Proximity-Effektes genau modellieren, werden mit Ansys HFSS zur Bestimmung der Elektroden-Geometrien verwendet. Diese wird für die Adressierung eines feldunabhängigen Überganges in $^9Be^+$ bei ungefähr 1 GHz optimiert. Diese Arbeit stellt außerdem den experimentellen Aufbau zum Fangen und Manipulieren einzelner Ionen in einer Oberflächenfalle, die Implementierung eines feldunabhängigen Qubits für lange Kohärenzzeiten sowie eine Kalibrierungsfalle zur Validierung der numerischen Simulationen vor. Ein Mikrowellenmagnetfeld verschiebt die Energieniveaus in der Hyperfeinstruktur des Grundzustandes, welche mittels eines einzelnen $^9Be^+$-Ions als hochauflösendem Quantensensor räumlich vermessen werden. Der Vergleich von Messung und Simulation weist eine Übereinstimmung im Sub-μm-Bereich auf, die zugehörigen Winkel weichen nur um wenige Grad ab. Als Ausblick werden jüngste Fortschritte in Richtung eines neuen Fallendesigns sowie die Entwicklung einer Mehrlagenfalle mit integrierter Nahfeldkontrolle aufgezeigt. Beide Entwürfe profitieren von den Resultaten dieser Arbeit.

Schlagwörter: Quanteninformation, gefangene und lasergekühlte Ionen, Mikrostrukturen, Mikrowellen-Nahfelder

Contents

Chapter 1

Introduction

Studying quantum many-body physics is one of the most challenging tasks towards a deeper understanding of fundamental physics. The complexity of interacting many-body systems impairs the simulation of such systems on classical computers in full generality. Even supercomputers run into fundamental limitations simulating a system with some tens of spins in full generality. To solve a problem with about 250 spins for example, a classical computer would require a huge amount of bits which surpasses the amount of protons in the universe. In general, the complexity of solving many-body physics problems increases exponentially with N, where N is the number of particles involved [1]. In 1982, Richard Feynman already suggested to study complex quantum many-body systems using a well controlled quantum system [2]. These pioneering ideas have evolved into the general concept of a quantum computer, where the elementary unit of information is the quantum bit, abbreviated qubit, which is a quantum-mechanical two-level system. If certain criteria, known as the DiVincenzo criteria [3] are fulfilled, any classical and quantum problem can be solved as a sequence of quantum operations. These criteria are:

- A scalable physical system with well-characterized qubits
- The ability to initialize the state of the qubits to a simple fiducial state, such as $|000...\rangle$
- Long relevant decoherence times, much longer than the gate operation time
- A "universal" set of quantum gates
- A qubit-specific measurement capability

If the quantum computer is extended by adding the possibility to transmit the information to different places, as is necessary for quantum communication, two additional criteria are added [3]:

- The ability to interconvert stationary and flying qubits[1]
- The ability to faithfully transmit flying qubits between specified locations

The operations required to implement the "universal" set of quantum gates change either the state of a single particle or act on a state common to at least two particles [4]. Several physical systems have been investigated for implementing a quantum computer such as superconductors [5], Rydberg atoms [6], quantum dots in silicon [7], neutral atoms [8, 9, 10] and trapped ions [11]. The ability to laser-cool and manipulate atomic systems, first achieved for atomic ions [12, 13] in 1978 and neutral atoms [14, 15, 16] in 1985, paved the way towards quantum experiments in such systems and the development of a potential quantum computer. One of the most important features for a given architecture is the ability to scale to large numbers.

Trapped ions are one of the experimentally most advanced scalable systems [17, 18, 19]. Here, the qubits are encoded in the energy levels of a single ion. The interactions between ions are mediated by the common motional state of the ions and are coupled to the internal state using sideband transitions. In the last decades, demonstration experiments with a few qubits have shown the basic techniques for the implementation of a quantum computer. As proposed by Cirac and Zoller in 1995 [11], these experiments were performed with ion strings in a single Paul trap. Although all necessary operations, such as quantum state preparation, manipulation, and detection have been demonstrated successfully, this approach is limited to a few tens of ions because of the complicated mode structure (the number of motional modes is $3N$ if N is the number of ions). One proposal to overcome this limitation is a QCCD (quantum charge-coupled device) architecture [20, 21], which consists of a large number of interconnected ion traps. This architecture allows for confining single ions at individual trap sites and shuttling between these traps by adjusting the trapping potentials. The information can hence be transported between single ion traps. With this proposal, a large-scale quantum information processor is feasible. Several groups are working on different aspects of this architecture, specifically on the development of a reliable transport of ions between different zones [22, 23, 24, 25]. The development of surface-electrode ion traps, in which the trap electrodes are in the same plane and the ion is trapped a few tens to a hundred microns above the surface, has a huge impact on scaling up the architecture [26, 27]. Microfabrication processes allow for a precise fabrication of complex electrode structures as necessary for shuttling junctions [28, 29].

Although a functional quantum computer is a rather distant goal, the advances in trapped-ion technology have already been used to simulate quantum many-body physics such as interacting spin models [30]. In general, two methods exist to realize the simulation of quantum many-body physics with trapped ions. One is based on

[1] Flying qubits can be for example freely propagating single-photon qubits.

sequences of multi-qubit operations, as necessary for a quantum computer. This approach is often called "digital" quantum simulations [31]. The other is studying quantum many-body systems by directly implementing the Hamiltonian of interest, an approach also known as "analog" quantum simulation or quantum emulation. For an overview, see [32, 33, 34]. In 2004, Porras and Cirac proposed two different approaches to study quantum magnetism using trapped-ion experiments [35]. One is based on the implementation in linear ion strings; the other is based on individual trapping sites in regular arrays, where ions in the individual sites interact through the Coulomb interaction. First attempts towards an engineered remote Coulomb interaction have been performed in a double-well system; two ions were trapped in individual wells of a double-well potential, and a remote coupling via the Coulomb interaction was observed [36, 37]. Recently, a subsequent experiment has shown that the Coulomb coupling can be transferred into a spin-dependent interaction using a laser-induced spin-motional coupling [38]. The ability to implement such arrays in surface-electrode ion traps which allow for complex electrode structures, as discussed for example in [39], has led to an increased interest in such array structures. First steps to implement a 3-site array in a planar geometry have been performed [40]. Furthermore, a scalable loading scheme for a 2D array has been investigated recently in [41].

Scaling up both, quantum information processing and quantum simulations, requires an extremely well-controlled system. In ion trap crystals, the two relevant degrees of freedom for the quantum control are the internal degrees of freedom (the internal energy levels) and the motional degrees of freedom, which can be described in terms of normal modes [42]. Laser beams can couple these different degrees of freedom and thus enable the required multi-ion spin-spin interactions mediated by the shared motional state, as exploited for both approaches. Lasers are commonly used since the applied optical field has large inhomogeneities across the motional wave packet of a single ion, which is typically on the order of ten nanometers. These inhomogeneities provide the spin-motional coupling. However, scaling up the system towards architectures with multiple ion trap arrays for either a quantum information processor or quantum simulator with laser control at each individual site introduces an additional scaling challenge. To handle the large laser overhead, Chiaverini and Lybarger [43] proposed to provide the spin-motional couplings by oscillating fields generated by radiofrequency (rf) or microwave conductors integrated in planar trap designs. The proposal is part of a general attempt to provide the spin-motional coupling directly with microwave radiation. Not only analogue quantum simulation designs benefit from such integrated conductors; they are also useful for quantum information processors. The lack of spontaneous emission and the reduced sensitivity to motional-state initialization could lead to high-fidelity gate operations, one of the most challenging steps for actually scaling up any architecture. So far, no experimental realization of a two-qubit operation has reached a fidelity above 99.99%, essential for fault-tolerant operation [44]. The ability to use microwaves

instead of laser radiation is motivated by the structure of the internal energy levels of the ions. Often, these levels are hyperfine levels separated by a microwave frequency. Here, the laser control is performed only indirectly through a stimulated-Raman process coupling to other short-lived electronically excited states [45]. In contrast to the laser radiation, free-space microwave fields exhibit a near-vanishing spatial inhomogeneity across the ion's wave packet. The ion essentially feels a constant field which cannot lead to any appreciable spin-motional coupling. However, by engineering the microwave fields, it is possible to achieve that coupling. One approach relies on static magnetic field gradients and homogeneous microwave fields [46], and the other induces the coupling through an amplitude gradient of an oscillating magnetic field provided by microwave conductors integrated into the trap structure [47]. In close proximity to the conductors, an appreciable coupling is possible. Note that the use of long-wavelength radiation to drive motional sideband transitions has a precursor in the g-2 experiments of Dehmelt and co-workers [48].

The miniaturization of ion traps paved the way towards the use of the near-field approach in planar ion traps. The close surface-to-ion distance in these traps allows for high gradients necessary for the spin-motional coupling. First demonstration experiments have shown that single-qubit gates below the fault-tolerant threshold [49, 50] and the generation of two-ion entanglement are feasible [51]. These experiments have demonstrated a tremendous reduction of laser overhead and experimental complexity. Subsequent experiments showed that individual addressing of single ions, one of the DiVincenzo criteria, is possible [52, 53]. The close distance to the surface needed for high gradients was one of the limiting points in the experiments performed with $^{25}Mg^{+}$ [51]. Here, the fidelities were at the level of 0.76(3). At a distance of only $30\,\mu$m, motional heating of the trapped ion [54] reduces the fidelity [55] of gates, especially entangling gates. To tackle this issue, two options are of interest: cooling the trap electrodes to cryogenic temperature [55, 56, 57, 36, 58] and cleaning the surface trap in situ [59, 60, 61]. The former also reduces background gas collisions by orders of magnitude and thus significantly improves the lifetime. Several groups are working on aspects that reduce motional heating and the understanding of the mechanisms behind the heating [62, 63, 64, 65] . In this work, we are interested in tackling a different limitation, the stability of the microwave fields performing the gate operations. In the near-field approach, an entangling gate is realized with a σ_φ-type gate [66, 67, 68]. This gate sequence is ideal for the near-field approach, since it is a so-called hot gate where no ground state cooling is required in principle. The scheme is based on sideband transitions, which implement the spin-motional coupling. These transitions change the internal state and the motional state simultaneously. A red sideband removes a quantum of motion, whereas a blue sideband adds one quantum of motion while changing the internal qubit state. To perform the gate, both interactions are applied simultaneously with a slight detuning from resonance.

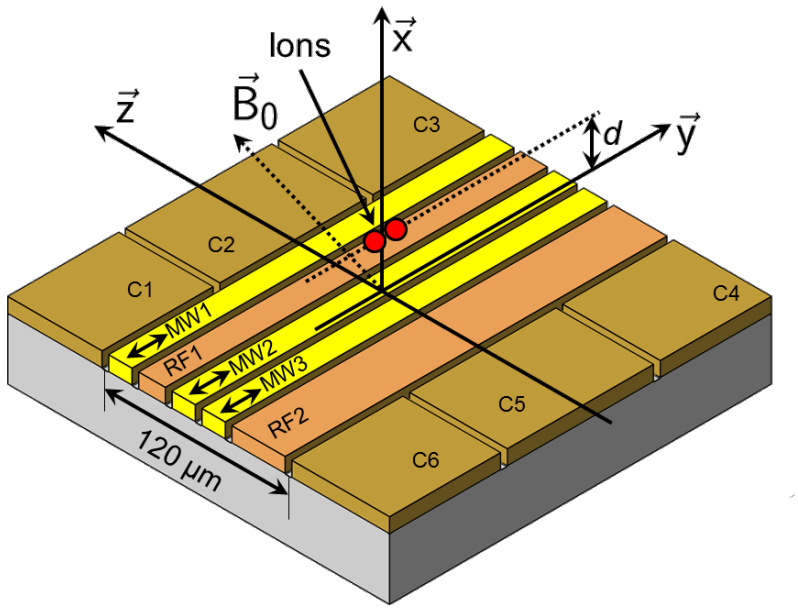

Figure 1.1: First demonstration ion trap design to implement the near-field approach. Here, three microwave conductors (MW1-3) provide the near-field configuration needed to induce a spin-motional coupling. The image was taken from [51].

To achieve high-fidelity entangling gates, it is essential to perform the spin-motional coupling with high accuracy. The spin-motional coupling, implemented with the near-field approach, requires a field configuration with a large oscillating magnetic amplitude gradient for driven motional sideband transitions, and an oscillating amplitude which is as small as possible. The oscillating field leads to off-resonant carrier transitions and to AC Zeeman shifts [47] which can spoil the spin-motional coupling. In the previous experiments [51, 69], the required field configuration was created by carefully balancing currents in three microwave conductors embedded in the planar trap design, as shown in Figure 1.1. By adjusting the phases and amplitudes of these currents, the magnetic near-field can be minimized at the position of the radiofrequency pseudopotential null, where the ion is located. While conceptually simple and tunable, this implementation has the drawback that keeping the current balanced, and thereby the field minimum stable, during a pulse sequence for multi-qubit operations can be challenging. This is especially difficult for high powers, as required for fast gates. The gate speed increases with the strength of the field gradient. Although embedding the conductors in resonant circuits significantly reduces the applied power and could hence potentially lead to higher stability [69], it could also cause undesired coupling between the three different resonant circuits that result in frequency shifts.

From a practical point of view, it would be desirable to implement the spin-motional coupling with a single microwave electrode which provides the magnetic field configuration "by design". This simplifies the implementation of the required quantum control even further; however, it complicates the design of the surface-electrode ion trap. The challenge of this approach is to overlap the magnetic near-field minimum with the pseudopotential null by design. For this purpose, a toolchain for highly accurate simulations of the microwave currents in the electrode structure of surface-electrode ion traps is developed in this thesis. The simulations are performed in a state-of-the-art full-wave numerical simulation tool, Ansys HFSS. The trap design developed here features a single microwave conductor for inducing sideband transitions, which is laid out in the shape of a meander line. I investigate whether this shape is appropriate for creating the corresponding field configuration and design a first test chip. The microwave quantum control is engineered for a field-insensitive transition in the hyperfine manifold of a Beryllium ion. Although the toolchain is developed for Beryllium ions, it can be used for other ions. We use a single ion as a high resolution quantum sensor to measure the magnetic field distribution provided by the meander-shaped electrode through energy shifts induced in the hyperfine energy levels. To describe the field distribution required for the spin-motional coupling, we develop a two-dimensional near-field model, which can be used to compare measured and simulated near-fields. This allows us to calibrate the toolchain.

The development of a quantum control approach based on a single-electrode design would benefit both the scalability to large-scale trap arrays as well as the fidelities of the spin-motional coupling. The single-electrode design offers excellent stability of the near-field minimum at the ions' position, which can lead to the high-fidelity gate operations necessary for quantum information processing. Furthermore, the single-electrode microwave design is an important simplification of the previous microwave approaches to implement ion trap arrays, as required for quantum simulators.

Thesis outline

The structure of this thesis is as follows. **Chapter** 2 gives a brief overview of the basics relevant for the design of surface-electrode ion traps. This includes the general principle of linear Paul traps and the pseudopotential approximation. Furthermore, the idea of an adjustable rf potential is discussed. In **Chapter** 3, I present the basics of the oscillating near-field approach in Beryllium ions, including the level structure, the field-independent qubit as well as the interaction of the ion with oscillating magnetic fields. Here, I further present the two-dimensional near-field model used to describe the desired field configurations for spin-motional couplings. **Chapter** 4 covers different designs implementing the single-electrode near-field approach. Here, the general idea of the single-electrode design, including

the integration of such an electrode into a surface-electrode ion trap is discussed. I present the optimization of the combined structure and the corresponding simulation models. In **Chapter** 5, the apparatus used to perform trapped-ion experiments with the microwave near-field approach is described. This includes the vacuum chamber, laser systems, electronics, as well as the ion trap and its fabrication. In **Chapter** 6, I present the measurement of the microwave near-field provided by the single-electrode design using a single beryllium ion as a quantum sensor. This includes the characterization of the trapping potential as well as micromotion compensation. **Chapter** 7 gives an outlook into advanced designs for multi-qubit operations such as multi-layer traps based on the results obtained in this work. Finally, I summarize the results in **Chapter** 8.

Chapter 2

Surface-electrode ion trap design

Surface-electrode ion traps are a promising platform to implement large-scale quantum information processors (QIP) and quantum simulation, as discussed in the introduction. The ability to use standard well-known microfabrication processes enables complex structuring of the electrode design. Most surface-electrode ion traps used for quantum simulation and information are based on the fundamental ion trap developed by Wolfgang Paul [70]. Only a few approaches implement QIP with planar Penning traps such as [71, 72, 73, 74]. Compared to the commonly used laser-based approach, a microwave-based control can be integrated directly into the trap structure in a rather straightforward way by embedding microwave conductors. The idea to provide the control for spin-motional coupling using a single electrodes requires a thoughtful choice of the trap design. A linear Paul trap is the most suitable design because microwave conductors can be placed in parallel to the trap electrodes. Before considering the design of a surface-electrode ion trap, basic properties of linear Paul traps are discussed. Since a single-electrode design provides a fixed field configuration, the possibility to create an adjustable radiofrequency (rf) potential is investigated. Such a potential provides the flexibility to overlap the ion position with the microwave magnetic field minimum.

2.1 Linear Paul traps

To trap a charged particle, confinement in all three dimensions is required. Electrostatic fields would be the obvious intuitive choice, since these fields are easy to generate and control. However, confinement in all three dimensions with purely electrostatic fields is not allowed by the laws of physics (Earnshaws theorem [75]), since $\nabla \cdot \vec{E} = 0$. A three-dimensional confinement can either be achieved with

a combination of magnetic and electric fields or a combination of oscillating and static electric fields. The former is used in Penning traps, while the latter is used for Paul traps, which are discussed here. The information given in this section is based on the detailed descriptions in [20, 76].

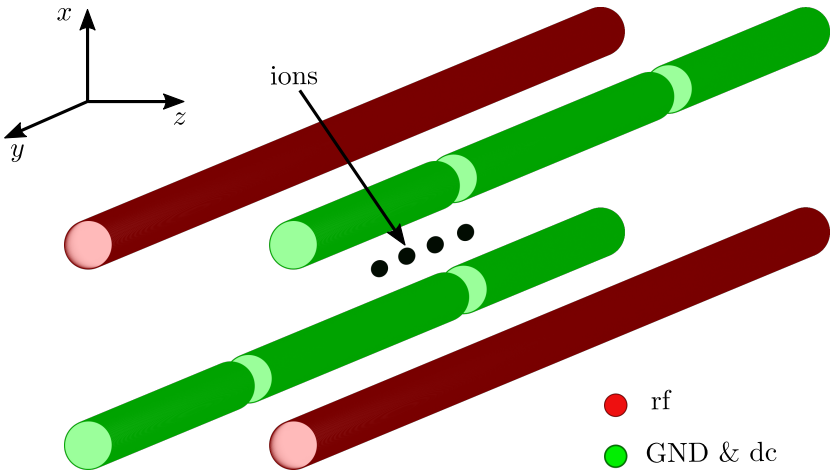

Figure 2.1: Configuration of a linear Paul trap. Applying an oscillating field on the rf electrodes (red) yields a confinement in the radial direction (xz-plane). The axial confinement (y-axis) is provided by a static potential on the control electrodes (GND & dc). For strong radial confinement, the ions line up on the center axis of the electrode configuration.

The potential in a Paul trap is a combination of static and dynamic potentials; in the simplest form, the latter is a potential with a quadrupole shape in the trapping center. Such a field can be created by four electrodes arranged in a square. Applying an oscillating voltage on two diagonally opposing electrodes, while the others are held at ground, a quadrupole potential oscillating with the drive frequency is produced in the plane perpendicular to the rods, the radial plane. This configuration is known as a linear Paul trap and is illustrated in Figure 2.1 together with control electrodes used to apply a static potential for the additional axial confinement. The control electrodes are created by segmenting the ground electrodes and putting a negative potential on the center part. The grounded segments next to the central control electrodes are known as the "endcap electrodes". In a quadrupole potential, at any specific moment in time, the ion feels an inward force in one radial direction and outward force in the other radial direction. After a half cycle of the oscillation, the situation is reversed. To achieve a stable trapping potential, the frequency and voltage applied to the electrodes must be chosen appropriately. The dynamics of an ion in the trap provide information about the stability of the ion trap in the sense that the ion needs to follow a stable orbit in the oscillatory field. From these dynamics, stability regions can be identified. These regions depend on the applied voltages and thus, require a suitable design of

the trap drive. One approach to calculate the dynamics uses the Mathieu equation. In the case of the ideal linear Paul trap, the axial motion is described by a simple harmonic motion. We are, however, mostly interested in the radial motion because we will be using radial modes for near-field induced quantum logic operations. In order to provide these operations with a single electrode, the null position of the radial confinement is of particular interest since it is used to design the combined trap geometry with an overlap of the electric and magnetic field quadrupoles (cf. chapter 4). The following considers only the radial confinement.

Applying a static and an oscillatory potential, U and $V\cos(\Omega_{\mathrm{rf}}t)$) respectively, on two opposing electrodes of the linear Paul trap while the others are held at ground yields the following potential in the radial plane

$$\Phi(x,z,t) = (U - V\cos(\Omega_{\mathrm{rf}}t)) \quad \frac{x^2 - z^2}{2r_0^2}, \tag{2.1}$$

where r_0 is the distance from the center to an electrode and Ω_{rf} the drive frequency. In this potential, the motion of a trapped ion with mass m and charge q in the xz-plane, the radial plane, is described by the differential equations

$$\frac{d^2x}{dt^2} + \frac{q}{mr_0^2}(U - V\cos(\Omega_{\mathrm{rf}}t))x = 0 \tag{2.2}$$

$$\frac{d^2z}{dt^2} - \frac{q}{mr_0^2}(U - V\cos(\Omega_{\mathrm{rf}}t))z = 0. \tag{2.3}$$

With the transformation

$$a_x = -a_z = \frac{4qU}{mr_0^2\Omega_{\mathrm{rf}}^2}, \quad q_x = -q_z = \frac{2qV}{mr_0^2\Omega_{\mathrm{rf}}^2} \quad \text{and} \quad \zeta = \frac{\Omega_{\mathrm{rf}}t}{2},$$

the differential equations can be expressed as Mathieu equations

$$\frac{d^2x}{d\zeta^2} + (a_x - 2q_x\cos(2\zeta))x = 0 \tag{2.4}$$

$$\frac{d^2z}{d\zeta^2} + (a_z - 2q_z\cos(2\zeta))z = 0. \tag{2.5}$$

We obtain solutions for these equations by using the Floquet theorem [77]. Only for specific combinations of a_i and q_i parameters, a stable trapping potential is reached. We assume that $a_i < q_i^2 \ll 1, i \in x, y$, a typical case for linear Paul traps. The first order solution is

$$u_i(t) \approx u_{0i}\cos(\omega_i t + \psi_i)\big(1 + \frac{q_i}{2}\cos(\Omega_{\mathrm{rf}}t)\big). \tag{2.6}$$

with

$$\omega_i \cong \frac{\Omega_{\mathrm{rf}}}{2}\sqrt{a_i + \frac{q_i^2}{2}}, \tag{2.7}$$

where ψ_i and u_{0i} depend on the initial position and the velocity of the ion. The solution consists of two different kinds of motion: a harmonic oscillation at the so-called secular frequency $\omega_{x,z}$ and a rapid oscillation at the drive frequency Ω_{rf}, known as micromotion, which is minimized at the center of the trapping potential. Applying additional electrostatic fields on the control and endcap electrodes provides the confining potential for the ion in the axial direction, which is here the y-direction. These fields and any other stray fields can move the ion out of the center of the radial confinement, leading to excess micromotion. The micromotion due to a displacement induced by the secular motion is called intrinsic micromotion. While the latter is unavoidable, the former can be compensated by using electrostatic fields to bring the ion back to the rf minimum. Excess micromotion can also occur due to a phase shift between the voltages on the rf electrodes. That motion cannot be compensated by applying static compensation fields.

The pseudopotential approximation [78, 79] describes the treatment of the potential as that of a harmonic oscillator. Here, the force experienced by an ion in the oscillatory field is time averaged, leading to the pseudopotential ϕ_{pp}:

$$q\phi_{\mathrm{pp}} = \frac{1}{2}m\omega_r^2(x^2 + z^2) \tag{2.8}$$

with

$$\omega_r = \frac{qV}{\sqrt{2}mr_0\Omega_{\mathrm{rf}}} = \frac{q_x\Omega_{\mathrm{rf}}}{2\sqrt{2}}. \tag{2.9}$$

Here, ω_r is the radial secular frequency, assuming an electrode configuration which is cylindrically symmetric. From Equation (2.8) and (2.9), we can estimate the influence of each parameter on the trapping potential, such as the ion-to-electrode distance r_0, the drive frequency Ω_{rf} and amplitude V. Although the equations are derived for three-dimensional linear Paul traps, the basic idea can be transferred to surface-electrode ion traps. In surface-electrode Paul traps, however, the additional control electrodes provide an electrostatic field in the radial direction in addition to the axial confinement. Although this field can be cancelled at the pseudopotential null, it is typically not oriented along the same spatial direction as the radiofrequency quadrupole associated with the voltage $V\cos(\Omega_{\mathrm{rf}}t)$, so that in general, the two radial equations of motion do not decouple. In terms of the stability of the traps, assuming a decoupled motion seems to lead to an overly conservative estimate of stability [80]. This does not, however, affect the calculation of secular frequencies within the pseudopotential approximation. Since the potential is not fully symmetric, the generalized form [78] of Equation (2.8) is more appropriate:

$$\phi_{pp} = \frac{q^2}{4m\Omega_{\mathrm{rf}}}|\Delta\phi_{\mathrm{rf}}|^2, \tag{2.10}$$

where ϕ_{rf} describes the time-averaged dynamic potential around the trapping center. The three-dimensional linear Paul trap design already provides significant insight

into the design of a surface-electrode ion trap, since the design can be transferred into a two-dimensional plane using a Möbius transformation [81].

2.2 Analytic tools for trap design

In the pseudopotential approximation, the electric field originating from the radiofrequency electrodes, usually oscillating at a frequency between 100 kHz and 100 MHz, is treated in terms of electrostatics. This simplifies the calculation of the quadrupole field and moreover, the design of the electrode geometry. Surface-electrode ion traps are usually single-layer metal electrodes grown on a dielectric substrate. To avoid any stray fields occurring from accumulated charges on the dielectric surfaces, the gap sizes between electrodes are kept as small as possible. Figure 2.2 shows an example of a typical surface-electrode ion trap geometry. This geometry can be obtained by transferring the three-dimensional (3D) geometry in Figure 2.1 into a two-dimensional (2D) plane using a Möbius transformation. A detailed description of mapping a 3D linear Paul traps into a planar Paul trap can be found in [81].

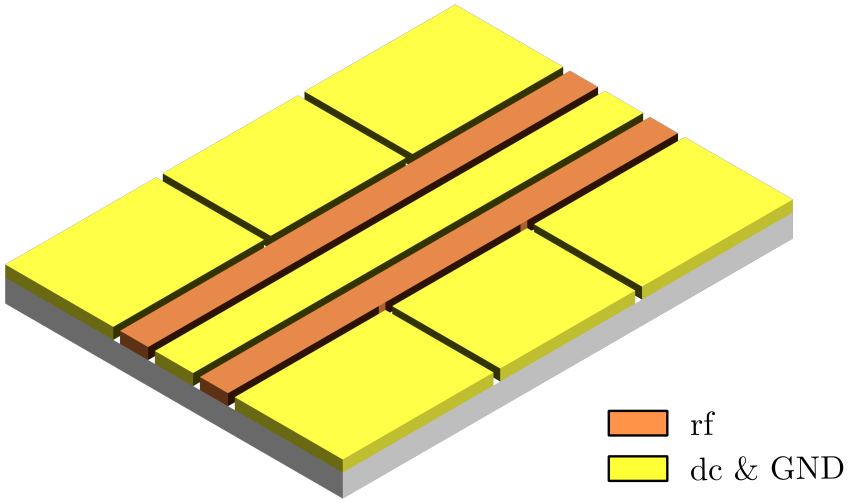

Figure 2.2: Typical surface-electrode ion trap. The electrodes are arranged as a linear Paul Trap with control electrodes on each side (dc). The radial confinement is determined by the rf electrode geometry. Usually the ion is trapped only a few tens of microns above the surface.

Several numerical simulation methods are available to solve the field configuration for such trap geometries. Boundary element methods [82] and finite-element methods [83] have found wide-spread success in the community, and because of their high accuracy should in general be considered for the final design. However,

such numerical simulations are time-consuming and hence not suitable for finding a rudimentary design on which to base further developments. For the specific case of surface-electrode ion traps, the rf pseudopotential can be simply calculated using the Biot-Savart-like law for electrostatics [84]. This method uses the gapless plane approximation, in which the electrode geometry is laid out in a single plane extended to infinity with vanishing gap sizes between the electrodes. Here, any given electrode is kept at a potential V, whereas the surrounding electrodes are at zero potential, and more complicated voltage combinations can be treated by the superposition principle. To use this approximation, the gap size in an actual ion trap must be significantly smaller than the ion-to-surface distance, and the extension of each electrode must be much larger than the gap size. Surface-electrode ion traps are usually designed to fulfill these requirements. In the following, I will briefly describe the basics of the Biot-Savart-like law.

2.2.1 Biot-Savart-like law

The Biot-Savart-like law for electrostatics is a powerful tool to calculate the electrostatic field of an arbitrarily shaped two-dimensional electrode. The general idea is to integrate over infinitesimal parts of the contour of any given electrode and to determine the related electric field using the analog to the actual Biot-Savart law [85].

The approach assumes a flat electrode lying in a plane and kept at a constant potential V while the surrounding area is set to zero potential. The geometry of the electrode is given by the closed boundary curve C. The electric field at a point P is determined by the potential on the electrode. As derived in [84], the potential for such a configuration is given by

$$\phi(\vec{r}) = \frac{V}{2\pi}\Omega(\vec{r}), \tag{2.11}$$

where $\Omega(\vec{r})$ is the solid angle spanned by the electrode area as seen from $\vec{r}$. Figure 2.3 illustrates the geometric parameters for calculating Ω. In the yz-plane, the solid angle is

$$\Omega(\vec{r}) = \int \frac{(\vec{r} - \vec{r}^{\,'}) \cdot \vec{e}_x}{|\vec{r} - \vec{r}^{\,'}|^3} dy' dz', \tag{2.12}$$

assuming $x > 0$. $\vec{r}^{\,'}$ defines a specific point in the electrode plane. We obtain the electric field $E(\vec{r})$ by inserting the solid angle expression (Eq. (2.12)) into the potential $\phi(\vec{r})$ and using Stokes' theorem [85]:

$$E(\vec{r}) = -\Delta\phi(\vec{r}) = \frac{V}{2\pi} \oint_C \frac{(\vec{r} - \vec{r}^{\,'}) \times \vec{dr}^{\,'}}{|\vec{r} - \vec{r}^{\,'}|^3}. \tag{2.13}$$

The integration is performed clockwise along the boundary curve C, as indicated in Figure 2.3. The prerequisites for the calculation are the same as for the gapless

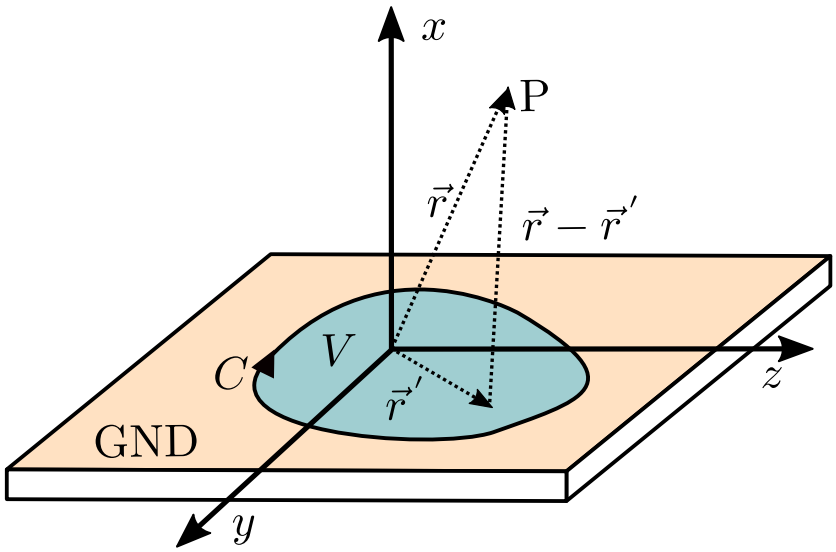

Figure 2.3: Configuration to calculate the electric field at a point P with the Biot-Savart-like law from an electrode with a potential V surrounded by a zero potential region (GND). The electrode geometry is determined by the closed boundary curve C [84].

plane approximation. Hence, with Equation (2.13), we obtain the electric field for any electrode geometry as long as the gapless plane approximation is valid. This approach is used to calculate the field configuration for a specific trap geometry. Based on this calculation, the pseudopotential null position as well as trap depth and frequency can be obtained. Furthermore, it is possible to include the electrostatic field for the axial confinement in the calculation, obtaining the complete set of trap parameters. The complete potential is then given by

$$\phi_{trap} = \phi_{\mathrm{rf}} + \phi_{\mathrm{dc}}. \tag{2.14}$$

For a given geometry, it is possible to determine the voltages needed to achieve the axial confinement with specific boundary conditions. The number of dc electrodes determines the number of degrees of freedom. This number is reduced by specifying requirements for the axial confinement. In general, the axial confinement is overlapped with the radial confinement, and hence all components of the dc field are minimized at the rf pseudopotential null position. For six dc electrodes as in Fig. 2.2, this overlap can be achieved by imposing equal voltages on pairs of endcap voltages and by imposing a null dc field in the x- and z-directions at the rf pseudopotential null position. The field is zero by symmetry in the axial direction. The two remaining parameters can be specified setting the trap frequency in the axial direction and the rotation of the normal modes with respect to the surface to a fixed value. Ideally, the dc voltages are set in such a way that the ion position is overlapped with the rf pseudopotential null to avoid excess micromotion. Besides these "optimal" field solutions, we are also interested in so-called

"shim fields". These are linear combinations of voltages, applied to all electrodes together and superimposed with the trapping voltages, which let us apply a field of given magnitude in any spatial direction, possibly while minimizing the associated potential curvature. These "shim fields" are used for example to compensate any stray fields present in the trap due to laser-induced charging of dielectric materials. For specific applications in our project, it was desirable to obtain geometries with individually controllable rf electrodes. The same methodology applied above can also be used to calculate the pseudopotential in this more general case.

2.2.2 Adjustable rf potential

Integrating the microwave control into a surface-electrode ion trap using a single-electrode design has a substantial drawback. The near-field minimum is given by design and cannot be adjusted to achieve perfect overlap with the pseudopotential null (cf. chapter 4). One approach to overcome this issue is to adjust the rf potential instead of the microwave near-field minimum. To adjust the rf potential in all directions of the radial plane, at least three electrodes with independently adjustable potentials are required. We model these electrodes as planar conductors infinitely extended along the axial direction. These electrodes are located in the yz-plane and are surrounded by ground electrodes, also extended to infinity. The control electrodes for the axial confinement are neglected. This assumption is appropriate, since the position of the pseudopotential null is solely defined by the radiofrequency field. We determine the potential of the rf electrode using the Biot-Savart-like law and the pseudopotential approximation. We assume that the phases of the voltages applied to all rf electrodes are identical. In the case of planar electrodes which are infinitely extended along the axial direction (y-direction), the potential in the radial plane, the xz-plane, can be solved analytically using Equation (2.11) and (2.12). The potential $\phi_i(x, z)$ provided by an electrode i with an applied voltage V_i which is extended from $z = z_i^s$ to $z = z_i^e$ is then given by:

$$\phi_i(x,z) = \frac{V_i}{\pi}\left(\arctan\left(\frac{x-z_i^s}{z}\right) - \arctan\left(\frac{x-z_i^e}{z}\right)\right). \tag{2.15}$$

Although the voltage V_i of each electrode is individually adjustable, two of those electrodes together should form a trapping potential with a minimum close to the microwave near-field minimum when identical voltages are applied to both electrodes. This will make it possible to also operate the trap from a single rf source for inital loading and debugging. The aim here is to investigate how far the pseudopotential minimum can be moved by applying a small voltage to a third electrode or by modifying the voltage ratio of the two first electrodes.

To give a specific example, let us consider a symmetric electrode configuration with four rf electrodes surrounding three microwave segments. Figure 2.4 a) shows the arrangement of the electrodes with the resulting rf field configuration and b)

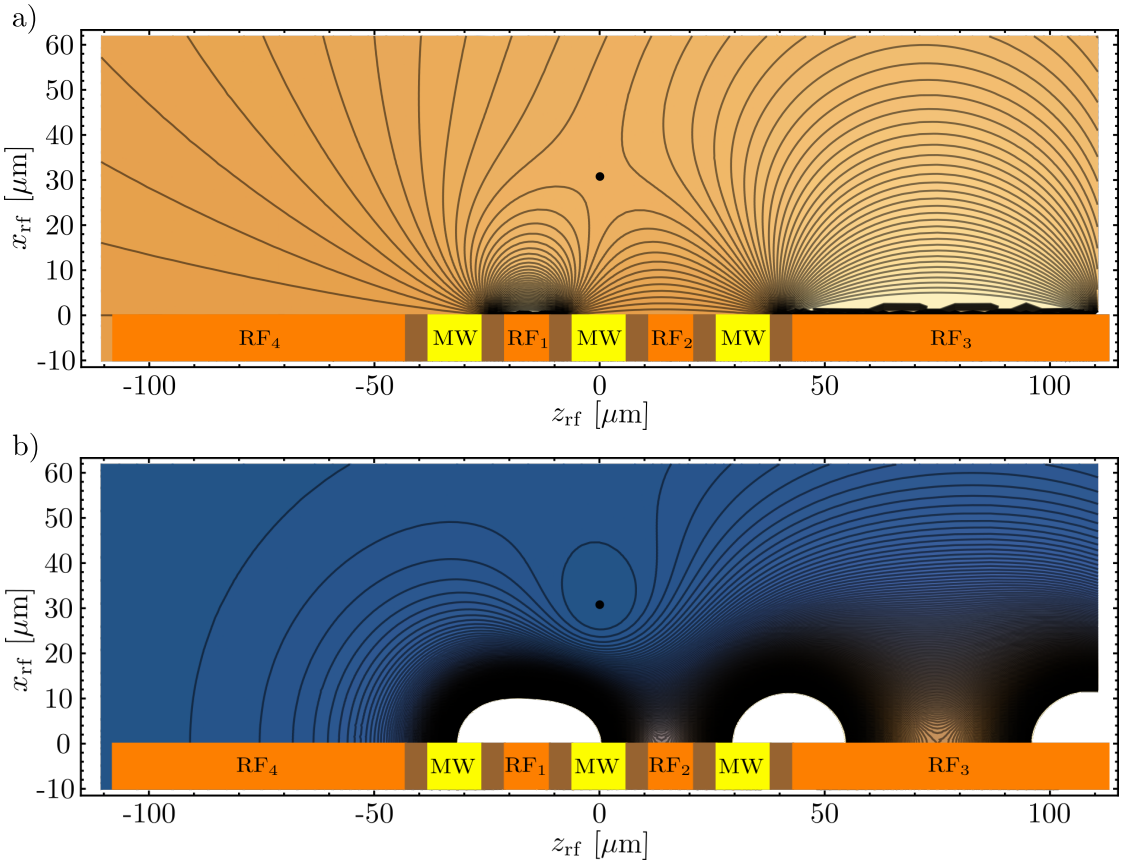

Figure 2.4: Electrode configuration for a symmetric microwave arrangement (MW). The voltage V_i of the four rf electrodes RF_i, $i = 1, .., 4$ is independently adjustable. The rf field configuration for $V_1 = V_3 = 1$ and $V_2 = V_4 = 0$ is shown in a) while b) is the resulting pseudopotential.

the pseudopotential. Here, we consider only the field produced by the electrodes RF_1 and RF_3 with $V_1 = V_3 = 1\,\mathrm{V}$, while the MW electrodes are set to rf ground. Fixing the widths $w_{\mathrm{RF}_1} = 10\,\mu\mathrm{m}$, $w_{\mathrm{RF}_3} = 65\,\mu\mathrm{m}$ and $w_{\mathrm{MW}} = 12\,\mu\mathrm{m}$ with a gap size of $5\,\mu\mathrm{m}$, the pseudopotential position null is at $(z_{\mathrm{rf}}, x_{\mathrm{rf}}) = (0.15\,\mu\mathrm{m}, 30.9\,\mu\mathrm{m})$. These are our initial values for the adjustment of the rf voltages. Note that we use the gapless plane approximation here; half the gap size is added to each electrode where the gap is located in reality. This assumption leads only to minor errors, if the gap sizes are small compared to the electrode size [86]. Fine-tuning the position of the rf pseudopotential is now possible by changing the ratio of V_1 and V_3 or by applying an additional voltage V_2 or V_4. Figure 2.5 shows the position of the rf pseudopotential null as a function of the amplitude V_2. The voltage is given in multiples of the voltage applied to electrode RF_1, which is set to $V_1 = 1\,\mathrm{V}$. To compensate a mismatch of the rf pseudopotential and the near-field minimum of about $2\,\mu\mathrm{m}$ in the x-direction, at least 25% of the amplitude of V_1 has to be

applied to electrode RF_2. Similar results are obtained by altering voltages V_3 and V_4 relative to V_1. To achieve an overlap in both directions, two voltages are changed simultaneously. For a given position of the microwave near-field minimum $(x_{\mathrm{MW}}, z_{\mathrm{MW}})$, the voltage combination for an overlap is obtained by solving

$$\frac{\partial \phi_{\mathrm{rf}}(x_{\mathrm{MW}}, z_{\mathrm{MW}})}{\partial x} = 0 \quad \text{and} \quad \frac{\partial \phi_{rf}(x_{\mathrm{MW}}, z_{\mathrm{MW}})}{\partial z} = 0.$$

To achieve a perfect overlap of both minima in the experiment, the rf sources should therefore allow for an independent adjustment of each voltage. Since the calculated voltage values can differ from the initial experimental settings, we need to adjust the voltages while an ion is trapped in the potential. The voltage combination necessary to obtain the overlap should be reached by gradually changing the initial values. This allows for maintaining a stable trapping potential during the adjustment.

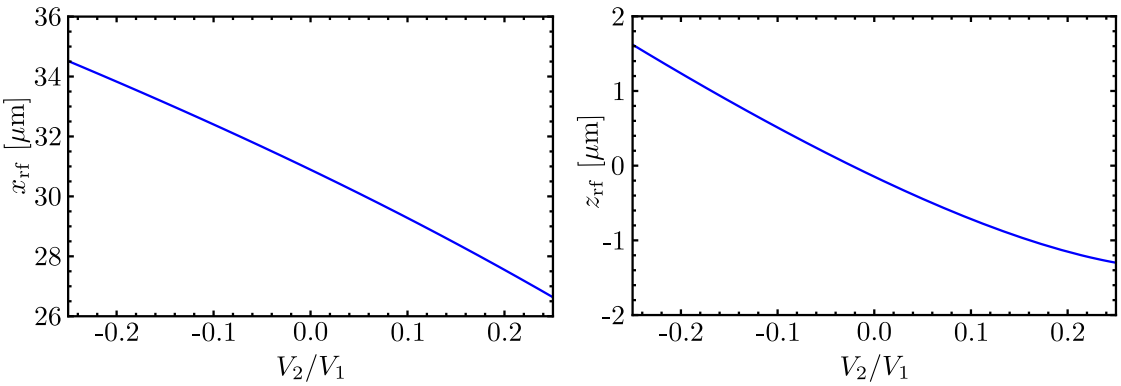

Figure 2.5: Position $(x_{\mathrm{rf}}, z_{\mathrm{rf}})$ of the rf pseudopotential null as a function of the applied voltage V_2 in multiples of V_1. The other voltages are set to $V_1 = V_3 = 1\,\mathrm{V}$ and $V_4 = 0\,\mathrm{V}$.

Chapter 3

Microwave quantum logic with $^9Be^+$

The oscillating magnetic field approach to address and control qubit states of trapped ions requires qubit splittings in the radiofrequency or microwave regime. In trapped ions, such transitions appear between hyperfine or Zeeman levels. Choosing qubit states in the hyperfine manifold of the electronic ground state of an ion has the advantage that transitions exists which are magnetic-field-insensitive to first order and can yield long coherence times ($> 10\,s$) [87]. Any ion with a nuclear magnetic moment $I > 1/2$ and an electron angular momentum $J > 0$ exhibits such transitions. Our experiments are performed in the electronic ground state hyperfine manifold of ionized beryllium where several field-insensitive transitions for different magnetic field strengths exist. Using beryllium ions has the advantage that, due to their low mass, high trap frequencies are feasible for a given electric field. Furthermore, when trap voltages are small, such as in surface-electrode ion traps, it is highly beneficial if the work functions of the neutral atoms from which the ions are created and of the trap surfaces, typically made out of a different metal, are similar. Due to similar work functions, the effect of patch potentials occurring from neutral atoms deposited during the loading process is reduced. A typical metal used in surface-electrode ion traps is gold, whose work function value is 5.1 eV, which is close to that of beryllium (5.0 eV). In this chapter, I present the basics for implementing the oscillating near-field approach in $^9Be^+$, including the level structure, our hyperfine qubit and the interaction with an oscillating magnetic field. Detailed information on the topics discussed in the first section can be found in [88]. The basics of the oscillating magnetic field approach are discussed in [47]. Our model describing the two-dimensional near-field needed to induce a spin-motional state coupling completes the discussion. The model is documented in [89], which is under review at the time of this writing.

3.1 $^9Be^+$ Qubit

With two valence electrons, neutral beryllium belongs to the group of alkaline earth metals. When ionized, such elements have a similar level structure to alkali atoms, implying a simple atomic structure due to the single valence electron. This simple structure is favorable for trapped-ions experiments. The required optical transitions are addressable with available laser wavelengths. Beryllium is the lightest element in that group, allowing for the highest trap frequencies (Eq. (2.9)) for a given electric field. In the oscillating magnetic field approach, high trap frequencies are desirable to avoid off-resonant excitation while driving motional sideband transitions.

3.1.1 Level structure

The relevant atomic structure of ionized beryllium used in trapped-ion experiments is illustrated in Figure 3.1. Such experiments require a pair of energy levels defining the qubit states as well as optical transitions for state preparation and detection. The former are often chosen to be sublevels of the ground state (S-orbital), while the latter are electric dipole transitions between the ground state and higher orbitals. In $^9Be^+$, this transition is between the S-orbital and the P-orbital, the lowest excited state, with a wavelength of 313 nm.

The level structure is determined by the different couplings of angular momentum. We have to distinguish between fine and hyperfine structure. The fine structure is a result of the coupling between the orbital angular momentum $\mathbf{L}$ of the outer electron and the spin angular momentum $\mathbf{S}$. The resulting electron angular momentum $\mathbf{J}$ is given by $\mathbf{J} = \mathbf{L} + \mathbf{S}$ with the corresponding quantum number J, $J \in \{|L - S|, \ldots, L + S\}$. With this relation, we obtain the fine structure for $^9Be^+$. The ground state has a single energy level with $J = 1/2$, since $L = 0$ and $S = 1/2$, while the lowest excited state is split into two states, $J = 1/2$ and $J = 3/2$. The spectroscopic notation for these energy levels is $^{2S+1}L_J$, where L is given by the subshell letter $L = 0, 1, 2, .. \equiv \mathrm{S}, \mathrm{P}, \mathrm{D}, ...$ Hence, the ground state level is $^2\mathrm{S}_{1/2}$, and the two levels of the excited states are $^2\mathrm{P}_{1/2}$ and $^2\mathrm{P}_{3/2}$. The fine structure splitting of the P-orbital is 197.2 GHz.

The fine structure levels are split further into hyperfine sublevels by the coupling of the electron angular momentum and the nuclear angular momentum $\mathbf{I}$. The resulting atomic angular momentum is $\mathbf{F} = \mathbf{J} + \mathbf{I}$ with the corresponding quantum number F, $F \in \{|J - I|, \ldots, J + I\}$. $^9Be^+$ has a nuclear spin of $I = 3/2$. Hence, the ground state $^2\mathrm{S}_{1/2}$ is split into two levels $F = 1$ and $F = 2$ with an energy splitting of 1.25 GHz. The hyperfine structure of the $\mathrm{P}_{1/2}$ level has a splitting of 237 MHz while that of the $\mathrm{P}_{3/2}$ is below 1 MHz [90, 91]. As shown in Figure 3.1, the hyperfine structure is also divided into sublevels. Each hyperfine level has $2F + 1$ magnetic sublevels. At zero magnetic field these sublevels are degenerate. Applying a static magnetic field breaks this degeneracy. The energies of these levels

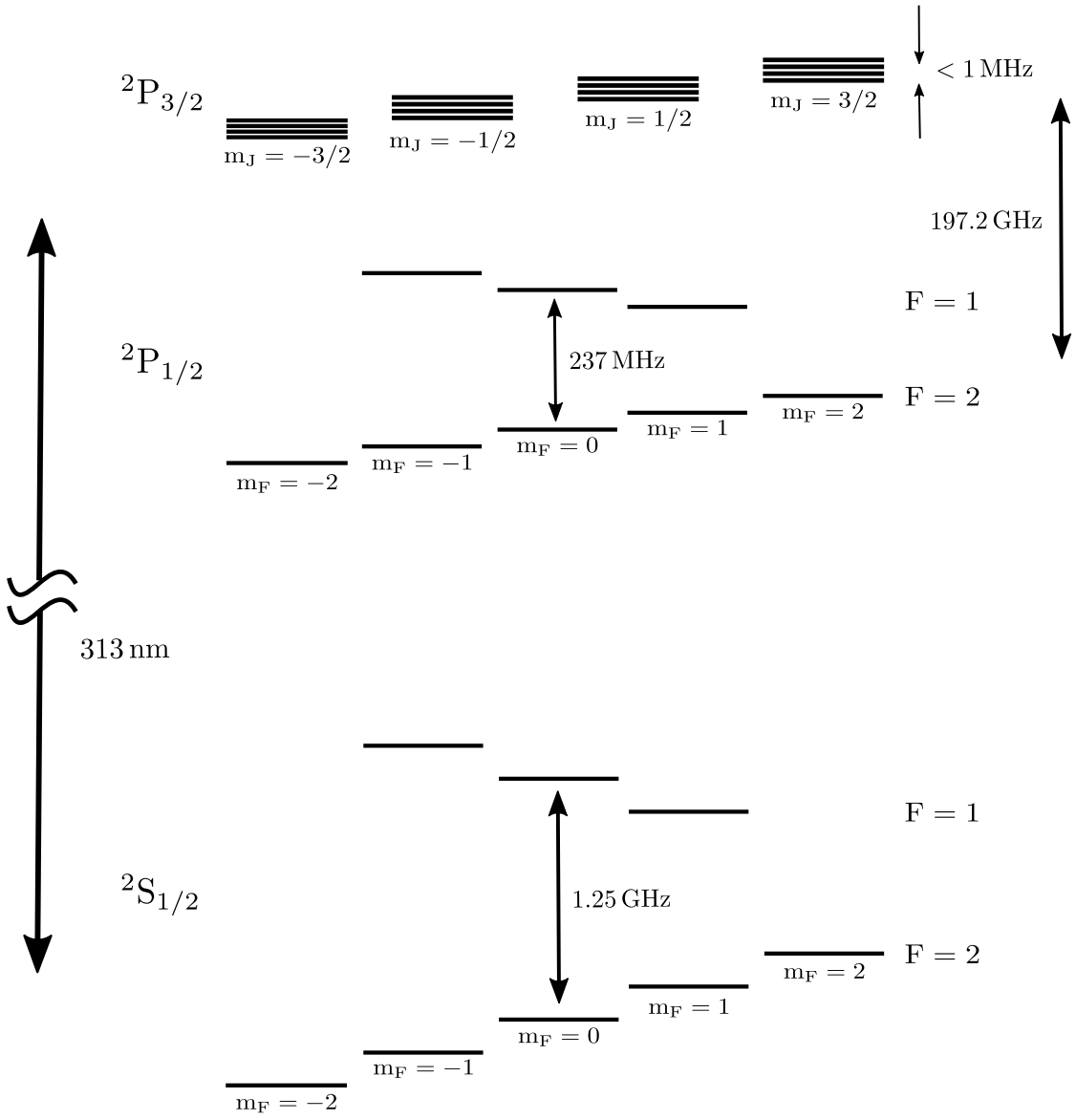

Figure 3.1: Energy level diagram for $^9Be^+$. The electric dipole transition between the S- and P-orbital is at 313 nm. The fine structure levels $^2P_{1/2}$ and $^2P_{3/2}$ of the P-orbital are split by 197.2 GHz, while their hyperfine splittings are at 237 MHz and below 1 MHz, respectively. In the ground level $^2S_{1/2}$ the hyperfine levels are split by 1.25 GHz. Each of the hyperfine F states is divided into $2F + 1$ magnetic sublevels m_F if an external magnetic field is applied.

change depending on the external magnetic field. At low fields, the sublevels of the hyperfine manifold are described in the $|F, m_F\rangle$ basis. Pairs of these sublevels are usually used as the qubit states. Typical transition frequencies are in the microwave domain, allowing the use of the oscillating magnetic field approach to implement trapped-ion quantum logic.

3.1.2 Hyperfine qubit

In the hyperfine manifold of $^2\mathrm{S}_{1/2}$, magnetic-field-insensitive transitions exist. These transitions are first-order-insensitive to magnetic-field fluctuations, which can be exploited for long-lived qubits. In $^9\mathrm{Be}^+$, four of these transitions exist for different magnetic field strengths. In the experiment, we apply an external magnetic field $\mathbf{B}$ to define the quantization axis and to resolve the hyperfine sublevels due to the linear Zeeman effect. The choice of the qubit transition determines the magnetic field strength, as shown in the following.

The Hamiltonian of the combined interaction of the hyperfine structure and the external field is given by

$$\mathbf{H} = hA\,\mathbf{I}\cdot\mathbf{J} - \boldsymbol{\mu}\cdot\mathbf{B} \tag{3.1}$$

where h is Planck's constant, A a hyperfine constant and $\boldsymbol{\mu}$ the magnetic dipole operator. The interaction with the external magnetic field $\mathbf{H}_B = -\boldsymbol{\mu}\cdot\mathbf{B}$ is different for weak and strong magnetic fields. For strong magnetic fields, the interaction is described by the Paschen-Back effect. Here, the interaction with the external magnetic field dominates over the hyperfine energy and J, I, m_J and m_I are good quantum numbers. The energy shift W_B for a magnetic field in the z-direction is then given by

$$W_B = (\mu_B g_J m_J + \mu_K g_I m_I)\, B_z, \tag{3.2}$$

where g_I, g_J are the Landé g-factors for the electron angular momentum J and nuclear spin I, μ_B the Bohr magneton and μ_K the nuclear magneton. In the weak-field regime, the coupling of the nuclear spin to the electronic angular momentum is stronger than the energy associated with the external magnetic field. In that regime I, J, F and m_F are good quantum numbers and the interaction energy W_B becomes

$$W_B = \mu_B g_F m_F B_z, \tag{3.3}$$

with g_F as the Landé g-factor for the atomic angular momentum. The regime of weak fields is known as the Zeeman regime.

In the intermediate regime, the energy of the sublevels can neither be described in the $|F, m_F\rangle$ nor in the $|m_J, m_I\rangle$ basis. To determine the energy, we need to diagonalize the combined Hamiltonian. For the ground state $^2\mathrm{S}_{1/2}$ and all other states with $F = I \pm 1/2$, the energy of the hyperfine sublevels can be determined

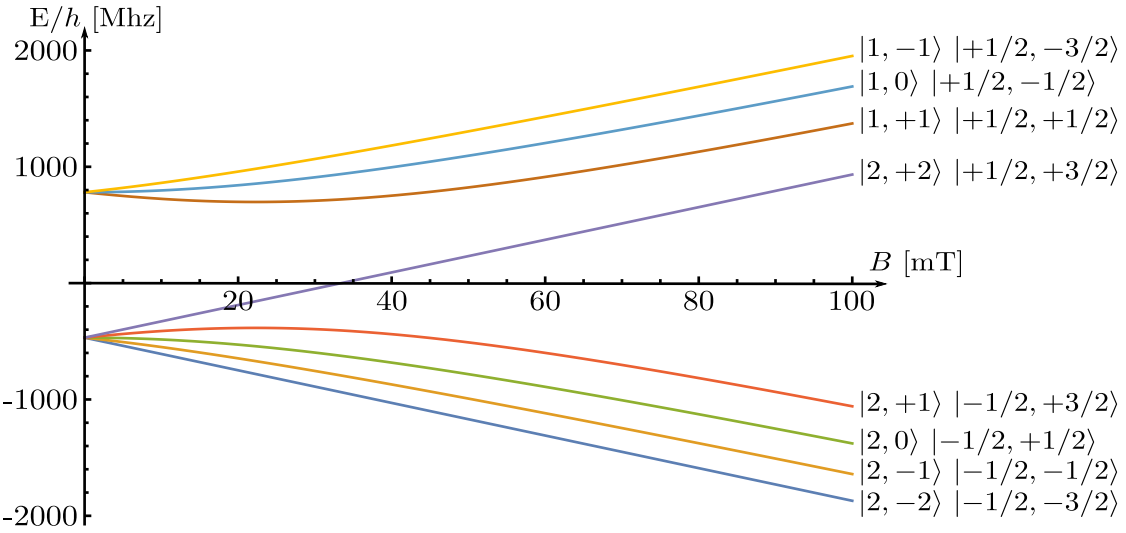

Figure 3.2: Energy levels of the $^2S_{1/2}$ ground state as a function of an external magnetic field determined with the Breit-Rabi formula (eq. (3.4)). The states are given in the $|F, m_F\rangle$ and $|m_J, m_I\rangle$ basis. The former is valid for weak fields in the Zeeman regime, while the latter is a good description for strong fields in the Paschen-Back regime. Here, the labelling is $|F, m_F\rangle$ $|m_J, m_I\rangle$.

analytically with the Breit-Rabi formula:

$$E_B = -\frac{\Delta E_{\mathrm{HFS}}}{2(2I+1)} + m g_I \mu_B B \pm \frac{\Delta E_{\mathrm{HFS}}}{2} \begin{cases} 1 \pm x & m = \pm(I+1/2) \\ \sqrt{1 + \frac{4m}{2I+1}x + x^2} & \text{otherwise} \end{cases} \tag{3.4}$$

where $m = m_I \pm m_J = m_I \pm 1/2$ and x is defined by

$$x = \frac{(g_J - g_I)\mu_B}{\Delta E_{\mathrm{HFS}}} \cdot B. \tag{3.5}$$

ΔE_{HFS} is given by

$$\Delta E_{\mathrm{HFS}} = A \cdot \left(I + \frac{1}{2}\right). \tag{3.6}$$

The $\pm$ in front of the last term in Equation (3.4) refers to $F = I \pm 1/2$. Figure 3.2 shows the resulting energy structure for the $^2S_{1/2}$ state with the different energy slopes in the Zeeman and Paschen-Back regimes. For certain field strengths, sublevels of the hyperfine manifold have the same slope. Hence, the transition between these states is first-order magnetic-field-insensitive. The derivative of the Breit-Rabi formula (Eq. (3.4)) yields the field strengths at which these transitions occur. Besides the point at $B = 0$, four field-independent transitions for $^9Be^+$

exist, listed in Table 3.1. The two-photon transition at low field ($B = 0.0254\,\mathrm{mT}$) known in the context of cold atomic gases in the case of ^{87}Rb, which has the same nuclear spin as $^9Be^+$ [92], but has seen no use in trapped-ion experiments so far. Two of the magnetic-field-insensitive transitions are σ-transitions with $\Delta m_F = \pm 1$ which occur at about 11.9 mT. These transitions are usually chosen as qubits for quantum information processing and simulation with beryllium based on the laser scheme, cf. [87]. In the oscillating magnetic field approach, the radiated field is linearly polarized. Hence, π-transitions with $\Delta m_F = 0$ are favorable. Such a transition exists between $|F = 2, m_F = 1\rangle$ and $|F = 1, m_F = 1\rangle$ at 22.3 mT. We choose $|F = 1, m_F = 1\rangle$ as our spin up state ($|\uparrow\rangle$) and $|F = 2, m_F = 1\rangle$ as our spin down state ($|\downarrow\rangle$). The energy splitting of these states is 1082.55 MHz, a frequency suitable for the oscillating microwave approach. Note that this is the first time that this particular transition has been implemented in an experiment.

Table 3.1: Magnetic-field-insensitive transitions in the $^2S_{1/2}$ hyperfine manifold of $^9Be^+$ at corresponding magnetic field strength B and the corresponding transition frequency.

Hyperfine states	B / mT	f / MHz
$\|2,0\rangle \rightarrow \|1,1\rangle$	11.9446	1207.5
$\|2,1\rangle \rightarrow \|1,0\rangle$	11.9642	1207.35
$\|2,1\rangle \rightarrow \|1,1\rangle$	22.3073	1082.55
$\|2,1\rangle \rightarrow \|1,-1\rangle$	0.0254	1250.02

3.2 Microwave excitation of internal and external degrees of freedom

To implement multi-qubit operations with trapped ions, two different kinds of quantum states are important, the internal state and the motional state. The internal state is given by the level structure of the ion, which is in our case a pair of magnetic sublevels in the hyperfine manifold of the $^2S_{1/2}$ electronic ground state. The motional state is defined by the energy levels of the harmonic oscillator of the trapping potential (Eq. (2.8)). To address the internal state, an oscillatory field matching the energy splitting between the two qubit states is required. Such a transition is called carrier transition. Detuning the oscillatory field by the trap frequency allows for coupling of the internal and motional states by adding or removing quanta of motion while changing the internal state. These kinds of transitions are known as sideband transitions. Figure 3.3 shows the possible transitions. In the near-field approach, the ion interacts with an oscillating magnetic field inducing these transitions. In the following, the interaction with the oscillating magnetic field is described in more detail based on the derivation in [47].

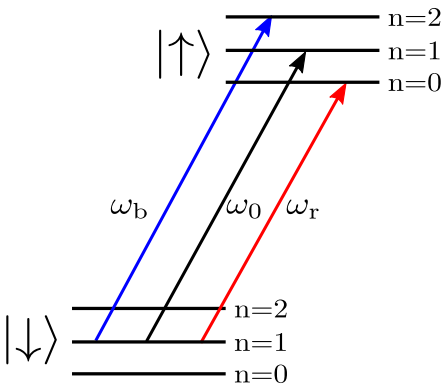

Figure 3.3: Possible transitions between the qubit states. Each of these states exhibits motional degrees of freedom n, whose energies are determined by the trapping potential. Carrier transitions at ω_0 change the internal state only, whereas red/blue sideband transitions at ω_r/ω_b remove/add quanta of motion while flipping the spin.

3.2.1 Interaction with oscillating magnetic field

We will now approximate the trapped ion as a two-level system where the two states are identified with an effective spin-1/2 system or qubit. For a spin-1/2 system in a static magnetic field the Hamiltonian can be written as

$$\mathbf{H}_{\text{int}} = \omega_0 \mathbf{S}_z = \frac{\hbar\omega_0}{2}\boldsymbol{\sigma}_z, \tag{3.7}$$

where $\hbar\omega_0$ is the energy of the eigenstates and $\boldsymbol{\sigma}_z$ a Pauli matrix. Besides the internal state, the trapping potential has to be considered. The Hamiltonian for the trapping potential in the pseudopotential approximation is given by

$$\mathbf{H}_{\text{trap}} = \hbar\omega_z \mathbf{a}^\dagger \mathbf{a}, \tag{3.8}$$

where ω_z is the secular frequency determined by the trapping potential. $\mathbf{a}^\dagger, \mathbf{a}$ are the creation and annihilation operators, respectively. The combined Hamiltonian $\mathbf{H}_0$ of the qubit is

$$\mathbf{H}_0 = \mathbf{H}_{\text{int}} + \mathbf{H}_{\text{trap}}. \tag{3.9}$$

To investigate how an oscillating magnetic field acts on the combined Hamiltonian, we assume the magnetic field driving the transition has a spatial variation along the z-direction:

$$B(z,t) = B(z) \cdot \cos(\omega t + \varphi). \tag{3.10}$$

Here, φ is a phase offset and ω the oscillation frequency. The corresponding Hamiltonian for the magnetic dipole interaction is then given by

$$\mathbf{H}_B = -\mu \boldsymbol{\sigma}_x B(z) \cdot \cos(\omega t + \varphi), \tag{3.11}$$

where μ describes the magnetic dipole matrix moment associated with a transition. Writing the spatial variation of the magnetic field as its Taylor series and using the relation $\boldsymbol{\sigma}_x = \boldsymbol{\sigma}_+ + \boldsymbol{\sigma}_-$ [1] leads to

$$\mathbf{H}_B = -\mu \cos(\omega t + \varphi)(\boldsymbol{\sigma}_+ + \boldsymbol{\sigma}_-) \sum_k \frac{1}{k!} \frac{\partial^k B(z)}{\partial z^k}\bigg|_{z=0} \mathbf{z}^k. \tag{3.12}$$

The position $\mathbf{z}$ in the approximated harmonic oscillator of the trapping potential can be written in terms of creation and annihilation operators:

$$\mathbf{z} = \sqrt{\frac{\hbar}{2m\omega_z}}(\mathbf{a} + \mathbf{a}^\dagger) = z_0(\mathbf{a} + \mathbf{a}^\dagger). \tag{3.13}$$

Using that relation and the definition

$$\Omega_k = -\frac{\mu}{2\hbar} \frac{\partial^k B(z)}{\partial z^k}\bigg|_{z=0} z_0^k, \tag{3.14}$$

the Hamiltonian for the magnetic dipole interaction can be written as

$$\mathbf{H}_B = 2\hbar \cos(\omega t + \varphi)(\boldsymbol{\sigma}_+ + \boldsymbol{\sigma}_-) \sum_k \frac{\Omega_k}{k!}(\mathbf{a} + \mathbf{a}^\dagger)^k. \tag{3.15}$$

In the interaction picture, the Hamiltonian is given by

$$\begin{aligned} \mathbf{H}'_B &= e^{\frac{i\mathbf{H}_0}{\hbar}t} \mathbf{H}_B e^{-\frac{i\mathbf{H}_0}{\hbar}t} \\ &= 2\hbar \cos(\omega t + \varphi) \\ &\quad \times e^{\frac{i\mathbf{H}_{\text{int}}}{\hbar}t}(\boldsymbol{\sigma}_+ + \boldsymbol{\sigma}_-)e^{-\frac{i\mathbf{H}_{\text{int}}}{\hbar}t} \\ &\quad \times \sum_k \frac{\Omega_k}{k!} e^{\frac{i\mathbf{H}_{\text{trap}}}{\hbar}t}(\mathbf{a} + \mathbf{a}^\dagger)^k e^{-\frac{i\mathbf{H}_{\text{trap}}}{\hbar}t}. \end{aligned} \tag{3.16}$$

With the Baker-Campbell-Haussdorff formula[2], the Hamiltonian in the interaction picture is transformed to

$$\mathbf{H}'_B = \hbar \left(e^{i(\omega t+\varphi)} + e^{-i(\omega t+\varphi)}\right) \left(\boldsymbol{\sigma}_+ e^{i\omega_0 t} + \boldsymbol{\sigma}_- e^{-i\omega_0 t}\right) \sum_k \frac{\Omega_k}{k!} \left(e^{-i\omega_z t}\mathbf{a} + e^{i\omega_z t}\mathbf{a}^\dagger\right)^k. \tag{3.17}$$

In the rotating wave approximation, where the rapidly oscillating terms at $\pm(\omega+\omega_0)$ are dropped, the Hamiltonian changes to

$$\mathbf{H}'_B = \hbar \left(\boldsymbol{\sigma}_- e^{i((\omega-\omega_0)t+\varphi)} + \boldsymbol{\sigma}_+ e^{-i((\omega-\omega_0)t+\varphi)}\right) \sum_k \frac{\Omega_k}{k!} \left(e^{-i\omega_z t}\mathbf{a} + e^{i\omega_z t}\mathbf{a}^\dagger\right)^k. \tag{3.18}$$

[1] $\boldsymbol{\sigma}_+$ and $\boldsymbol{\sigma}_-$ are the ladder operators for the Pauli matrices defined as $\boldsymbol{\sigma}_\pm = 1/2[\boldsymbol{\sigma}_x \pm i\boldsymbol{\sigma}_y]$.
[2] Detailed information is given in appendix A

Keeping only the zero and first order terms, the Hamiltonian for the interaction is reduced to

$$\mathbf{H}'_B = \hbar \left(\boldsymbol{\sigma}_- e^{i((\omega-\omega_0)t+\varphi)} + \boldsymbol{\sigma}_+ e^{-i((\omega-\omega_0)t+\varphi)} \right) \left(\Omega_0 + \Omega_1 \left(e^{-i\omega_z t}\mathbf{a} + e^{i\omega_z t}\mathbf{a}^\dagger \right) \right). \tag{3.19}$$

Hence, the interaction of an oscillating field with a trapped ion yields both carrier and sideband transitions. The frequencies Ω_k determined by the definition in Equation (3.14) correspond to the Rabi oscillation rates. This definition identifies the field requirements to drive carrier and sideband transitions with oscillating magnetic fields. Carrier transitions need a field amplitude

$$\Omega_0 = -\frac{\mu B_0}{2\hbar} \tag{3.20}$$

and sideband transitions are induced by the amplitude gradient of the oscillating field:

$$\Omega_1 = -\frac{\mu}{2\hbar} \frac{\partial B(z)}{\partial z}\bigg|_{z=0} z_0. \tag{3.21}$$

Additionally, Equation (3.19) shows that off-resonant carrier transitions can occur as long as a field amplitude is present. To avoid these transitions and purely drive sideband transitions, a field configuration with a high field gradient and a vanishing field amplitude is required. In addition, this requirement suppresses possible AC Zeeman shifts. Besides the strengths of the amplitude and gradient, the Rabi frequencies depend on the dipole matrix element of the qubit transitions. Figure 3.4 shows all possible transitions between the magnetic sublevels in the hyperfine manifold $^2\mathrm{S}_{1/2}$. The corresponding frequencies and dipole matrix elements are listed in Table 3.2.

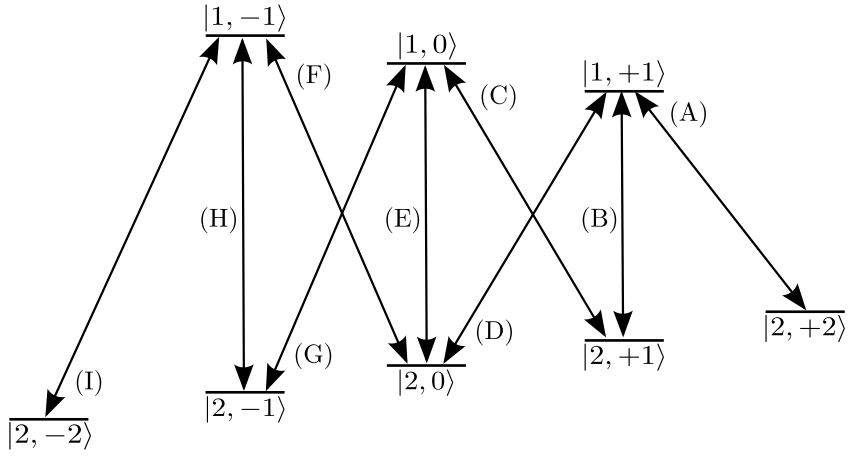

Figure 3.4: Hyperfine levels of the $^2\mathrm{S}_{1/2}$ ground state of $^9\mathrm{Be}^+$. Corresponding frequencies and matrix elements are listed in Table 3.2

Table 3.2: Transitions $|F', m_{F'}\rangle \rightarrow |F, m_F\rangle$ in the hyperfine manifold $^2S_{1/2}$ of $^9Be^+$ at 22.3 mT with corresponding frequencies and magnetic dipole matrix moment μ associated with the transition. μ is calculated by diagonalizing the corresponding Hamiltonian using Wolfram Mathematica.

	$\|F', m_{F'}\rangle$	$\|F, m_F\rangle$	f [MHz]	$\mu_{x,z}/h$ [kHz/mT]
(A)	$\|2, +2\rangle$	$\|1, +1\rangle$	853.64	99.0437
(B)	$\|2, +1\rangle$	$\|1, +1\rangle$	1082.55	-140.091
(C)	$\|2, +1\rangle$	$\|1, 0\rangle$	1239.92	52.0729
(D)	$\|2, 0\rangle$	$\|1, +1\rangle$	1240.19	-84.2739
(E)	$\|2, 0\rangle$	$\|1, 0\rangle$	1397.56	125.301
(F)	$\|2, 0\rangle$	$\|1, -1\rangle$	1525.46	-25.7264
(G)	$\|2, -1\rangle$	$\|1, 0\rangle$	1525.72	111.67
(H)	$\|2, -1\rangle$	$\|1, -1\rangle$	1653.62	91.711
(I)	$\|2, -2\rangle$	$\|1, -1\rangle$	1764.46	131.275

3.2.2 AC Zeeman shift

The AC Zeeman effect describes the energy shift due to off-resonant oscillating magnetic fields. In the hyperfine manifold, such an oscillating magnetic field shifts the energy E_i of sublevel i by

$$\Delta E_i = \frac{1}{\hbar} \sum_j |\langle j|\boldsymbol{\mu} \cdot \mathbf{B}|i\rangle|^2 \left(\frac{1}{\omega - \omega_{ij}} + \frac{1}{\omega + \omega_{ij}} \right), \tag{3.22}$$

if the oscillation frequency ω is detuned from any transition frequency $\omega_{ij} = \frac{(E_j - E_i)}{\hbar}$ [93]. Each allowed transition from sublevel j to sublevel i contributes to the corresponding energy shift. These contributions depend directly on the detuning of the oscillating magnetic field and on the strength of the polarization component of the magnetic field B relevant for each transition. Since the shift is proportional to the magnetic field, this relation can be used to determine the magnetic field by measuring the frequency shift $\delta f_{\mathrm{AC}} = \frac{\Delta E_j - \Delta E_i}{h}$.

For an intuitive picture, we set $i = 1$ and $j = 2$ and assume that the detuning $\Delta\omega = \omega - \omega_{12}$ is small compared to the difference between transitions frequencies. Then the shift can be approximated as

$$\Delta E_1 = \frac{1}{\hbar} |\langle 2|\boldsymbol{\mu} \cdot \mathbf{B}|1\rangle|^2 \left(\frac{2\omega}{\omega^2 - \omega_{12}^2} \right). \tag{3.23}$$

From this relation we obtain that blue-detuned fields ($\omega > \omega_{12}$) yield negative energy shifts and pull the states closer together, whereas red-detuned ($\omega > \omega_{12}$) fields create positive shifts and push the states apart.

3.3 2D microwave near-field model

In the magnetic near-field approach, sideband transitions require a high field gradient and a vanishing field amplitude. Quadrupole-like field configurations meet these requirements. They can be realized by superimposing fields with different orientations. Here, the dimensions of the trap geometry and the ion-to-surface distance are typically small compared to the wavelength. Due to the relatively high microwave frequencies needed for the transitions, the field pattern cannot be described in the quasistatic approximation as it is for the rf field configuration. At microwave frequencies, eddy currents and phase effects cannot be neglected and lead to more complex field patterns.

We developed an intuitive model of 2D microwave fields around a local minimum of the field intensity which allows for evaluating simulated and measured data. In general, the expansion of a 2D oscillatory magnetic field up to first order results in a total of six complex or twelve real-valued expansion coefficients. However, in the case where dimensions are small compared to the wavelength, the following (near-field) conditions apply:

$$\begin{aligned} \nabla \cdot \vec{B} &= 0 \\ \nabla \times \vec{B} &= 0. \end{aligned}$$

Then, the magnetic field is expressed as

$$\vec{B} = \Re\left\{ e^{i\omega t}\Big((B_r \vec{e}_{\alpha_r} + iB_i \vec{e}_{\alpha_i}) + (B'_r Q_{\beta_r} + iB'_i Q_{\beta_i})\,\vec{r} + \dots \Big)\right\}, \tag{3.24}$$

with the following definitions

$$\vec{e}_\alpha \equiv \begin{pmatrix} \cos\alpha \\ \sin\alpha \end{pmatrix} \quad \text{and} \quad Q_\beta \equiv \begin{pmatrix} \cos\beta & \sin\beta \\ \sin\beta & -\cos\beta \end{pmatrix}.$$

Here, $B_{r,i}$ and $\alpha_{r,i}$ characterize the real and imaginary components of the complex field at the origin and their spatial orientation. The parameters $B'_{r,i}$ and $\beta_{r,i}$ describe the real and imaginary components of the complex field gradient and their spatial orientation. The quadrupole matrix Q_β is traceless and symmetric assuming the near-field conditions. As a result of the near-field condition, the number of real-valued parameters is thus reduced from twelve to eight. By multiplying Equation (3.24) with a suitable complex phase factor, the strength B_r of the real part of the gradient can be maximized. Making that specific choice, we obtain the relation:

$$\beta_i = \beta_r + \frac{\pi}{2},$$

and we also write $\{B_r, B_i\} = B\{\cos\varphi, \sin\varphi\}$ and $\{B'_r, B'_i\} = B'\{\cos\psi, \sin\psi\}$. Here, $B, B' \in \mathbb{R}$, $\alpha_r, \beta_r, \psi \in [0, \pi[$ and $\alpha_i, \beta_i, \varphi \in [-\pi/2, \pi/2[$ are suitable domains.

For a field configuration where $|\vec{B}|$ has a minimum at the origin, we obtain the relations

$$\alpha_i - \alpha_r + \frac{\pi}{2} = n\pi, \quad n \in \mathbb{Z}$$

and

$$\varphi = \psi - \frac{\pi}{2}.$$

For our parameter choice, $\alpha_i - \alpha_r + \pi/2$ must be in $]-\pi, \pi[$, thus $n = 0$ and

$$\alpha_i = \alpha_r - \frac{\pi}{2}.$$

Setting $\alpha \equiv \alpha_r$ and $\beta \equiv \beta_r$, the field can be written as

$$\vec{B} = \Re\left\{e^{i\omega t}\left(B\left(\vec{e}_\alpha \sin\psi - i\vec{e}_{\alpha-\pi/2}\cos\psi\right) + B'\left(Q_\beta \cos\psi + iQ_{\beta-\pi/2}\sin\psi\right)\vec{r} + \ldots\right)\right\} \tag{3.25}$$

with five remaining parameters. Here, B and B' are the strengths of the offset field at the origin and of the field gradient, respectively. The spatial orientation of the offset at the origin is given by the angle α, while β describes the angle of the gradient matrix. The latter is shown in the illustration of the 2D quadrupole-like field in Figure 3.5. The last parameter is the angle ψ, which characterizes the ratio of the real to imaginary part and hence determines the polarization, which is set to zero for the illustration in the Figure. The description of the magnetic field $|\vec{B}|$ with Equation (3.25) is only valid for fields with a field minimum at the origin and our special choice of the global phase factor.

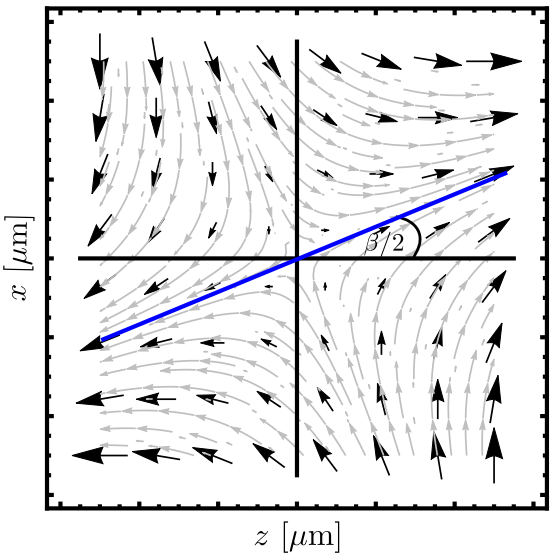

Figure 3.5: Illustration of the 2D microwave near-field model around a magnetic field minimum at $\psi = 0$. The orientation given by the angle β of the gradient matrix is visualized.

Chapter 4

Integrated microwave quantum control

So far, I have discussed surface-electrode ion traps as a scalable platform for quantum information processing and quantum simulation. In most trapped-ion experiments, focused laser beams are used to implement quantum logic operations. These are typically realized using sophisticated and bulky external laser systems. In order to optimally scale the trapped-ion architecture, it would be beneficial if some of the control infrastructure for realizing gates could be integrated into and scaled with the trap structure, as discussed in chapter 1. One way to achieve this is by combining the microwave near-field approach described in chapter 3 with the surface-electrode ion trap architecture described in chapter 2. This approach has been proposed in [47].

A universal set of microwave quantum control gates requires two different kinds of transitions: carrier and motional sideband transitions. As discussed in chapter 3, for state-independent trapping potentials, the former needs an oscillating field amplitude whilst the latter requires a large oscillating amplitude gradient and a vanishing oscillating field amplitude. Carrier transitions can easily be implemented using a single current-carrying electrode embedded into the trap structure. The field of such an electrode oscillates with the driving frequency, enabling transitions between the qubit states. Motional sideband transitions are more difficult to implement. A set of three microwave conductors can provide a field configuration with a high field gradient and a vanishing residual field. The linear superposition of the fields as well as the field configuration are displayed in Figure 4.1. Only the arrangement in which the current in the middle electrode has an opposite sign achieves a vanishing field at a location above the three conductors. In [51], the field configuration was created by carefully balancing currents in three microwave electrodes integrated in a surface-electrode ion trap. By adjusting the amplitudes

and the phases of these currents, the magnetic near-field minimum could be spatially overlapped with the radiofrequency pseudopotential null, the ions' position. The drawback of this approach is that keeping the currents balanced and thereby the field stable during pulse sequences is challenging. Even small relative fluctuations in the currents alter the magnetic field configuration. The ions experience changing residual fields, which lead to off-resonant carrier transitions and AC-Zeeman shifts. If these effects are not reproducible and fluctuate, they cannot easily be compensated. However, using a single-electrode geometry which produces the field configuration by design can stabilize the field. In this chapter the general idea of the single-electrode design is discussed, including the integration of such a design into a surface-electrode ion trap. I present our work on optimizing the combined structure as well as a calibration trap. Note that although the simulations described here are for the 22.3 mT field-independent qubit in $^9Be^+$, they can easily be transferred to other ions with a qubit transition in the few GHz regime. The first section of this chapter has been published in [94].

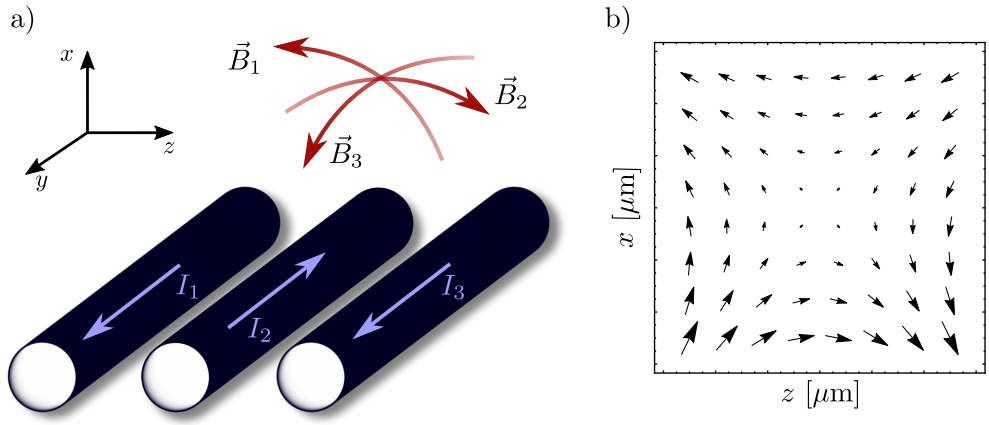

Figure 4.1: a) Arrangement of three conductors to create a magnetic near-field configuration required to drive sideband transitions. The current in the middle electrode has an opposite sign compared to the outer electrodes. Thus, the fields of the outer electrodes cancel the field of the middle electrode and a field minimum at a certain height above the three conductors is obtained. b) shows the magnetic field distribution around a field minimum in a cross-section, the xz-plane, in a). The arrows indicate the strength of the magnetic near-field and its orientation.

4.1 Single-electrode design

Here, I present a design in which a single microwave electrode produces the field configuration for motional sideband transitions by design. This approach provides a microwave near-field with a minimum defined by the trap geometry. Fluctuations

in the current will ideally not change the field minimum and hence the position of the field minimum will be kept stable over time.

For a current distribution which creates a field configuration with a steep gradient and a vanishing magnetic field, I have investigated a geometry laid out like two turns of a meander. The arrangement of a single electrode in a two-turn meander forms a current distribution similar to the three balanced currents of [51]. The only differences compared to a three-electrode design are that the currents in the segments cannot be adjusted separately and that additional fields are provided by the connection segments S_4 and S_5 as shown in Figure 4.2. These additional fields and a non-negligible phase difference between the segments cause a non-vanishing field at the minimum. In general, off-resonant excitation due to this field can be calibrated and accounted for to some extent, as long as it is stable over time. Nevertheless, it is desirable to minimize the residual field at the ion's position.

Figure 4.2 shows the basic idea of our microwave design. For a symmetric configuration ($w_{\mathrm{IE1}} = w_{\mathrm{IE2}}$), by symmetry one would expect the field minimum to appear above segment S_2. Here, one can think of S_2 as producing both the desired gradient and a field in the z-direction. Together, S_1 and S_3 produce a field which counteracts the field in z-direction originating from S_2 while adding to the overall gradient. This is conceptually equivalent to Figure 4.1 a). Typically, the meander structure would be surrounded by two ground electrodes, similar to a coplanar waveguide. Also, the structure is typically fabricated on top of a dielectric substrate placed on a copper heat sink which effectively provides a ground plane and modifies the coplanar waveguide behavior. Before going into the details of the design, let us clarify general design goals and constraints.

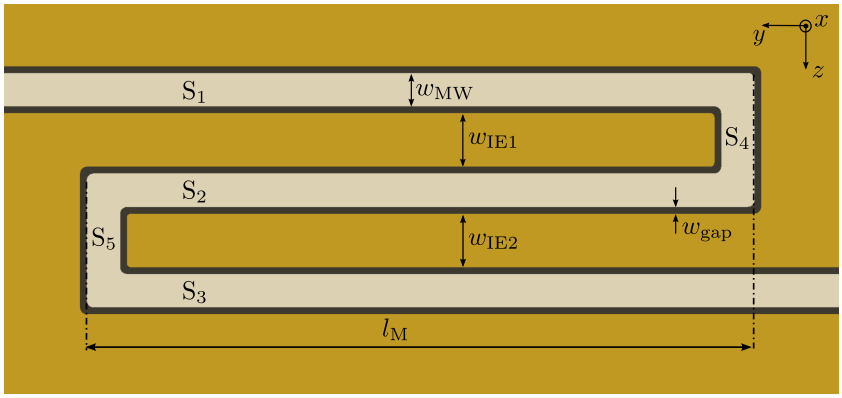

Figure 4.2: Basic idea of a microwave conductor structure for near-field quantum logic operations (top view). The conductor structure consisting of segments S_1– S_5 generates a microwave near-field distribution above the structure. At the minimum of the magnetic microwave near-field, field gradients provide motional-internal couplings ("motional sideband transitions"), whereas oscillating field amplitudes are responsible for parasitic excitations of the carrier.

4.1.1 Design requirements

For our target design, we aim for a distance between the near-field minimum and the surface of the electrode d of about $30\,\mu$m, similar to [51], a compromise between steep gradients, laser access, and motional heating. The gradient increases quadratically with decreasing distance from the surface at the same nominal current, while anomalous heating increases at the same time as d^4 [55]. Ion heating, however, causes motional decoherence and reduces the fidelity of quantum operations involving the motion. An ion-to-surface distance of $30\,\mu$m is a good but challenging compromise. So far, to the best of our knowledge, there is no working surface-electrode ion trap with a distance smaller than this.

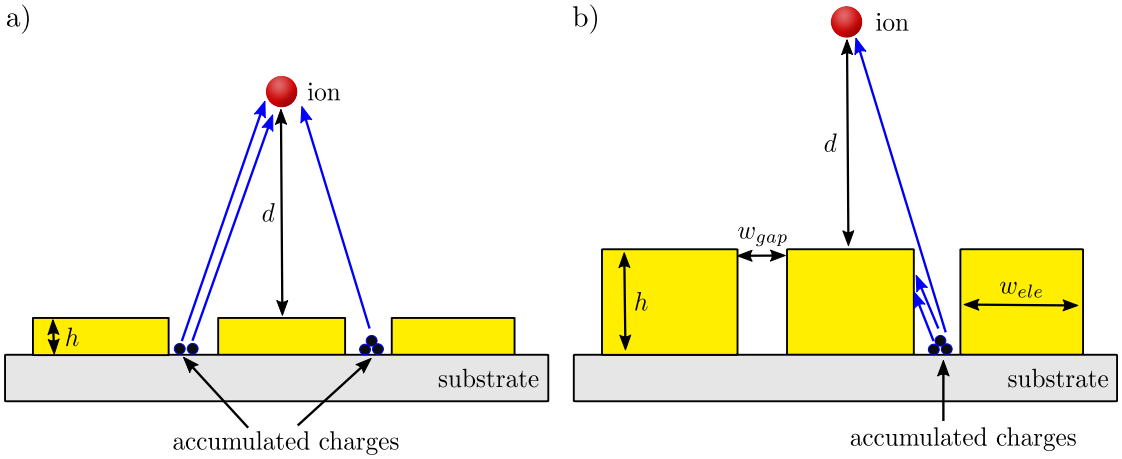

Figure 4.3: Profile of a surface-electrode ion trap showing the trap electrodes on a dielectric substrate. a) shows the profile for a low electrode thickness h and b) that for relatively high electrode thickness. By increasing the electrode thickness while keeping the same ion-to-surface distance d, the same electrode width w_{ele}, and gap size w_{gap}, stray electric fields from accumulated charges on the dielectric substrate can be shielded by the electrodes as indicated in b).

Other constraints arise from insulating surfaces. In general, insulating surfaces close to the ion should be avoided because charges can accumulate in an uncontrolled way. These charges create fluctuating stray electric fields and therefore alter the trapping potential. However, these insulation surface cannot easily be avoided in surface-electrode ion traps with a single-electrode layer. The trap electrodes in a single-layer microfabricated ion trap are located on a dielectric substrate separated by small gaps. A typical gap size is $5\,\mu$m. Figure 4.3 illustrates a cross section of such a trap. To reduce the influence of stray electric fields, a high ratio between electrode and gap width as well as a large ratio of electrode thickness and width is desirable. With our current fabrication process (see appendix B), we can structure electrodes with a thickness of $10\,\mu$m. To achieve a high ratio between electrode and gap width, electrodes with a width of at least $10\,\mu$m are preferred. Smaller

electrodes are difficult to fabricate with our established fabrication process. The amount of dielectric seen by the ion increases significantly if the electrode width is decreased for a given gap size. In the following, an analytic model is used to obtain a first idea about possible electrode sizes to create a field minimum 30 μm above the surface.

4.1.2 Elementary Biot-Savart model

A basic understanding of the magnetic near-field created by the meander segments in the radial plane can be obtained with an elementary Biot-Savart model for static magnetic fields. In this model we consider only the parallel segments S_{1-3} of the meander shown in Figure 4.2. The currents in these segments determine the position of the field minimum in the radial plane. In a meander-like shape currents in neighboring segments have opposite sign. To resemble the meander-like shape in the Biot-Savart model the currents in the three segments have the same amplitude and the current in the middle segments S_2 flows in the opposite direction. The three segments are infinitely extended along the y-axis at positions r_{zi} along the z-axis at and $x = 0$. Each of these segments is modeled using four infinitely thin wires. Two such wires are placed at the edges of the finite conductor, each containing half the conductor current I. To model the current induced in the nearby ground plane, two additional wires that carry currents induced in the edges of the neighboring ground plane are placed on the ground plane on the other side of the gap. For an illustration, see the inset in Figure 4.4. The induced currents are given by $-\alpha I/2$ with $\alpha \leq 1$. The remaining current flows back in parts of the electrode structure far away from the ion (e.g. in the ground plane below the chip), where it has little effect on the near-fields. Here, we use $\alpha = 0.8$, an estimate obtained from earlier near-field simulations [95]. The superposition of all currents provides the magnetic field configuration. The analytic model allows for estimating the position of the magnetic field minimum depending on the electrode width and the distance between the electrodes.

In general, two options for the meander layout are available, a symmetric and an asymmetric one. As a first step, we will discuss the latter in detail as it has been used in the design of [51, 95]. Here, the ground plane between two segments is eliminated, specifically between S_2 and S_3. To obtain this configuration in the above model we set $w_{\mathrm{IE2}} = -w_{\mathrm{gap}}$. As a result, there are only three free parameters left: the gap size w_{gap}, the inter-electrode distance w_{IE1}, and the microwave conductor width w_{MW}. By fixing the gap size to 5 μm, the interplay of the two remaining parameters determines the height of the magnetic field minimum x_{MW} above the surface. Figure 4.4 shows how that height changes with the width of the inner electrode w_{IE1} and the electrode size w_{MW}. The larger w_{IE1}, the higher the position of the magnetic field minimum. A similar behavior can be observed when increasing the width of the electrode w_{MW} at a fixed value for w_{IE1}. The design target of 30 μm

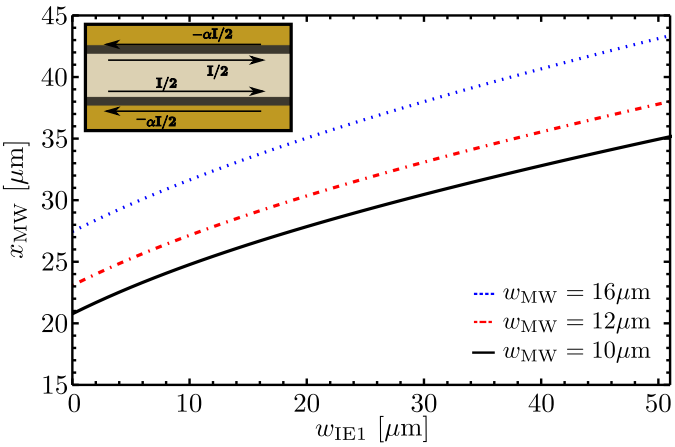

Figure 4.4: Height of the magnetic near-field minimum above the structure of Fig. 4.2 with $w_{\mathrm{IE}_2} = -w_{\mathrm{gap}}$ as a function of the microwave electrode separation w_{IE_1} for different microwave electrode width w_{MW} in a simple analytic model. Inset: Within this model, microwave currents in the surface are modeled by four infinitely thin wires at the edges of the conductor and its neighboring ground planes.

can easily be achieved for electrode widths above 10 μm with the asymmetric layout. In contrast, the symmetric design shows overall higher surface-to-minimum distances than the asymmetric design. To realize the design target with the symmetric design, at least one of the parameters w_{MW}, w_{IE_1}, or w_{IE_2} must be below 10 μm, the lower limit for the electrode width. However, the presented model enables solely the estimation of the meander geometry parameters for specific desired distances of the microwave field minimum from the surface. Determining the field of an oscillating current in the GHz regime requires the consideration of skin and proximity effects as well as a more exact model for induced eddy currents in neighboring electrodes. Though an advanced analytic model might result in a better field calculation, the effort to take all required effects into account is rather high. Instead, we use available numerical simulation tools for an appropriate field characterization and for finding a suitable integrated design.

4.1.3 Near-field simulation

Nowadays, numerical simulations are an efficient and well-established method for designing high frequency structures in research and development. They allow to optimize and investigate a structure without actually building a prototype. Most applications use calibration measurements to estimate the model accuracy and to validate approximations such as boundary conditions. In terms of surface-electrode ion traps with integrated microwave control, so far no actual calibration measurement has been accomplished. Simulations performed in [69, 95] have still a rather high discrepancy between simulation and measurement. However, the

microwave control designed for those traps is based on three independent currents applied to the trap. Each of those currents can be adjusted in phase and amplitude, which allows for compensating any discrepancies from simulations. For the present single-electrode design an accurate model is required. In particular, the position of the magnetic field minimum is relevant in order to realize an overlap with the ion position at the pseudopotential null. In this work, Ansys HFSS is used to establish a model for surface-electrode ion traps. Ansys HFSS is a high-frequency structure solver using finite element methods, usually used to design antenna structures and determine their radiation characteristics. The model of an ion trap with integrated microwave control has somewhat different requirements. The radiated fields are not relevant, but rather the near-fields, especially the fields a few tens of microns above the surface. Here, a resolution of a few microns is required to extract the relevant parameters of the magnetic near-fields. Few-micron resolution is extremely unusual for radiation with a wavelength of about 30 cm. Typically, the meshing and hence the resolution is on the order of one tenth of the applied wavelength. Additional non-modal[1] sheets, segmented air boxes and segmented electrodes with decreasing mesh sizes allow for a mesh size on the order of a few microns at the position of interest within a reasonable computing time. Furthermore, the computing time can be decreased by solving the problem on the surface of the conductors, rather than solving inside their volume. Using Green's theorem [85], volume problems can be translated into surface problems. Nevertheless, solving the model within the volume is more accurate, especially for the model considered here, since the electrode sizes are comparable to the ion-to-surface distance. For rough estimations and for determining the influence of coarse changes to the geometry, the approximation with surface currents is sufficient, whereas volume currents are used to accurately determine the position of the near-field minimum for a final design.

In a first step, the meander-line itself is characterized, followed by adding trap electrodes in a rather basic model. In both cases, gold electrodes with a conductivity of $4.1 * 10^7$ Siemens/m and a thickness of 10 μm are placed onto an aluminum nitride (AlN) substrate with a dielectric constant of $\epsilon_r = 8.8$ at 1 GHz and a thickness of 635 μm, as fabricated. In addition, a part of the chip mount is included and copper is assigned as the material. In the experiment, the copper mount serves as a heat sink and as an additional ground plane. Since the copper mount modifies the microwave propagation it is included here. The structure is excited by a single-mode wave port with an input power of 1 W from a 50 Ω source impedance not matched to the load as in [69]. A second port at the other end of the meander simulates a continuing coplanar waveguide without any termination. The structure is not excited from this port. These assumptions are used as long as the complete structure is not considered. The air box represents the volume in which the problem is solved, in our case a vacuum box with radiation boundary. The

[1] A non-modal object will not be taken into account in the simulation. Regions with different meshing sizes can be specified using such objects.

region of the field minimum is of particular interest, thus an additional non-modal sheet with a 3 μm mesh to increase the accuracy is inserted in the middle of the meander. This is the region where the ion is trapped in the final design. To prevent any meshing errors, an additional vacuum box with a thickness of 10 μm surrounds the sheet. These models are used to observe geometric influences on the near-field quadrupole regarding the position of the field minimum and the ratio of the gradient to the residual field. Here it is sufficient to use the solution based on surface currents, speeding up the characterization. More advanced models will consist of an ion trap chip and part of the connector board. To simplify the simulations, other influences are approximated using boundary conditions. Due to a lack of calibration measurements for ion traps, these approximations might be inaccurate. A calibration measurement of the near-field of one ion trap will overcome this issue. Detailed information on boundary conditions and modifications of the settings described above are given in the particular sections describing the corresponding simulations. For more advanced models, the complete simulation setup is illustrated including ports and boundary conditions. All simulations in this work are carried out using the carrier transition frequency of 1082.55 MHz for the hyperfine qubit of $^9Be^+$ at 22.3 mT, although the sideband transition frequencies are about $\pm$10 MHz shifted from this value. A subsequent frequency sweep provides information about any changes of the quadrupole field due to changes to the frequency of the order a few MHz.

Data analysis

The simulations provide discrete numerical data points for the magnetic near-field on a grid around the near-field minimum. The complex magnetic field is extracted from HFSS around the magnetic near-field minimum and evaluated by fitting a 10th order polynomial to the complex field $\vec{B}$ within a square of 8 μm. The relevant parameters of the quadrupole are obtained by evaluating the fitted data around the field minimum with the 2D quadrupole model, described in section 3.3. Here, only the first order of the Taylor expansion is relevant. To optimize the geometry, a figure of merit η of the near-field is introduced as follows: The speed of carrier transitions induced by the field is proportional to B, the oscillating magnetic field amplitude at the position of the ions. The speed of motional sideband operations, on the other hand, is proportional to the gradient B' of the near-field, multiplied by the motional wave packet size in the ground state, $x_{\mathrm{wp}} = \sqrt{\hbar/(2m\omega_{\mathrm{m}})}$. For $^9Be^+$ and $\omega_{\mathrm{m}} = 2\pi \cdot 5\,\mathrm{MHz}$, one obtains $x_{\mathrm{wp}} \simeq 10\,\mathrm{nm}$, a typical value. Hence the figure of merit is given by

$$\eta = \frac{B' x_{\mathrm{wp}}}{B}. \tag{4.1}$$

This figure gives the ratio of sideband to carrier transition Rabi rates and can be compared to the Lamb-Dicke parameter for laser-induced transitions. Note that

this figure is independent of the current amplitude in the microwave conductor, but it depends on the specific electrode geometry. By maximizing the figure of merit, we can find the optimal geometry for inducing spin-motional couplings by driving sideband transitions.

4.1.4 Meander characteristics

Before integrating the meander into the trap design, the magnetic near-field produced by the meander-line without any trapping electrodes is characterized. Here, the residual field as a function of the length of the meander is of particular interest. This dependence allows us to determine whether the meander shape can produce the desired field configuration. A parametric sweep of the length of the meander from 100 μm to 1000 μm reveals the required information.

Due to the meander shape, an exact magnetic field null cannot be achieved. The connection segments S_4 and S_5 (cf. Fig. 4.2) produce a field pointing along y-direction in the center of the meander. Increasing the length reduces the effect, but then an increased phase shift between the segments S_{1-3} leads to an increased residual field in the xz-plane. The aforementioned parametric sweep of l_M reveals these effects. Figure 4.5 shows the residual field in the radial and axial directions as a function of l_M. The radial component increases slowly with increasing l_M due to the phase shifts whilst the axial component, the contribution from the connection segments S_4 and S_5, decreases. In general, the residual fields for lengths longer than 400 μm are appropriate for driving efficient sideband transitions.

Furthermore, this basic geometry points out the limitations between the analytic model compared to numerical calculations concerning the position of the magnetic field minimum. The discrepancy increases with increasing electrode width. This

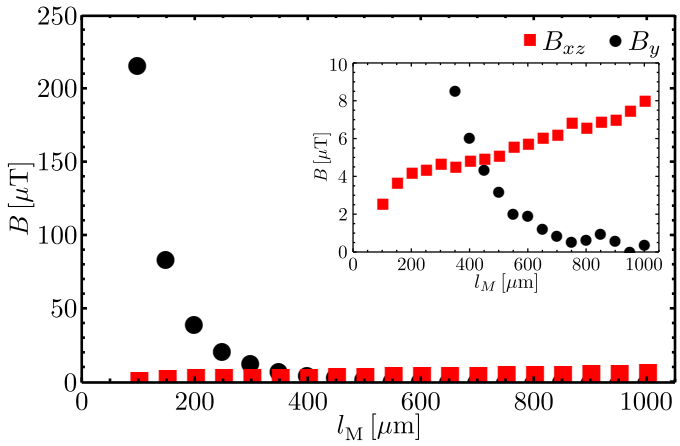

Figure 4.5: Residual field B at the magnetic near-field minimum as a function of meander length l_M. For small lengths, fields originating from the segments S_4 and S_5 (see Fig. 4.2) dominate; for longer lengths, phase retardation leads to a finite field amplitude.

effect can be clearly seen for the asymmetric design (see Fig. 4.6). Induced currents as well as proximity and skin effects are not accounted for properly within the analytic model, leading to an inaccurate prediction for the position of the near-field minimum in the analytic model. Hence, numerical simulations are essential to determine the location of the near-field minimum. The next step is to add additional electrodes for trapping. At a frequency of about 1 GHz, induced currents in these neighboring electrodes affect the near-field behavior significantly.

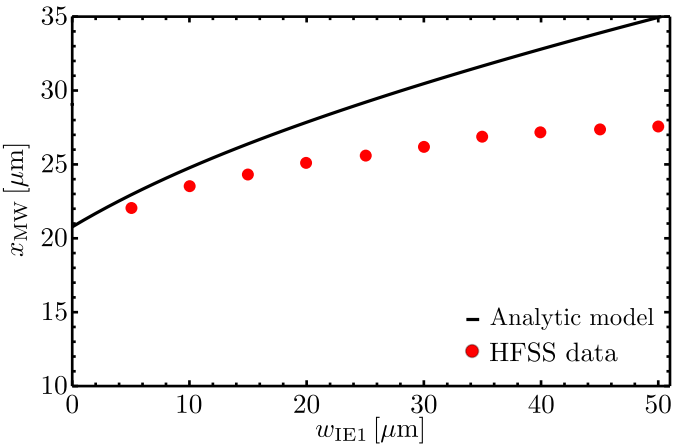

Figure 4.6: Comparison of the near-field minimum height x_{MW} above the electrode surface obtained from the simple Biot-Savart model and from numerical simulations, respectively. While the analytic models provides an exact field-zero, the position of the minimum in the numerical simulation is extracted from a 10th order polynomial fit to the data. The size of the microwave electrode is fixed to $w_{\mathrm{MW}} = 10\,\mu$m. The values are obtained for the asymmetric design.

4.1.5 Adding trap electrodes

Figure 4.7 shows a sample surface-electrode ion trap design with an integrated meander conductor. We investigate potential arrangements of the conductor and the necessary trapping electrodes. Since the microwave electrode contains three parallel segments, rf and dc electrodes can easily be arranged around and between the meander segments. Here, all configurations were designed to have at least three independent rf electrodes to be able to adjust the rf pseudopotential null for an overlap of the magnetic and electric field quadrupoles, should this be required. The configurations considered here are shown in Figure 4.8. The symmetric design and one asymmetric design provide an additional rf electrode. In every configuration, six dc electrodes, three on each side of the meander as indicated in Figure 4.7, supply the axial confinement. Each configuration is implemented in a simple model in HFSS taking only the central trap area with the ground plane into account, as shown in Figure 4.9. Here, for the purpose of the microwave simulations, the

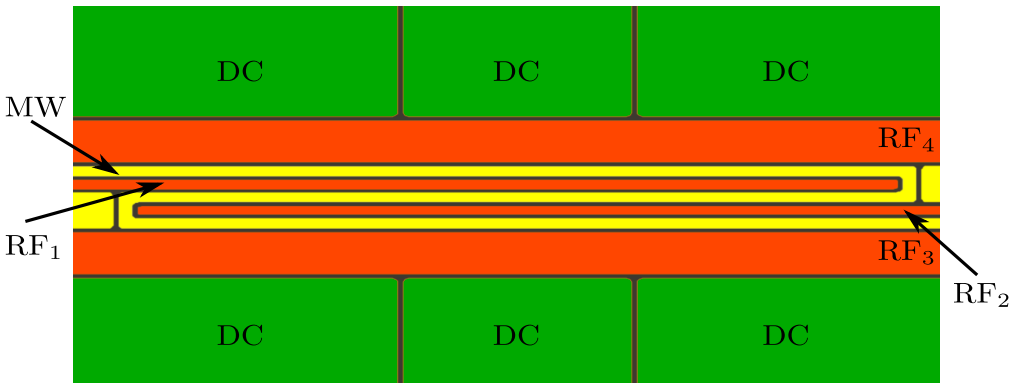

Figure 4.7: Sample design configurations for integrating the meander electrode into a linear Paul trap. A symmetric design exhibits four rf electrodes (red) and six dc electrodes (green) which surround the meander (yellow).

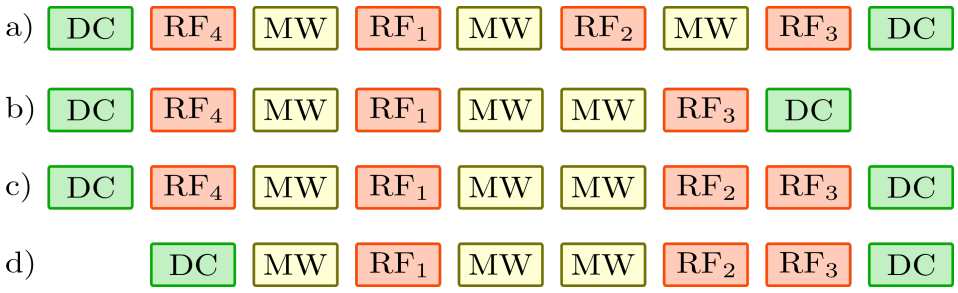

Figure 4.8: Cross section of possible configurations for integrating the meander electrode into a linear Paul trap. Configuration a) is a symmetric design, while b)-d) are asymmetric designs. All configurations have at least three rf electrodes to fine-tune the position of the rf null. Configurations a) and c) have an additional electrode which can also be used as a microwave carrier electrode.

electrodes are assumed to be floating. This model is sufficient for studying the general influence of additional electrodes on the near-field provided by the meander electrode. The near-field is extracted from the area indicated with ($\star$). We optimize each structure in Figure 4.8 by varying the relevant parameters individually and observing the behavior of the height of the minimum x_{MW} and the figure of merit η. The results are used to determine which of these configurations supplies the best magnetic near-field configuration considering the figure of merit at a ion-to-surface distance of at least 30 μm. Here, the rf electrodes are treated as individually adjustable electrodes, but can however be exchanged for a configuration where two of them are connected to a common rf source and one is held at ground. A typical surface current distribution and the resulting magnetic near-field for one possible configuration are shown in Figure 4.10. The eddy currents in the neighboring electrodes are clearly identifiable. Hence, the electrode width of the outer rf electrodes also alters the field configuration.

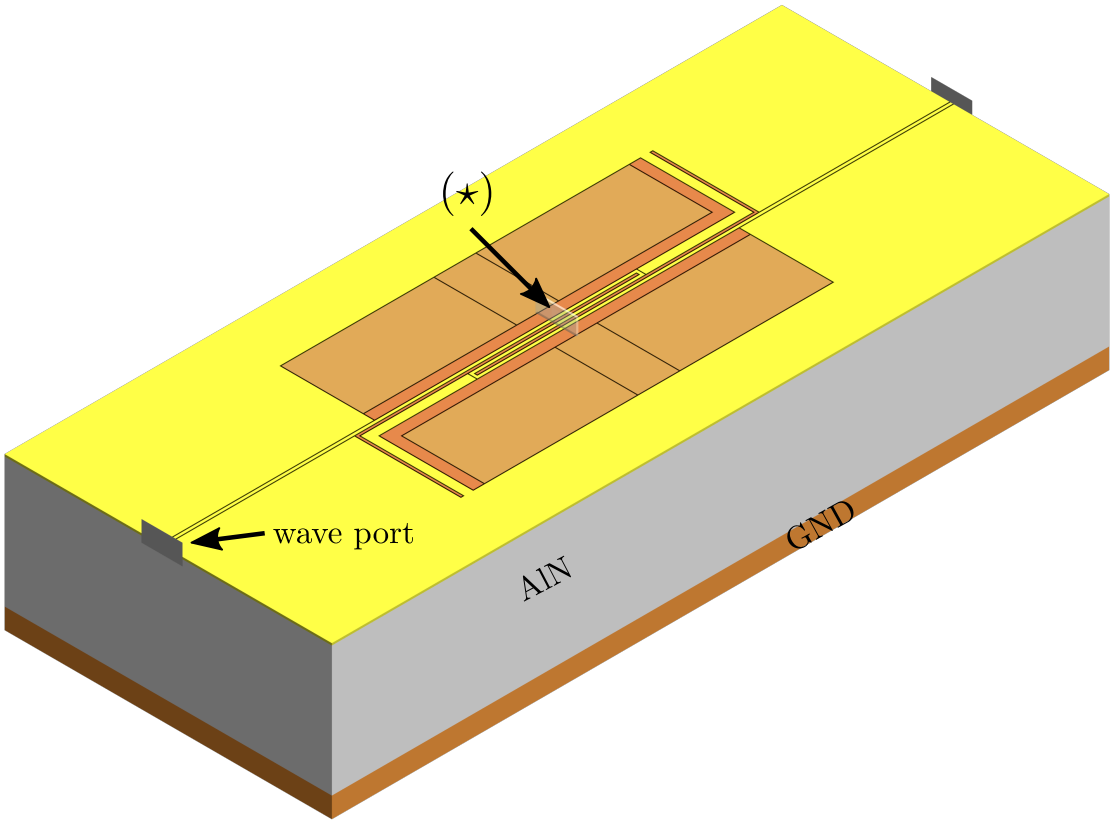

Figure 4.9: Simulation setup of the simple model, showing the symmetric design. Only parts of the electrodes are included in the simulation. This approximation speeds up the computation. The model is excited at the wave port and evaluated in the trapping center, indicated with (⋆). Besides the geometric structure, ground plane (GND) and substrate (AlN) are shown.

The parametric analysis reveals that adding electrodes dramatically influences the near-field minimum height. Previous results favored an asymmetric meander design. However, the current distribution with additional electrodes lowers the height of the field minimum in such a way that the symmetric design becomes favorable. Optimizing the asymmetric design is rather difficult. To achieve a height of $x_{\mathrm{MW}} > 30\,\mu\mathrm{m}$, the width of the electrodes, specifically the meander electrode, should be increased to at least $w_{\mathrm{MW}} = 20\,\mu\mathrm{m}$. However, increasing that electrode width decreases the figure of merit η. Maintaining the design requirements, the best value obtained out of all asymmetric designs is $\eta \approx 0.01$. Better figures of merit are only obtained by significantly decreasing the field minimum height. The symmetric design, on the other hand, does not result in heights below $30\,\mu\mathrm{m}$ when assuming minimal electrode widths of $10\,\mu\mathrm{m}$. Specifically, a configuration with $w_{\mathrm{MW}} = w_{\mathrm{RF_1}} = 10\,\mu\mathrm{m}$ achieves a height of $\approx 30\,\mu\mathrm{m}$ with a figure of merit

$\eta > 0.02$. Conclusively, the symmetric design gives the best results for a ion-to-surface distance $x_{\mathrm{MW}} > 30\,\mu$m. An optimization of the symmetric design reveals the general dependence of the figure of merit on the geometric parameters of the trap. The distance between meander segments S_{1-3}, which is the width of the rf electrodes w_{RF_1} and w_{RF_2} in this configuration, has the strongest influence on the figure of merit; the field is minimized for an electrode width of $w_{\mathrm{RF}_1} = 8\,\mu$m. Small deviations from the optimal value cause a large reduction of the figure of merit. All other parameters have minor influence. For example, the width of the meander electrodes w_{MW} has no significant influence; increasing the width leads to a slightly lower figure of merit. While the parameters w_{MW} and w_{RF_1} should be smaller for a good η, the widths of the outer electrodes w_{RF_3} and w_{RF_4} should be bigger for a good η (cf. Figure 4.8 a)). Although the simple model gives only an approximation of the near-field configuration, it reflects the general dependence of η and the position of the magnetic near-field minimum on geometric changes.

Based on these results, an ion trap with three adjustable rf electrodes and an additional microwave electrode for carrier transitions was designed. The width w_{RF_3} is adjusted to achieve a rough overlap of the trapping position with the magnetic-near-field minimum when only electrodes RF_1 and RF_3 are used. Slightly adjusting the voltage of one of the rf electrodes allows for fine-tuning of the ion's

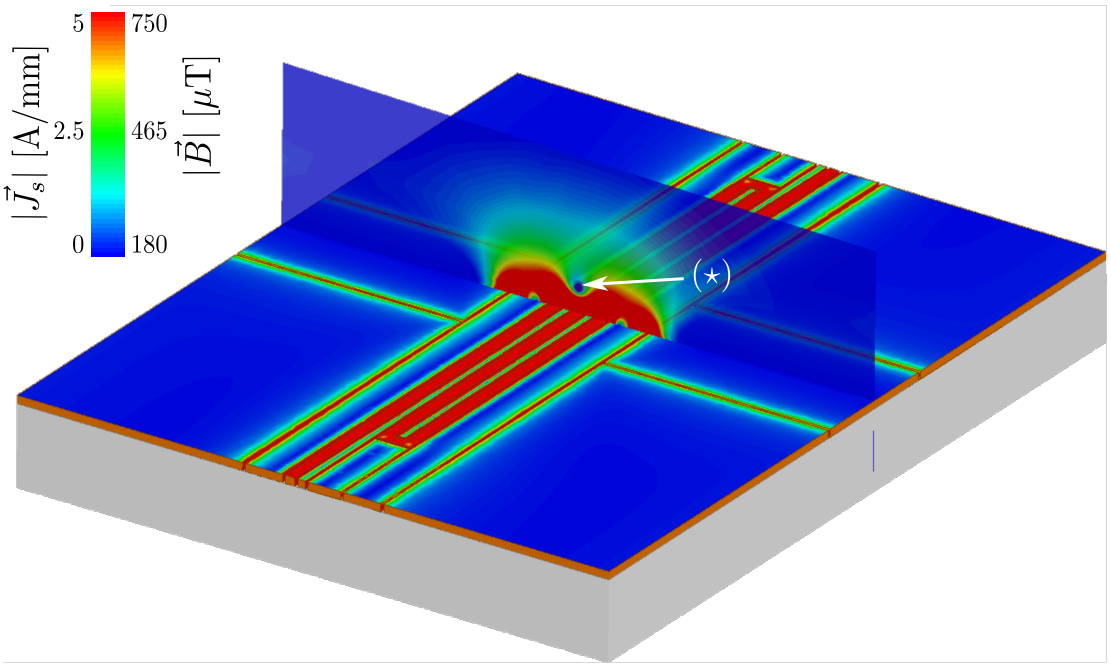

Figure 4.10: Surface current distribution $\vec{J}_{\mathrm{s}}$ in the symmetric design with the resulting magnetic near-field $\vec{B}$. The induced current in neighboring electrodes changes the magnetic near-field configuration, especially the position of the field minimum, indicated with ($\star$).

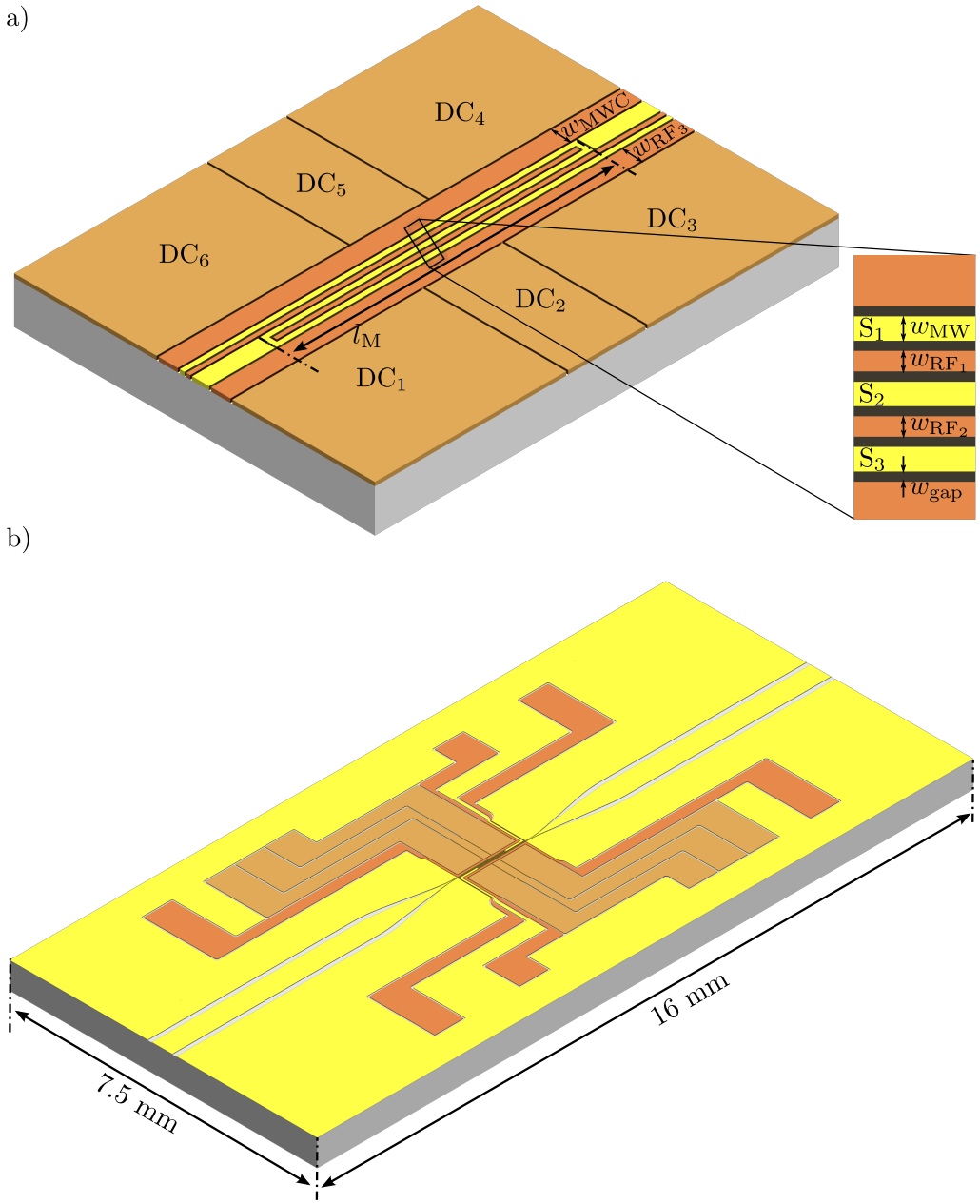

Figure 4.11: Full trap design, including rf and dc electrodes for a linear Paul trap. Three individually adjustable rf electrodes RF_{1-3} define the position of the trapped ion in the radial direction, while the six dc electrodes DC_{1-6} confines the ion in the axial direction. The additional electrode is used as a microwave carrier electrode, labeled MWC. The inner part of the trap in a) is optimized using parametric sweeps, and the electrodes are then extended to a full chip (b). The right-hand side in a) shows a zoom-in on the central trap area.

position in the calculation and also in the experiment. Hence, deviations from the simulated magnetic near-field minimum position, due to the simplicity of the model and neglected proper boundaries and feed lines, can be compensated in the experiment. Figure 4.11 a) shows the layout of the inner part of the trap. The fourth electrode can be used as an rf or microwave carrier electrode. For this purpose the feed lines are extended to both sides, to enable connecting the electrode on one side and grounding it on the other side if used as microwave carrier electrode. The arrangement of electrodes DC_{1-6} is adjusted considering the results of parametric sweeps and trap design demands. Setting $w_{\mathrm{MW}} = 12\,\mu\mathrm{m}$, $w_{\mathrm{RF_1}} = 10\,\mu\mathrm{m}$, $w_{\mathrm{RF_3}} = 50\,\mu\mathrm{m}$, $w_{\mathrm{gap}} = 5\,\mu\mathrm{m}$, and $l_{\mathrm{M}} = 850\,\mu\mathrm{m}$ leads to a figure of merit of $\eta \approx 0.032$ at a position of $x_{\mathrm{MW}} = 31.6\,\mu\mathrm{m}$. The trap electrodes are expanded to a chip with a size of $7.5 \times 16\,\mathrm{mm}$. The length of the trap is chosen in order to adopt a coplanar waveguide behavior, although it is not the best choice regarding laser access. The feed lines of all other electrodes are arranged as depicted in Figure 4.11 b) to provide laser access, at least along the short side of the trap, important for cooling and imaging. This trap exhibits a relatively unconventional feature: the fine-tuning the position of the rf pseudopotential null by individually adjusting the voltages on the rf electrodes. Only a few groups have so far implemented on-the-fly variable pseudopotential configurations as discussed here [96, 97, 98]. Since a drive system with this capability is still under development in our group, we bonded two rf electrodes (RF_1 and RF_3) together while grounding RF_2 and used a single rf drive to test the trapping procedure with this trap. While we loaded our first $^9Be^+$ ions in a trap of this design, it had a few important shortcomings such as the size of the chip and the connection of the rf electrodes. In the following section an alternative design is discussed.

4.2 SpyderTrap

The trap presented here is an enhanced version of the symmetric design discussed in section 4.1.5. The symmetric design features the possibility to fine-tune the position of the rf pseudopotential null by adjusting the voltages on one of the three rf electrodes, enabling the overlap with the magnetic field minimum. Because the rf drive for individually adjustable rf electrodes is not fully developed yet, we eliminate that feature in the new trap design, known as SpyderTrap, and use a single rf drive to provide the trapping potential. The rf electrode is hence divided into two segments in the central trap area of the chip, similar to other microfabricated trap designs. Now, an adjustment of the overlap of the near-field minimum and the rf null position is not possible. The overlap is determined purely by design, which means that a more accurate model to determine the position of the magnetic near-field minimum is essential. Here, a more advanced model is developed including the full chip design and additional boundary conditions for the electrodes. However, prior to this project, there was no experience in how accurately the position of the

microwave near-field minimum could be determined by simulations. To overcome this drawback, a calibration trap is introduced. The comparison of simulated and measured near-fields of this trap reveals insight into appropriate boundary and simulation settings. First, the trap design and the optimization of the trap design regarding the near-field configuration for sideband transitions are performed.

4.2.1 Trap design

The structure of the SpyderTrap resembles the design of the symmetric trap with some modifications. Figure 4.12 a) illustrates the trapping zones with all electrodes. The rf potential is given by a single segmented electrode providing the radial confinement while six dc electrodes DC_{1-6} provide the axial confinement. Furthermode, these six electrodes are used to overlap the position of the ion with the rf pseudopotential null and hence compensate micromotion. The rf electrode (RF) is arranged between the parallel segments of the meander. Due to the reduced number of rf electrodes and a symmetric layout of the meander, two additional electrodes are available. One is used as the microwave carrier electrode (MWC), the other is part of the ground plane. The illustration reveals a connection of both microwave electrodes to the ground plane at the end of the central trap area. We ground the meander as close as possible to the trap center to eliminate any phase differences between the applied and the back-reflected electromagnetic waves. Furthermore, the electric length and hence the inductance of the meander is reduced.

To investigate the behavior of the magnetic near-field generated by the meander electrode in the SpyderTrap, the whole chip design is included in the numerical simulation. The electrodes are extended to the edge of the chip as shown in Figure 4.12 b). To achieve a symmetric current distribution in the meander, the complete chip is designed to be as symmetric as possible. The meander feed line is tapered from the edge to the chip center to avoid back-reflections due to sudden impedance jumps. The neighboring ground planes model the input of the meander as a coplanar waveguide. The ground plane is not segmented to emulate this behavior. The total chip size is reduced to $5 \times 5\text{mm}^2$, a size allowing for laser access in all directions. Since an ion-to-surface distance of $30\,\mu$m is favored, an extension of the size might lead to clipping of the laser beams at the edge of the trap. For the lasers used in our experiment (313 nm and 235 nm), the size should be below 7.5 mm to avoid any clipping, though smaller is better.

4.2.2 Optimized design

Here, I will describe the final result of the optimization of the SpyderTrap design. To gain insight into the geometric parameters and the performance achievable in principle, we optimize the trap structure solely with respect to the figure of merit

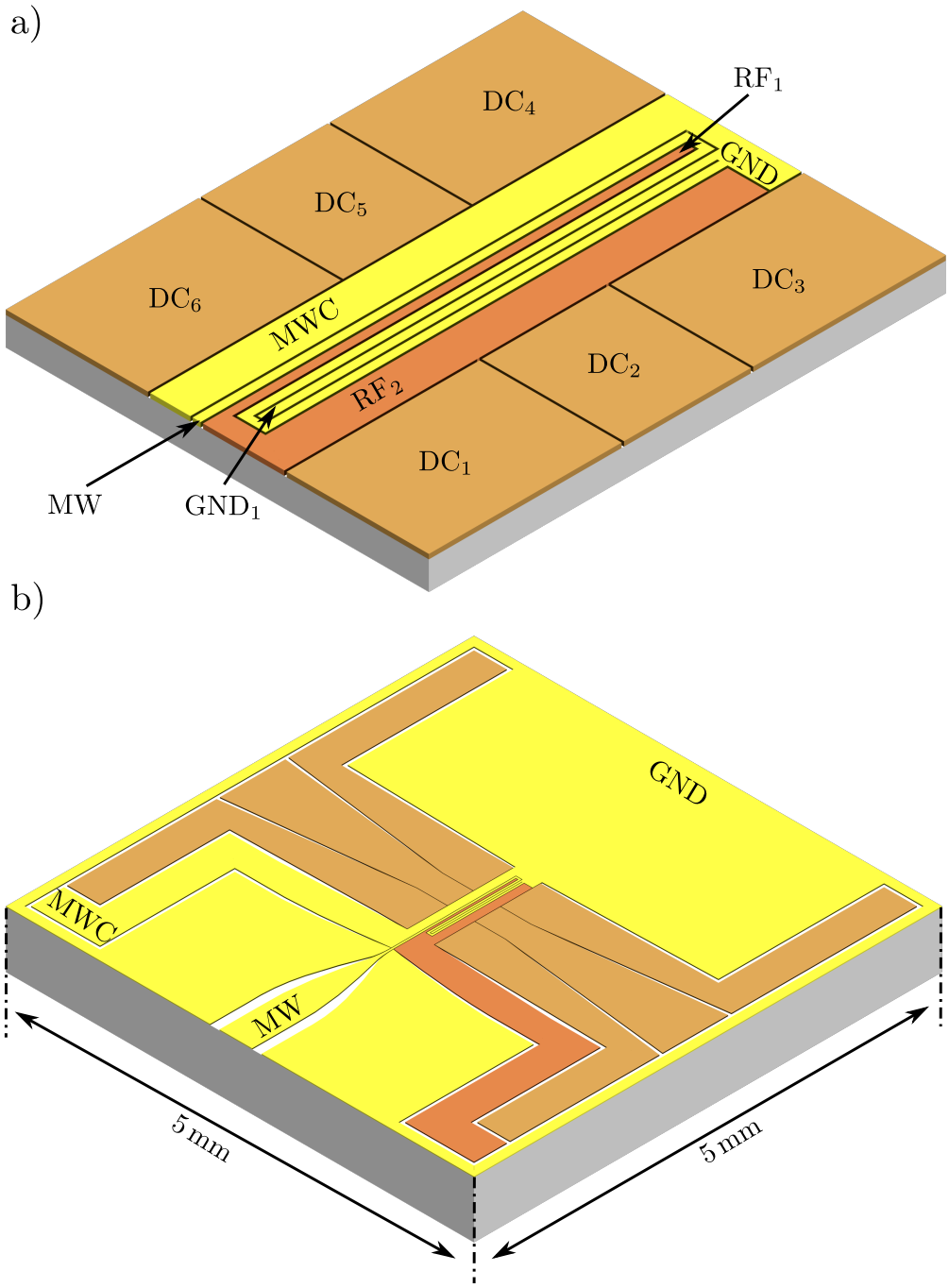

Figure 4.12: SpyderTrap design including trapping and microwave electrodes. a) shows the central trap area. Here, a single segmented rf electrode (RF) provides the radial confinement by design. The additional electrodes are used as microwave carrier and ground electrodes to maintain the symmetry. Both microwave electrodes are grounded on the chip. These electrodes are extended to a $5 \times 5\,\mathrm{mm}$ chip, and the ground plane is a single electrode as shown in b). Part of the aluminum nitride substrate is included here.

η introduced in Eq. (4.1), which basically gives the ratio of sideband to carrier transition Rabi rates. Note that hence only a coarse agreement between the location of the microwave minimum and the rf pseudopotential null is achieved. Also, we still assume floating as boundary conditions for the trapping electrodes and the microwave carrier electrode. In order to fully optimize the overlap of the microwave minimum with the pseudopotential null and take into account boundary conditions properly, more elaborate simulations will be required which will involve compromises concerning the achievable figure of merit. These more elaborate simulations will be described in the subsequent section 4.2.3. Here, solely the geometric influences are determined. This approach might give slightly inaccurate results, but simplifies the optimization. Although similar simulations have been performed in section 4.1.5, we investigate the complete geometric dependence once more. The fact that the microwave electrodes are now directly grounded on the chip surface itself at the edge of the central trap area and not on the filter board as previously implemented, as well as the replacement of one of the former rf electrodes by a grounded patch changes the current distribution and hence the magnetic near-field. The simulation model is set up in HFSS similar to the model discussed in section 4.1.4. We model here the complete chip design even though the geometric dependence could be obtained with a simple model including only the trap area. The meander in the design seen in Figure 4.12 b) is excited with a wave port. The materials assigned are again those used in our fabrication procedure (cf. section 4.1.3). Furthermore, the solution is obtained with the assumption of surface currents since the exact position of the near-field minimum is not required for optimizing just the figure of merit. The deviation from using volume currents is less than $1\,\mu$m, and adding boundaries changes the position by a significantly higher value. To speed up the computation time for simulation, the electrodes are segmented into an inner and outer part. A finer mesh is applied on the inner part, the central trap area, to increase the accuracy, while the mesh for the outer part is coarser to speed up the computation time. To optimize the near-field configuration, a parametric sweep for every individual electrode width of the rf and microwave electrodes is performed. Determining the influence of each electrode results in an optimal configuration for certain ion-to-surface distances, here $30\,\mu$m.

As already seen from previous simulation results, the position of the near-field minimum depends mainly on the width of the meander electrode and the distances between the individual segments, here represented by the electrodes MW, RF_1 and GND_1. The distance between the surface and the field minimum increases with each of these parameters. The same is in principle true for the electrodes RF_2 and MWC, even though the position of the near-field minimum shift here is about a factor of 10 smaller compared to the shifts corresponding the other parameters. Altering MW, RF_1 and GND_1 by $1\,\mu$m shifts the field minimum height by approximately $1\,\mu$m. A similar behavior is found for the gap size: increasing the value leads to an increase of the surface distance. Figure 4.13 shows the variation of the height depending on

the width of electrode RF_1. Due to the symmetric arrangement, GND_1 changes simultaneously. Here, the other parameters are set to: $w_{\mathrm{MW}} = 12\,\mu$m, $w_{\mathrm{gap}} = 5\,\mu$m and $w_{\mathrm{RF_2}} = w_{\mathrm{MWC}} = 50\,\mu$m. The desired position of the field minimum is reached by choosing $w_{RF_1} = 10\,\mu$m, which is already on the lower end of our fabrication range. In total, the position in the x-direction increases by increasing any of the available parameters. Note that so far, we have not constrained the pseudopotential null yet, which varies as a function of the parameters just like the microwave field minimum.

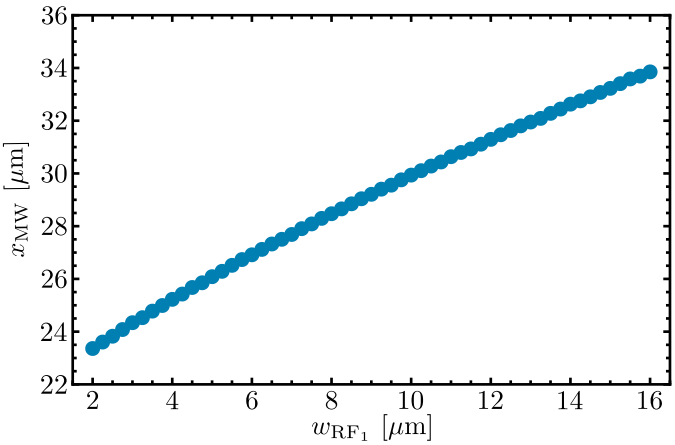

Figure 4.13: Height of the magnetic near-field minimum x_{MW} as a function of the electrode width $w_{\mathrm{RF_1}}$. The widths of electrodes RF_1 and GND_1 change simultaneously. Although an electrode width below $10\,\mu$m is difficult to fabricate, $w_{\mathrm{RF_1}}$ ranges from 2 to $16\,\mu$m to get an idea of the influence of that parameter. For $w_{\mathrm{RF_1}} \approx 10\,\mu$m a height of $x_{\mathrm{MW}} \approx 30\,\mu$m is feasible. Here, the size of the meander electrode is fixed to $w_{\mathrm{MW}} = 12\,\mu$m.

We optimize the near-field by maximizing the figure of merit η, the ratio of gradient and residual field. The parametric sweeps reveal a minor influence of w_{MW}. Changing that width alters the gradient and likewise the residual field, hence the choice of w_{MW} can be specified to adjust the position of the field minimum. Although the figure of merit increases with an increased gap size w_{gap}, the gap size is fixed to $w_{\mathrm{gap}} \approx 5 - 6\,\mu$m to shield electric stray fields created by accumulated charges on the dielectric. Sweeping $w_{\mathrm{RF_2}}$ in a range from 10 to $70\,\mu$m shows an increase of the figure of merit with increasing width. The remaining parameter $w_{\mathrm{RF_1}}$ has the strongest influence on the figure of merit. Specifically, the residual field shows a minimum for an electrode width of $w_{\mathrm{RF_1}} = 6\,\mu$m. Small deviations from the optimal value cause large deviations of the figure of merit. Both behaviors are shown in Figure 4.14. This behavior is slightly different from the results obtained for the simple model described in section 4.1.5. The value for the field minimum shifts to an even smaller value. The reason for this is the grounded meander electrode. Repeating the simulation for the simple model with a grounded meander yields approximately the same results. Nevertheless, with such an electrode size

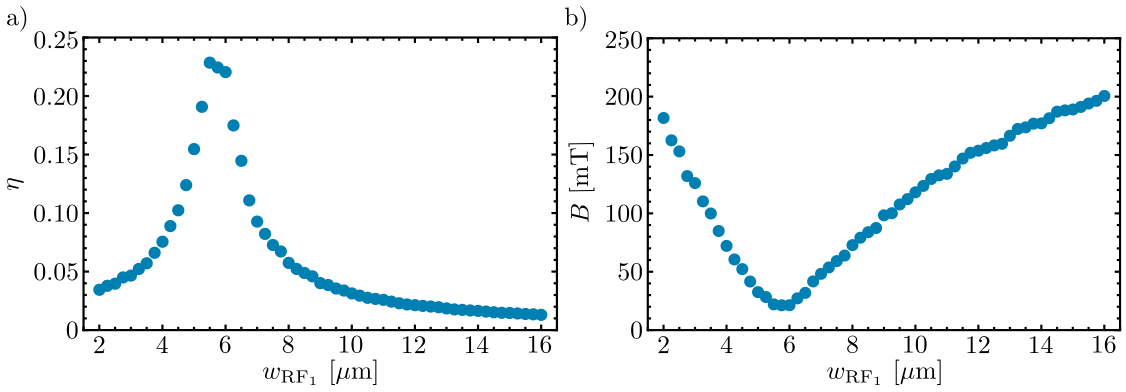

Figure 4.14: Influence of the electrode width w_{RF_1} on the residual field (b) and the figure of merit η (a) of the magnetic near-field. A field minimum at $w_{\mathrm{RF}_1} = 6\,\mu$m leads to a maximum of the figure of merit.

the minimum height of $x_{\mathrm{MW}} = 30\,\mu$m is not reached; furthermore, our fabrication process is not able to build such small electrodes. The best parameter set for our design requirements is $w_{\mathrm{RF}_1} = w_{\mathrm{GND}_1} = 10\,\mu$m, $w_{\mathrm{MW}} = 12\,\mu$m, $w_{\mathrm{gap}} = 5\,\mu$m and $w_{\mathrm{RF}_2} = w_{\mathrm{MWC}} = 70\,\mu$m with a figure of merit of $\eta = 0.04$ at $x_{\mathrm{MW}} = 31.2\,\mu$m for a meander length of $l_{\mathrm{M}} = 800\,\mu$m. Note that in principle, it is possible to achieve an overlap of the pseudopotential minimum and the near-field minimum for arbitrary ion-to-surface distances. However, the resulting widths for RF_2 and MWC can become unphysically large. It is a lucky coincidence that for $30\,\mu$m ion-to-surface distance, we can find a configuration with a coarse overlap (again, not considering proper boundary conditions yet) with a reasonable width of MWC and RF_2. Improving the fabrication process might reduce the possible electrode width to about $8\,\mu$m. The field minimum height can then be adjusted by increasing the meander electrode width to $w_{\mathrm{MW}} = 14\,\mu$m. The figure of merit is then $\eta = 0.11$ and the field minimum height is $x_{\mathrm{MW}} = 31.5\,\mu$m. Before finalizing this design a calibration trap with the same geometry but different electrode sizes was developed. Here, the boundary conditions are added and the position of the rf pseudopotential null is overlapped with the field minimum, as described in the next section.

4.2.3 Calibration trap

Instead of using an optimized design for calibrating the simulation in terms of boundary conditions, a more conservative design is used, both in terms of the fabrication requirements and the distance to the surface. After some previous inconclusive experience with the symmetric design (cf. section 4.1.5), we wanted to ensure we would not run into issues related to stray light from laser beams grazing across the surface in this trap. The SpyderTrap design is hence modified to trap not $30\,\mu$m, but $45\,\mu$m above the surface. The purpose of the calibration

trap is an implementation of the microwave control with microwave transfer pulses and Rabi oscillations on the qubit transitions. Furthermore, a magnetic near-field measurement provides insight into the boundary conditions for the simulation model. A comparison of simulation and measurement improves the understanding of the boundaries and yields an enhanced model, better reflecting the actual near-field configuration. To achieve an acceptable overlap between the magnetic near-field minimum and the rf pseudopotential null, the boundary conditions for the electrodes are added to the model, as described in the following.

Adding boundary conditions

Assigning boundary conditions to the electrodes implies an understanding of the electrical connection of each electrode in an actual experiment. To apply a proper dc signal to the electrodes DC_{1-6}, low pass filters eliminate oscillating signals with a frequency higher than approximately 1 MHz depending on the low pass filter composition. These filters prevent any rf or microwave signal from reaching the dc electrodes. That way, the electrodes DC_{1-6} appear as grounded for those signals. The appearance of the rf connection for the microwave is mainly a short circuit with some minor impedance, since the rf electrode is connected with a copper feedthrough to a helical resonator whose end is grounded. A microwave electrode, on the other hand, is usually coupled to a $50\,\Omega$ line, the impedance used by commercially available microwave components. To take all of those connection properties into account, a connection board is modeled in HFSS. This board surrounds the trap on three sides and is made of RO4350B, a common substrate material for microwave applications. On the substrate, gold patches connected to ground via impedance sheets are placed. These sheets resemble the actual connections using appropriate boundary conditions. Bond wires connect each electrode with the corresponding gold patch. Figure 4.15 shows the complete simulation model. The boundary for the microwave carrier electrode sheet is set to $Z_{\mathrm{MW}} = 50 + i0\,\Omega$ while we assume an impedance of $Z_{\mathrm{RF}} = 0 + i50\,\Omega$ for the rf electrode. The sheets connecting the ground and dc electrodes have a boundary condition for a finite electrical conductor realizing a direct ground connection. The finite conductor has the properties of gold. As in previous simulations, the model is solved in a vacuum box and the materials are again assigned as used in the fabrication process (cf. section 4.1.3). We add an additional virtual air box with vacuum properties to improve the meshing in the trap center and hence the accuracy. However, without any calibration measurement of the magnetic near-field, no accurate model of the connections is possible.

Overlap of electric and magnetic field

Using the model described above with additional boundary conditions, a second parametric sweep set is performed to estimate the distance of the microwave near-

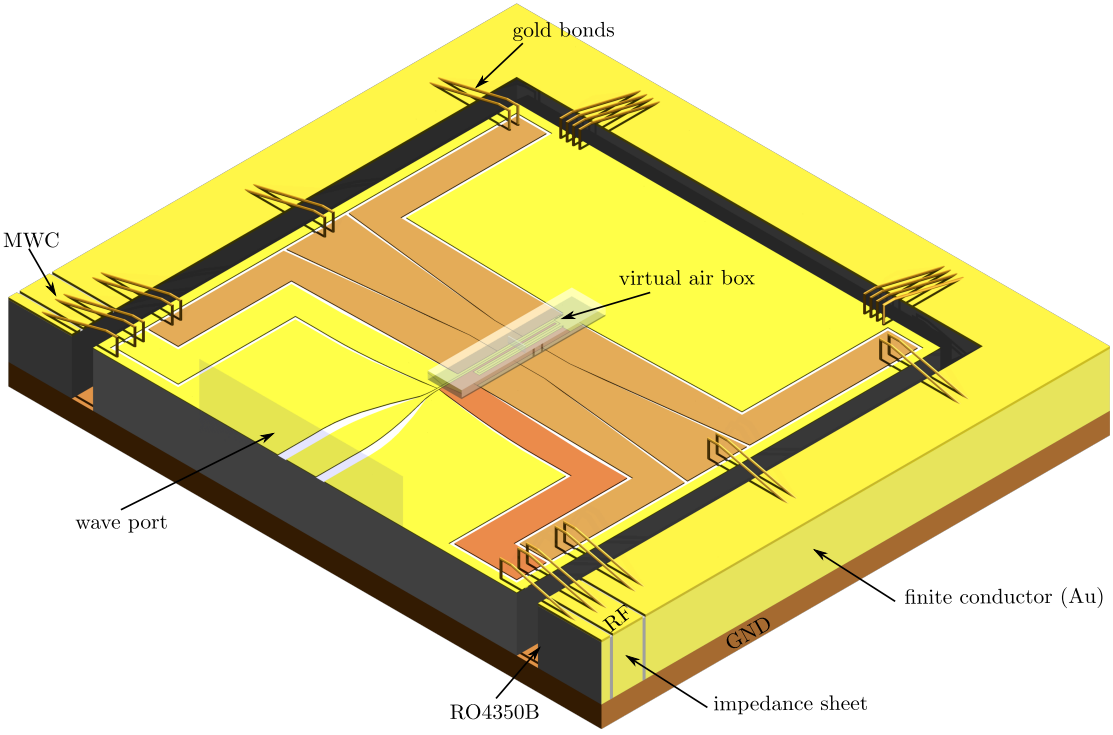

Figure 4.15: Simulation model with boundary conditions for all electrodes. The meander electrode is excited with a wave port and terminated on the chip. The ground plane and the dc electrodes are grounded using wire bonds connecting the electrodes to gold patches sitting on a RO4350B substrate. The gold patches are set to ground (GND) by a sheet with a finite conductor boundary, here gold (Au) is assigned. The microwave carrier (MWC) and the rf electrodes (RF) are terminated with impedance sheets connecting the gold patches. The virtual air box decreases the mesh size in the center of the chip leading to an increased accuracy.

field minimum from the surface. Here, we abandon the symmetry by adjusting all parameters individually for finding a suitable overlap of the electric and magnetic quadrupole fields. The sweeps are performed using surface currents. The height of the electric field quadrupole null, and hence the ion position is estimated using Equation (2.15), which treats the rf electrodes as infinitely extended in the axial direction. The target for the calibration trap is a height of roughly $45\,\mu$m. All previous simulations showed that the width of the meander and distance between segments have the strongest influences on the near-field minimum height above the surface. To reach approximately the height of $45\,\mu$m, a width of $18\,\mu$m for w_{MW}, w_{RF_1} and w_{GND_1} is assumed as a starting point for the trapping potential calculations, a rough estimate from the second parametric sweep. In addition, these sweeps reveal that the position of the minimum in the z-direction is a few microns off from origin, which is defined as the center of the middle electrode of the meander.

Adjusting the parameters as discussed in section 2.2.2 using the Biot-Savart-like law indicates a good set of rf electrode parameters, namely $w_{\mathrm{RF}_1} = 17\,\mu$m and $w_{\mathrm{RF}_2} = 85\,\mu$m with an ion-to-surface distance of $45.7\,\mu$m. The position in the z-direction can be altered by adjusting w_{MW} and w_{GND_1} while keeping the same distance between RF_1 and RF_2. The position of the magnetic near-field minimum varies from $44\,\mu$m to $48\,\mu$m in the x-direction and $1\,\mu$m and $3\,\mu$m in the z-direction. This position can be slightly adjusted by changing w_{MWC}. This electrode size has no influence on the ion's position and can hence be used to reach a better overlap between the fields. For the final overlap, the position of the ion is determined by calculating the rf potential from the complete electrode geometry using the Biot-Savart-like law for electrostatics [84] described in section 2.2.1. Furthermore, we use volume currents for the magnetic field solution in the central trap area of the model and for the complete meander line. Iterating different parameter sets finally leads to the following parameters: $w_{\mathrm{MW}} = 16\,\mu$m, $w_{\mathrm{MWC}} = 20\,\mu$m, $w_{\mathrm{RF}_1} = 17\,\mu$m, $w_{\mathrm{RF}_2} = 85\,\mu$m, $w_{\mathrm{GND}_1} = 25\,\mu$m and $w_{\mathrm{gap}} = 5\,\mu$m. The electric field minimum is located at $(x_{\mathrm{rf}}, z_{\mathrm{rf}}) = (45.7\,\mu\mathrm{m}, 2.9\,\mu\mathrm{m})$ while the magnetic field minimum is at $(x_{\mathrm{MW}}, z_{\mathrm{MW}}) = (45.4\,\mu\mathrm{m}, 2.1\,\mu\mathrm{m})$. The small discrepancy is irrelevant for measuring the near-field and calibrating the simulation boundaries. After fabricating this trap, a measurement of the S-parameter provides a first comparison with the simulation, as described in the next section.

4.2.4 S-parameter measurement

The scattering matrix is a useful tool to characterize microwave components. It describes the relationship between incident microwave V_j^+ and reflected wave V_i^- for N-port devices. The S-parameters S_{ij} are determined by

$$S_{ij} = \left.\frac{V_i^-}{V_j^+}\right|_{V_k=0 \text{ for } k\neq j}. \tag{4.2}$$

Although the SpyderTrap possesses two microwave electrodes, it is here considered as a single port device. The S-parameter S_{11} describes the back-reflection of an incoming signal. We measure this parameter using a network analyzer with an attached wafer prober.[2] The measured frequencies range from 1 to 10 GHz. The wafer prober is directly positioned at the beginning of the meander feed line. To eliminate any influence due to the large ground plane of the probe station, the trap is placed on an absorber made of Eccosorb MF-117. Several ion chips are investigated, all of them produced on the same wafer as the SpyderTrap used in the experiment. The simulation used for comparison is performed for the chip without any additional ground planes or connector board parts. Solely the pure chip including electrode

[2]The measurements are performed in cooperation with K. Schubert at the Technical University of Braunschweig.

and substrate is analyzed. A frequency sweep is performed for the same range as the measurement, to obtain the S-parameter. If no field solution is needed, the computing time can be decreased. Figure 4.16 shows the simulated and measured S-parameter S_{11} as a function of frequency. Here, we look at the real and imaginary parts of the S-parameter S_{11} separately. The plot shows only a small deviation from simulation to measurement for low frequencies, whereas differences start to appear for frequencies higher than 5 GHz. For higher frequencies, the wavelength of the microwave in the structure reaches the size of the structure. Close to resonance, the behavior is altered strongly depending on small geometric or material changes. The measured resonance is at $\approx 8.3\,\mathrm{GHz}$, while the simulated one is shifted to $\approx 9\,\mathrm{GHz}$. However, our interest is the variation in the frequency range around the qubit transition frequency of 1082.55 MHz. Here, the changes are rather small, see Figure 4.16 b). The impedance measured for that frequency is $Z_{\mathrm{meas}} = 3.4 + i35.3\,\Omega$ while the simulation reveals an impedance of $Z_{\mathrm{sim}} = 2.15 + i31.6\,\Omega$. Note that the corresponding inductance at about 1 GHz for both, measured and simulated, impedance value is approximately 5 nH, which can be compared to the inductance of a few wirebonds with a length of about one millimeter. Hence, these impedance values are approximately zero. The disagreement of these values can be explained by fabrication errors, slightly differing material properties as well as the position of the wafer prober on the chip. In summary, it can be stated that the first comparison of simulation and measurement shows a good agreement for the field-independent qubit frequency.

4.2.5 Model corrections

After fabricating the SpyderTrap we found that the simulation model used as shown in Figure 4.15 has some significant shortcomings. We discovered the issue by accident while we were trying to simulate also the rf trapping field using HFSS by converting impedance sheets on the rf electrodes to ports for applying a signal. We did the same for the microwave carrier electrode and gained some new insights. Here, I report on the results of these investigations and estimate any changes due to fabrication errors, as well as the dependence on frequency.

First of all, the assumption that a gold patch connected via a $50\,\Omega$ impedance sheet to ground describes a $50\,\Omega$ feed line is a quite simple picture. For a rough estimate it might be sufficient, however for determining the actual position of the microwave near-field minimum, it is not. To achieve a $50\,\Omega$ feed line behavior, part of the actual feed line should be modeled. The connection of the rf electrodes does not change the position of the near-field minimum significantly, as long as the impedance is chosen to roughly approximate the experimental settings. In the experiment, the total length of the rf conductor until the ground connection is made is about 20 cm. For the microwave, this single conductor appears as an inductance. Assuming an inductance for that line as low as $1\,\mu\mathrm{H}$ already results in

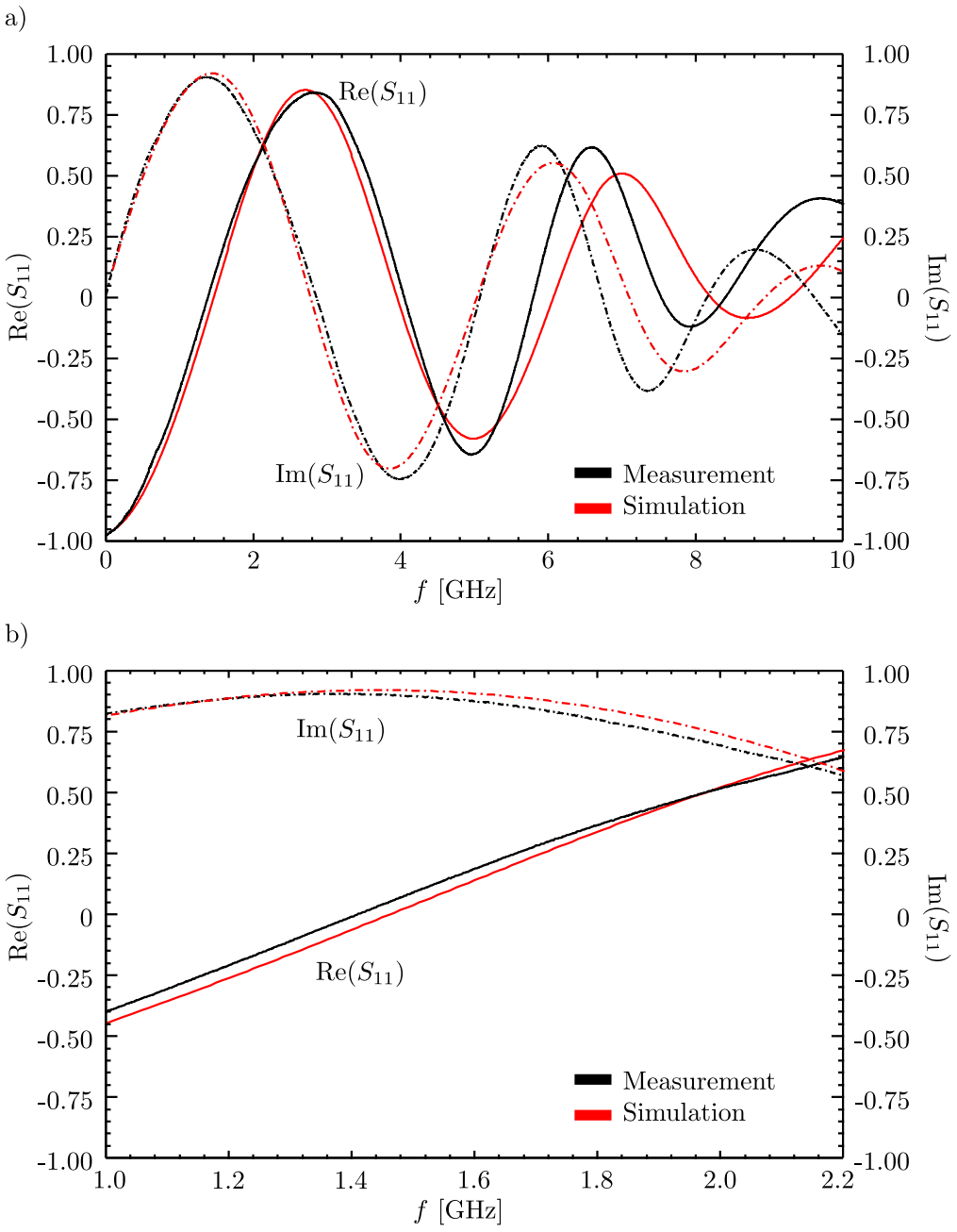

Figure 4.16: Real and imaginary part of the back-reflected signal S_{11}. The measured and simulated S-parameter are plotted as a function of frequency in a range from $1 - 10\,\mathrm{GHz}$ (a)). The zoom-in to the range of $1 - 2.2\,\mathrm{GHz}$ reveals only a small deviation between both signals (b)).

a reactance of $X_{\mathrm{RF}} = 1000\,\Omega$ at 1 GHz. Hence, the previously assumed impedance of $Z_{\mathrm{RF}} = 0 + 50i\,\Omega$ is obviously too low. Furthermore, the cable and connectors have some impedance, so $R_{\mathrm{RF}} = 0\,\Omega$ as an assumed resistance does not reflect the experimental conditions. In the model, the meander line is directly excited with a wave port, as shown in Figure 4.15. Though this provides a reasonable result, it does not replicate the settings in the experiment. Here, the meander is contacted to a feed line on a connector board by bonding. This feed line has an impedance of 50Ω, which is slightly different from the meander input ($Z = 45\Omega$). This discrepancy and the bond wires lead to back-reflection at that position. This should also be taken into account for a suitable model.

Enhanced model

The enhanced model replicates the conditions in the actual chip in a more sophisticated way. Instead of using impedance sheets, lumped ports are introduced for the microwave carrier and rf electrode. Here, boundaries for the impedance of the source can be added. We choose an impedance of $Z_{\mathrm{RF}} = 100 + 1000i\,\Omega$ for the rf port and $Z_{\mathrm{MW}} = 50\,\Omega$ for the microwave. The feed lines for the meander electrode on the connector board are arranged as coplanar waveguides (CPW). Due to the ground plane below the connector board the behavior of the CPW differs slightly. A different model for coplanar waveguides with an additional ground plane estimates the characteristic impedance of those feed lines [99]. This model requires the height of the substrate and the dielectric constants, as well as the dimensions of the feed line to determine the characteristic impedance. The substrate is as mentioned RO4350B with a height of $1524\,\mu$m. The dielectric constant of this material is $\epsilon_r = 3.66$ at 1 GHz. To achieve a $50\,\Omega$ line we set the width of the feed line to $w_{\mathrm{CPWG}} = 1.3\,$mm and the gap size on the connector board to $w_{\mathrm{gapFB}} = 150\,\mu$m. For the rf electrode, the electrode width is set to $w_{\mathrm{RFFB}} = 1\,$mm. To improve the connection of the gold between the connector board and the copper ground plane, vias are inserted in the design, as shown in Figure 4.17. Furthermore, an offset between the ion trap chip and the connector board is introduced. To accurately determine the position of the near-field minimum, the inner part of the electrodes and complete meander line are solved inside the volume. With the enhanced model, the more realistic position of the magnetic near-field minimum is determined as $(x_{\mathrm{MW}}, z_{\mathrm{MW}}) = (45.1\,\mu\mathrm{m}, 0\,\mu\mathrm{m})$. In the following, sources of possible deviations from this value are identified.

Fabrication tolerance

Since our fabrication process involves fabrication errors, the resulting fields due to such errors are determined. For the rf pseudopotential, such an error does not play a role, since the model is based on the gapless plane approximation. A correction parameter w_{cor} is introduced, which is subtracted from the gap widths

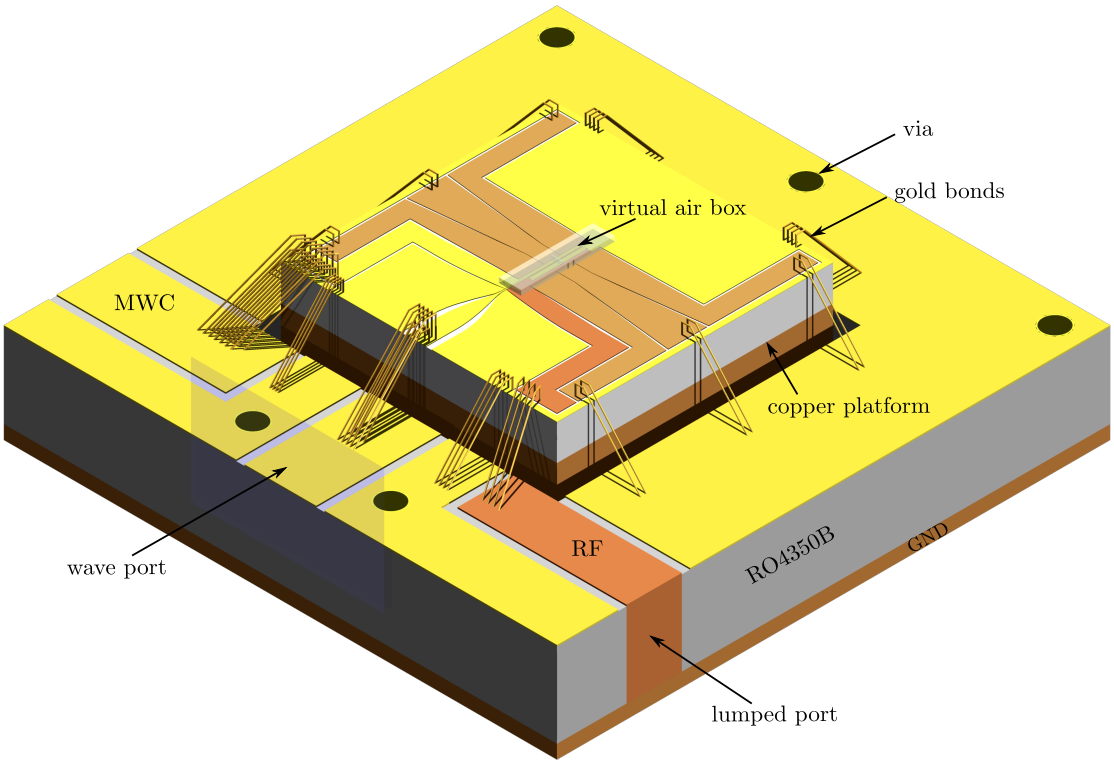

Figure 4.17: Enhanced model with part of the connector board, which exhibits 25 μm gold electrodes on a RO4350B substrate. The ion chip is placed on a copper platform to achieve an offset between connector board and chip, improving laser access. Gold wire bonds connect the chip and the connector board. To achieve a good connection of the ground plane of the connector board to the support copper block (GND), vias are inserted. The meander is fed via a feed line in coplanar waveguide configuration which is excited with a wave port. The microwave carrier electrode (MWC) and the rf electrode (RF) are excited with a lumped port. The virtual air box reduces the mesh size in the trapping center allowing for an improved accuracy.

and added to the electrode widths. For example, if the fabrication process leads to electrodes widths 1 μm wider than expected, the gap width is decreased by 1 μm. The corresponding correction parameter is $w_{\mathrm{cor}} = 1$ μm. The variation of the correction parameter goes from -1 to $2\,\mu$m, leading to a variation of the gap width from 4 to $7\,\mu$m. This is a realistic range for our mask and resist parameters. Moreover, the electrode thickness might deviate from the target value because of issues in the electroplating process. The electroplating is not homogeneous over the whole three-inch wafer and depends strongly on the plating time. Small deviations of $\pm$ 1 μm have been observed for the same electroplating time. A variation of the thickness by $\pm$ 2 μm is taken into account, assuming a worst case. Since the trap is not optimized for the performance of the sideband transition, only the overlap of the fields is of interest considering the deviations. As mentioned before, the trapping potential does not change, so only changes in position of the microwave near-field minimum are observed. For both errors, the position in the x-direction varies significantly while the position in the z-direction changes by less than $0.5\,\mu$m over the whole range. The influence of both errors on the field minimum height x_{MW} are shown in Figure 4.18. In the worst case, this leads to a mismatch by up to $\pm 3\,\mu$m for a perfectly overlapped design. In general, the error due to the fabrication process should be below $0.5\,\mu$m for the electrode widths and for the height, decreasing the mismatch to below $\pm 1\,\mu$m. Any larger deviation from this should be followed by an improvement of the fabrication process. However, a perfect match of the field quadrupoles in position cannot be achieved, even if the determined position were accurate to less than a few nanometers.

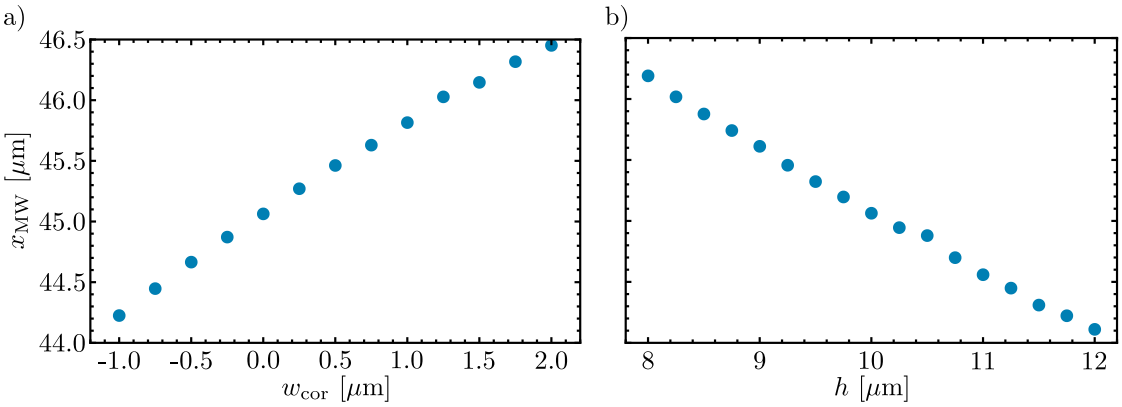

Figure 4.18: Dependence of the field minimum height x_{MW} on fabrication errors. An error due to the lithography process leading to a change of gap and electrode size, respectively, is introduced as w_{cor} (a). The second error occurs due to electroplating: the thickness of the electrodes h varies here in the worst case by $\pm 2\,\mu$m. Figure b) shows the influence. For both errors, the field minimum height changes x_{MW} by $\approx 1\,\mu$m per μm.

Frequency dependence

All simulations are performed for the qubit transition frequency at 1082.55 MHz. In the experiment, for sideband transitions, the microwave field will be detuned from this carrier resonance by $0 - 15$ MHz. In order to understand the influence of the drive frequency in general, a frequency sweep in a range from 850 MHz to 1800 MHz is carried out. This range includes all frequencies of the hyperfine manifold of $^9Be^+$, as well as the sideband transitions, which are usually on the order of ± 10 MHz detuned from the field-independent transition. The dependence in that range is rather small compared to the influence of fabrication errors. The position changes by less than 0.5 μm in height and 1 μm in the z-direction, as shown in Figure 4.19. For the sideband frequencies, there is a negligible difference in position, gradient and residual field. The solutions are obtained for surface currents to simplify the simulation model, explaining the height offset of about 0.4 μm for 1082.55 MHz. Apart from that, the parameter set is the same as before.

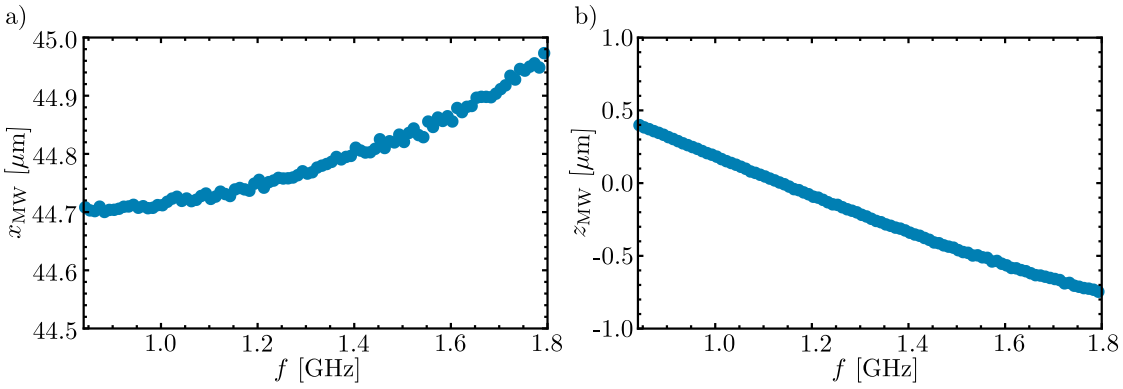

Figure 4.19: Position of the magnetic near-field minimum (x_{MW}, z_{MW}) as a function of frequency f. The changes in height x_{MW} (a) and z-coordinate z_{MW} (b) are less than a 1.5 μm for a change of 1 GHz and hence negligible for 10 MHz, the distance to a typical sideband frequency.

Deviation from assumed impedance settings

For the enhanced model, the impedance for the rf and the microwave carrier electrode was fixed to a certain value derived from the settings in the experiment. However, these values are assumptions and can be slightly different from our best estimate. Furthermore, transmission line theory implies a transformation of the termination impedance over the length of the transmission line for a mismatched termination [100]. Since the actual feed lines are much longer than modeled in the simulation setup, the simulated termination might not reflect the actual observed termination. In a first step, the simulations are performed with impedance sheets. Altering the impedance of both terminations individually reveals every change for

the model due to a mismatch in impedance. Sweeping the resistance and reactance of the rf feed line termination shows no significant change in the position of the near-field minimum, while both parameters of the microwave carrier feed line alter the position significantly. A look at the central trap area explains this behavior. The microwave carrier electrode is grounded, while the rf electrode is terminated with an open circuit. S-parameter calculations show that about 12 % of the power coupled into the meander is transmitted to the microwave carrier electrode, whereas only 0.005 % is transmitted to the rf electrode. This reduces significantly the influence of a back-reflected current from an impedance mismatch in the rf feed line. The influence of a varying termination on the microwave carrier electrode is shown in Figure 4.20. Altering the resistance or reactance changes the position by up to 12 μm in the z-direction and 5 μm in the x-direction. Normally, the feed line impedance should differ only little from a 50 Ω line. Microwave components in the line will, however, always exhibit some mismatches, leading to a back-reflection at the position of the mismatch. Estimating the impedance jump which leads to a back-reflected current similar to the experimental value is rather difficult.

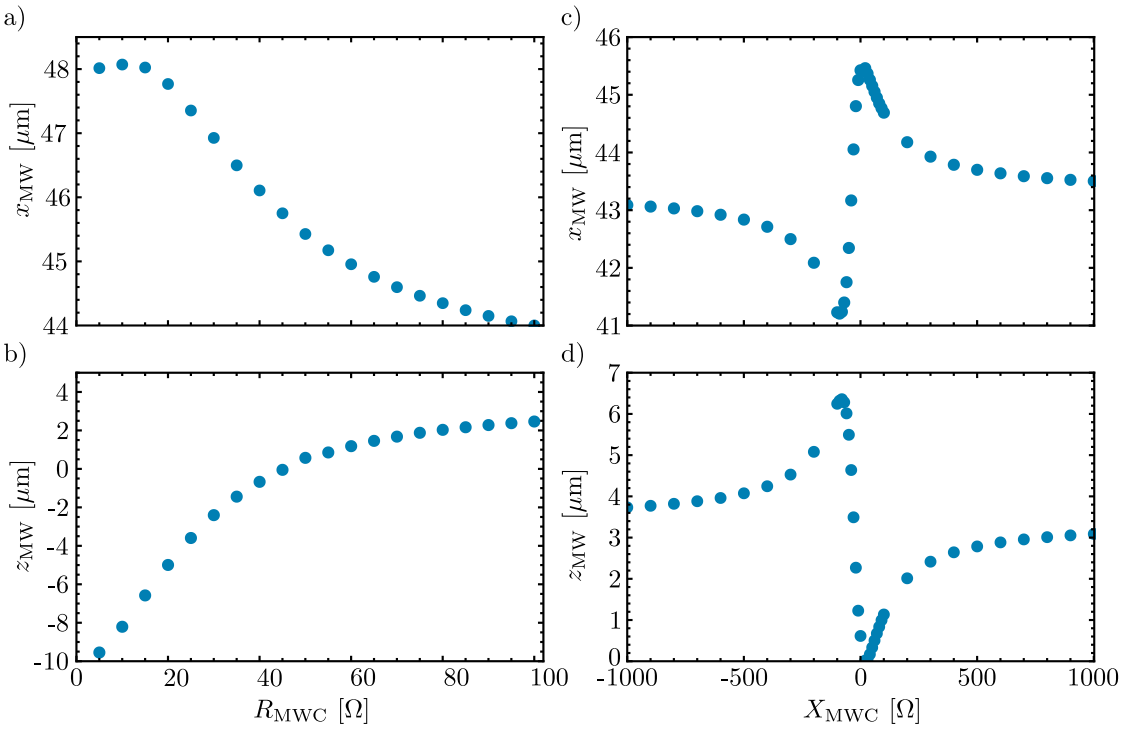

Figure 4.20: Position of the magnetic near-field minimum $(x_{\mathrm{MW}}, z_{\mathrm{MW}})$ as a function of resistance R_{MWC} and reactance X_{MWC} with which the microwave carrier electrode is terminated. Small deviations from the assumed impedance $Z_{\mathrm{MW}} = 50\,\Omega$ result in a significant change in position.

A more intuitive picture is given by approximating the back-reflected current by applying a small signal to each of the lumped ports. In an auxiliary simulation the lumped ports are included and the amplitude and phase of the applied signal are varied. The carrier electrode has a huge impact on the near-field configuration. Small deviations of the back-reflected current on the microwave carrier electrode lead to a significant change, not only in position but, also of the figure of merit. Figure 4.21 shows the position dependence on amplitude and phase of a back-reflected signal. Applying a current with a factor of ten higher in power to the rf electrode shows a similar behavior with a significantly lower oscillation amplitude. The oscillation is below 0.5 μm and hence negligible for our purposes. Since the back-reflected signal in the experiment can only be estimated, an exact prediction of the near-field minimum position for this trap is difficult. Here, the error depends strongly on the phase of the back-reflection. To reduce the influence of the microwave carrier electrode, that electrode should be moved further away from the trap center or removed completely.

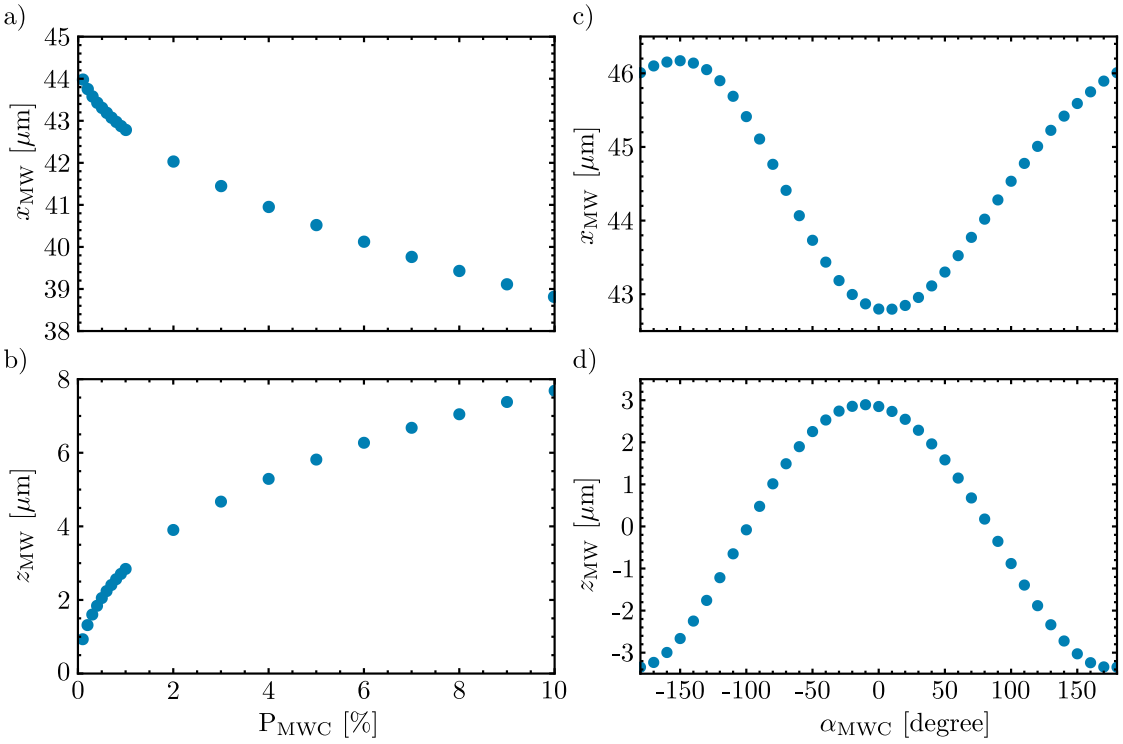

Figure 4.21: Position of the magnetic near-field minimum (x_{MW}, z_{MW}) as a function of amplitude P_{MWC} and phase α_{MWC} of a back-reflected current occurring from the microwave carrier electrode termination. While extracting the dependence on the amplitude, the phase is fixed to zero, whereas the data for the phase dependence is obtained for 1% of the input power. To model the back-reflection, a lumped port is used to apply an additional signal.

From the numerical data, the possibilities to adjust and optimize the near-field by applying a signal to the microwave electrode arises. However, this would resemble a return to the scenario of [51], where the near-field configuration was obtained by balancing three different currents. Although the currents needed are significantly smaller and thus the possible error, we propose another approach to adjust the near-field. In this approach we add a switch into the feed line of the microwave carrier in order to fine-tune the back-reflected signal. Either the switch lets the signal through or switches to a fixed termination with a specific impedance, ideally set by a double-stub tuner. This microwave component adjusts the phase and amplitude of a back-reflected signal using a transformation over the transmission line. However, for a next design, the carrier electrode should be eliminated or placed further away from the meander. In multi-zone trap arrays, the zones for single and multi-qubit operations should be separated to enable high-fidelity single-qubit addressing as discussed in [53].

Chapter 5

Apparatus

Performing experiments with trapped ions requires a complex experimental apparatus. The key element of the apparatus is the ion trap itself, a surface-electrode chip with different electrodes to provide confining potentials as well as microwave electrodes to control the quantum states of trapped ions. Even though we perform most operations using microwave near-fields, laser systems are still required to perform laser cooling and fluorescence detection of the ions. Furthermore, we operate a pulsed laser and a photoionization laser system for ablation loading of ions. The ion trap is mounted in a vacuum chamber providing an ultra high vacuum environment. The whole experiment is controlled with an FPGA-based control system enabling complex experimental sequences. Here, all components required to trap and manipulate beryllium ions are described, starting with the ion trap and its fabrication.

5.1 SpyderTrap

The ion trap tested here is a surface-electrode ion trap with integrated microwave quantum control. The so-called SpyderTrap is an ion trap with a surface-ion distance of 45 μm which is used to calibrate numerical simulations of microwave fields for controlling the quantum states of the trapped ions (cf. section 4.2). The focus of this work is to measure the magnetic field provided by a single meander electrode for driving sideband transitions. This measurement enables a comparison to the simulation model and potentially a calibration of the model (cf. chapter 6). The ion trap is produced in a clean room environment using standard microfabrication processes. We characterize the trap using surface analysis techniques such as optical microscopy or scanning electron microscopy (SEM) to estimate errors in the design parameters due to fabrication processes, important for validating the simulation (see chapter 4).

5.1.1 Fabrication process

The process to fabricate the SpyderTrap is based on planar chip technology, well established in atom and ion chip fabrication [101]. Here, the chip structure is produced by electroplating gold onto a substrate with a lithographically patterned resist. The whole fabrication process is performed in a clean room environment to guarantee a clean and defect-free surface, essential for avoiding stray fields and undesired field fluctuations in the trapping potential. In the following the substrate choice as well as an overview of the fabrication process are discussed. A detailed recipe can be found in appendix B.

Substrate

Building a microfabricated ion trap with integrated current carrying conductors demands a thoughtful choice of the substrate material. Using a substrate with a high thermal conductivity reduces thermal heating of the wires at the applied high currents. Furthermore, a low power dissipation factor is desirable to minimize high frequency losses. Table 5.1 lists commonly used substrate materials with relevant properties for microfabricated ion traps.

Table 5.1: Substrate materials used or suggested for microfabricated ion and atom chips at room temperature. Relevant properties such as the thermal conductivity, dissipation factor or dielectric constant are listed with approximate values for rf frequencies [26].

Material	Thermal conductivity (W/(Km))	Dielectric constant	Dissipation factor ($\tan\delta$)
AlN	180	8.5	3×10^{-4}
Alumina	30	9.8	1×10^{-4}
BN	28	4.1	5×10^{-4}
Diamond	2000	5.7	6×10^{-4}
Fused Silica	1	3.9	4×10^{-4}
GaAs	55	13	1×10^{-3}
Quartz	7	4.5	2×10^{-4}
Sapphire	45	11	1×10^{-4}
Si	150	12	5×10^{-3}
SiC	250	14	2×10^{-1}

We use polycrystalline Aluminium nitride (AlN) with a thermal conductivity of 180 W/(Km) and a power dissipation factor of 3×10^{-4} at rf frequencies. Considering a high thermal conductivity only diamond and silicon carbide (SiC) are better material choices. However, diamond is more expensive (about ten times) and SiC

has a high dissipation factor and hence high losses for the radiofrequency and microwave signals. Since the microfabrication equipment at the PTB clean room facility supports only 3 inch wafers, our AlN wafers have that size and a thickness of $635\,\mu\text{m} \pm 25\,\mu\text{m}$. The disadvantages of AlN is its relatively high surface roughness of about 50 nm. However, a careful control of the deposition rate during electroplating minimizes the effect of the initial high roughness. An alternative is crystalline AlN, which can nowadays be grown with a wafer size of up to 2 inches [102].

Fabrication flow

Electroplating is a chemical process in which metal is deposited onto a conductive surface using electrolysis. The conductive surface is placed parallel to an anode into a solution containing ionized metal atoms. Applying a negative voltage on the conductive surface and a positive voltage on the anode side leads to a current flow in the solution. The metal ions are deposited on the conductive surface. The whole fabrication process is illustrated in Figure 5.1 including conditioning treatments for the electroplating.

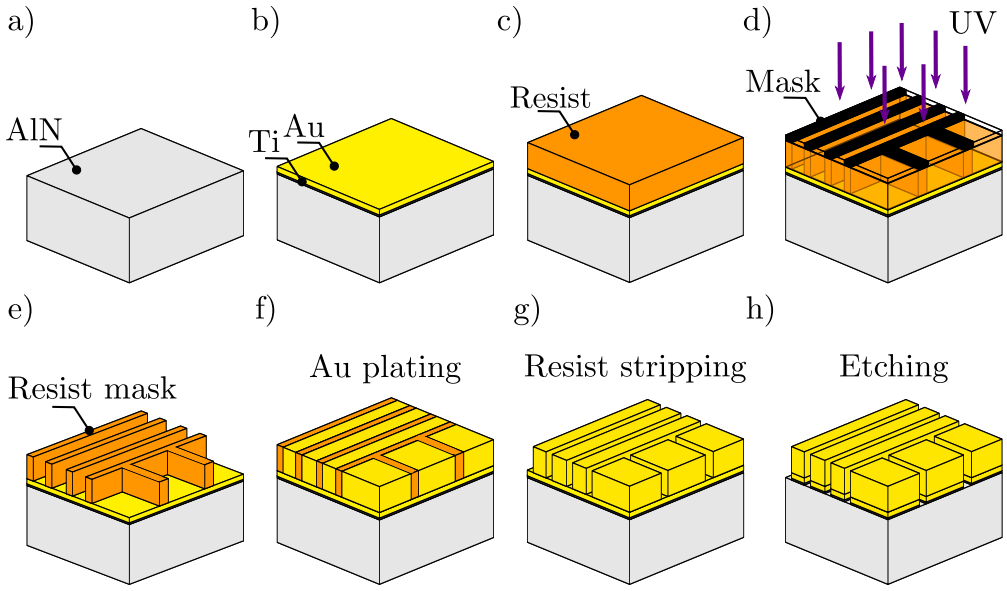

Figure 5.1: Fabrication process: a) Starting with cleaning the plain AlN wafer, a titanium adhesion (2 nm) and a gold seed layer (50 nm) are deposited by thermal evaporation (b). c) Spinning on $10\,\mu\text{m}$ resist with a following UV lithography step (d). After developing, a resist mask remains (e), in which the gold is electroplated (f). The resist mask is removed with acetone and piranha etch (g) and finally the seed gold layer and titanium layer are etched (h).

An electroplating process requires either a metal substrate or a conductive layer on the substrate to start the growth process. Hence, a metallic seed layer

is deposited on the wafer to initiate the process on the non-conductive AlN. A 50 nm gold layer is deposited on top of a 2 nm adhesion layer of titanium on the substrate by thermal evaporation. Optical lithography is used to transfer the chip structure from a chrome mask into a photoresist. After developing the exposed resist, the remaining structure is used as a template for electroplating. To achieve electrodes with a thickness of 10 μm, we use a positive tone resist[1]. Adjusting the spin coating time enables a resist thickness of about 10 μm. An additional step at higher angular frequency reduces the resist edge bead[2]. A remaining edge bead leads to near-field diffraction and, in a positive resist, to smaller features in the resist compared to the mask. The resulting error is about 2 μm and has to be taken into account when producing the chrome mask[3] for the lithography. The processed wafer serves as the cathode during electroplating. In our home-made setup, the wafer is attached with two contact pads to a movable mount which is connected to a small linear engine. This arrangement is placed parallel to a titanium anode and into the electroplating solution[4]. The electroplating beaker takes 0.5 l of the solution which contains 7.5 g of gold. Connecting the anode and the wafer to a power supply and slowly adjusting the voltage starts the process. From Faraday's law the time t to electroplate a specific thickness h of gold can be estimated by [101]

$$t = \frac{nFS\rho}{\alpha IM}h = \frac{10^{10}}{1.1}\frac{\mathrm{As}}{\mathrm{m}^3} \times \frac{S}{I}h. \tag{5.1}$$

Here, $n = 1$ is the charge number of the gold ions, F Faraday's constant, M the molar mass and ρ the mass density of gold. α is the current efficiency and is nearly 1 for the gold plating, while I is the current applied. S is the area which will be plated, including connector pads. The grain size of the plated gold depends on the electroplating rate. We choose a rate of 2 nm/s to achieve a smooth surface. After electroplating, the wafer is removed and rinsed carefully with DI water. Acetone removes the resist almost completely. To avoid any organic remains, the wafer is immersed in piranha etch before wet etching. Aqua regia etches the seed layer and usually most of the adhesion layer. The rest of the titanium can be etched with a following piranha etch step. Removing the titanium can be challenging, if the layer is thicker than 3 nm. In that case a strong acid - hydrofluoric acid (HF) - is needed.

One wafer contains about one hundred traps; each is optically inspected before sawing the wafer into pieces. Besides an optical microscope and a scanning electron microscope, a profilometer is available for thickness measurement. The characterization of the trap is described in the following section.

[1] ma-P 1275 from micro resist technology GmbH, Berlin

[2] During the spin coating process a bead is formed at the edge of the wafer. For thick film resists this bead can have a significantly higher film thickness.

[3] Our mask was made by Thomas Weimann at the clean room facility of PTB via electron beam lithography.

[4] Sulphite-based gold bath (Gold-SF) from METAKEM GmbH, Usingen, Germany

5.1.2 Characterization

An optical microscope is used to locate surface defects or potential shorts and to identify a suitable trap for operation. Furthermore, a rough measurement of the electrode widths is possible using this technique. However, it reveals no information about the thickness and the profile of the plated electrodes. This information is obtained using a profilometer and scanning electron microscopy (SEM). Unfortunately, these procedures can damage or contaminate the trap surface if not done properly. To avoid any damage or contamination during characterization we only inspect the ion chips nearby the optically selected one to extract relevant information.

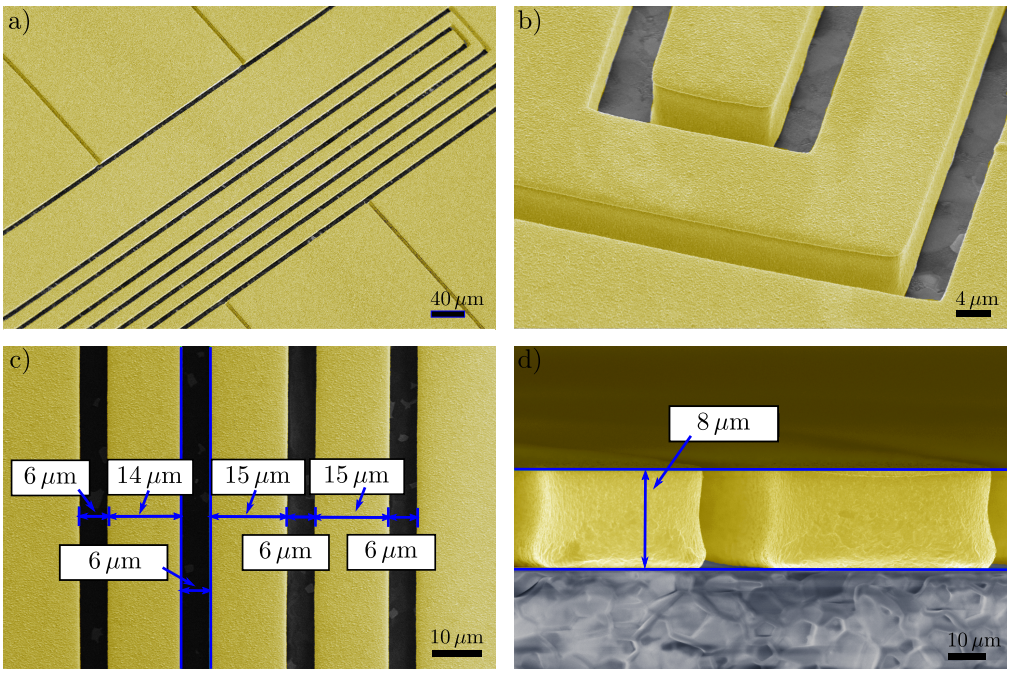

Figure 5.2: Scanning electron microscopy (SEM) images artificially coloured for clarification. The measurement was performed by Peter Hinze at the PTB clean room facility. In a) the trap structure is visible while b) shows the meander edge. Here, a mushroom-like shape of the electrode exhibiting overgrowth is identified. The sizes of individual electrodes are labeled in image c). Measured width of the electrodes in the central trap area of one of the ion chips nearby the optically selected one. d) Tilting of the sample during SEM inspection allows us to measure the electrode thickness. The thickness is measured on a SEM test chip which exhibits only parallel lines to allow for thickness measurements. The SEM measurement was performed on a SEM test chip taken from a different wafer compared to the ion chip characterized in a)-c).

The profilometer is a DEKTAK profiler with a 12 µm tip. In our case, it can only be used for thickness measurement, as the electrode and gap sizes are of similar size. Thickness measurements of gold structures with equal electroplating duration yield

a thickness deviation of about 2 μm between different wafers. Further investigations show an additional thickness variation on the wafer itself. That variation is on the same order and might arise from an uneven distribution of the gold in the solution, an uneven movement during the plating process or from an uneven current distribution. Additional stirring and quartering of the wafer before the electroplating might reduce this issue. The unreliability of the electroplating process has to be taken into account in designing the SpyderTrap. The thickness of the SpyderTrap chip used in the experiment is approximately 11 μm. Since the resist thickness is only 10 μm, this implies that the electrodes slightly overgrow the resist. This leads to a mushroom-like shape. We observe this effect with the profilometer and a SEM measurement as seen in Figure 5.2 b). Scanning electron microscopy not only reveals the profile of the electrode structure, but a measurement of the width is also possible and we can investigate the surface of the gold. Comparing the surface before and after etching shows that during the etching process, the gold electrodes are also affected. The etching leads to a slightly rougher surface and should therefore be done only for the required time. Figure 5.2 c) shows a SEM measurement with the widths of the center electrodes of one of the traps. We expect the parameters of the selected SpyderTrap to be similar. Comparing all nearby electrodes leads to the estimated parameters in Table 5.2. In our case, we choose a trap which has a slightly overgrown structure to reduce effects of charged particles on the dielectric. The specific shape partially blocks the undesired stray field. Figure 5.2 d) shows one of the measured profiles with an electrode thickness of 8 μm. Sharp edges were expected; the measurement shows a different behaviour. The current distribution in this shape might be slightly different compared to a square shaped electrode. This might lead to a slightly changed magnetic field distribution.

Table 5.2: Approximated parameters of the fabricated ion trap determined using optical microscopy and scanning electron microscopy. The thickness measurement reveals an electrode thickness of approximately 11 μm. The parameter indications can be found in Figure 4.12

Electrode	Width (μm)
gap	5
GND_1	24
MW	15
MWC	19
RF_1	16
RF_2	84

5.1.3 Trap assembly

Figure 5.3 illustrates the trap assembly with all necessary components. The ion trap is mounted onto a copper support to reach the necessary height for optical access in the vacuum chamber. The connection from the electrodes on the SpyderTrap to the signal sources is done by wirebonding the electrodes onto a connector board[5]. This board is made out of RO4350B and provides the rf, dc and microwave connections. The microwave line is a $50\,\Omega$ line tapered from an SMA connector to a suitable size for connecting the trap. The connector board is called filterboard, which alludes to one of its functions. The dc connection lines include rf filters to suppress any rf noise on the dc electrodes. Together with an additional filterbox outside of the chamber, the rf filter forms a Butterworth filter [103]. The rf is connected via a pin to an rf feedthrough while the microwave signal paths are connected via SMA cable. These cables have an impedance of $50\,\Omega$ to reduce any impedance mismatches. Both filterboard and trap are mounted on a copper block to supply a sufficient heat sink which serves also as a ground plane. The SpyderTrap is glued onto the copper mount with an epoxy[6], while the filterboard is screwed onto the mount with gold plated screws. The gold plated screws provide a good electrical connection between the board and the copper ground. After glueing and mounting both items, the electrodes are bonded using a ball wire bonder with $25\,\mu$m gold bonds. Depending on the current flowing through the electrodes, different numbers of bonds were used. The dc electrodes are connected with two bonds while the microwave electrodes are connected with at least ten bonds. These multiple bonds will support a current of at least 1 A, while four bonds are sufficient for the rf where relatively small currents are observed.

A Faraday cage is added onto the filterboard surrounding the SpyderTrap. This cage is used to block any unwanted electrical fields. A gold mesh with an optical transmission of 90% completes the cage. Optical access is available on the main axes. The extension on the left side of the cage supports a 0.5 mm diameter beryllium wire, the neutral atom source. The loading scheme is described in chapter 5.3.1.

5.2 Vacuum system

Single and few trapped-ion experiments are usually realized in ultra-high vacuum (UHV) chambers with pressures of about 10^{-11} mbar or less. In such an environment, background gas collisions are reduced and the lifetime of the ions in surface traps can reach several hours. To reach UHV conditions, three vacuum pumps are connected to the main chamber with a distribution junction. Besides a turbomolecular

[5]Fabricated by Contag AG, Berlin, Germany
[6]EPO-TEK H74 from Epoxy Technology Inc., MA, USA

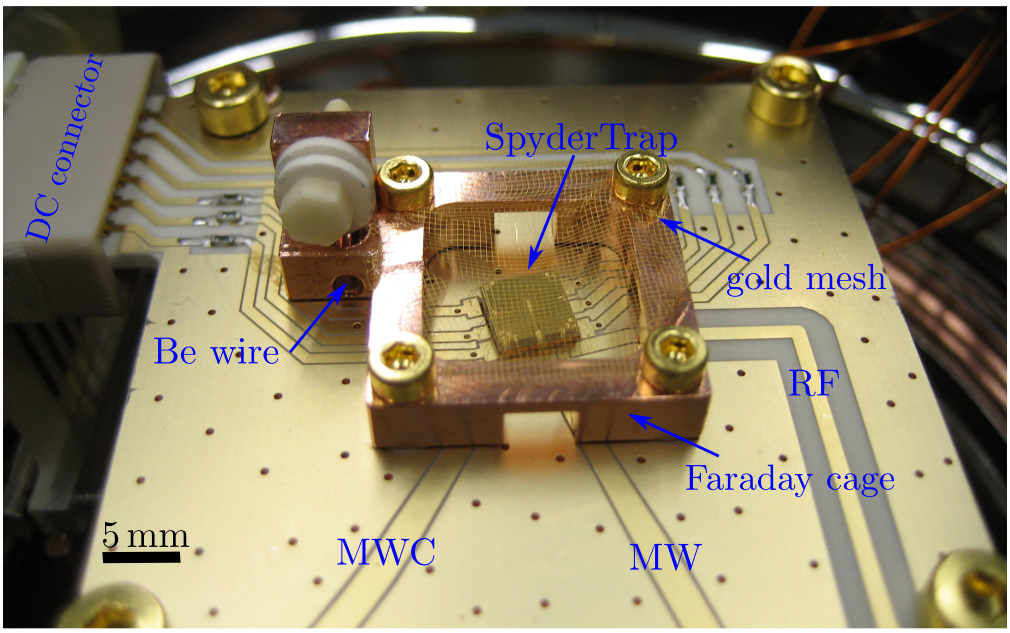

Figure 5.3: Trap assembly. A SpyderTrap mounted on a filterboard inside a Faraday cage which supports the beryllium wire as source of our ions.

pump[7], we use an ion getter pump[8] and a titanium sublimation pump[9]. The picture in Figure 5.4 shows the complete setup. The main chamber is a six-inch "spherical octagon"[10] which contains the trap on the chip mount described in 5.1.3. Besides the optical viewports, the vacuum chamber has three flanges with electrical feedthroughs: SMA connections for the microwaves, the 48 pin connector for dc and power feedthrough pins for the rf connection. We inserted four rf feedthroughs to enable a design with three adjustable radiofrequency electrodes. In the present setup three of the four feedthroughs are grounded, and only one is used to supply the rf voltage for the trap. In general, only UHV-compatible components are used, including vented screws to prevent virtual leaks.

Before assembling the vacuum chamber, all components were cleaned using an ultrasonic bath with first DI water, then acetone and finally isopropanol. The turbo molecular pump evacuates the chamber until a vacuum on the order of 10^{-8} mbar is reached. In a first step, the evacuated chamber is baked for three weeks at 300° C without delicate components such as the filterboard, electrical connectors or optical viewports. The final assembly in which the chip is mounted into the chamber is performed in a clean room environment to prevent dust and particles from getting onto the chip structure. Now, a second baking step is performed. The

[7]TPS Compact V304 from Agilent Technologies, Santa Clara, CA, US
[8]TiTan Ion Pump from Gamma Vacuum, Shakopee, MN, US
[9]VACOM Vakuum Komponenten & Messtechnik GmbH, Großlöbichau, Germany
[10]Kimball Physics Inc.,Wilton, NH, USA

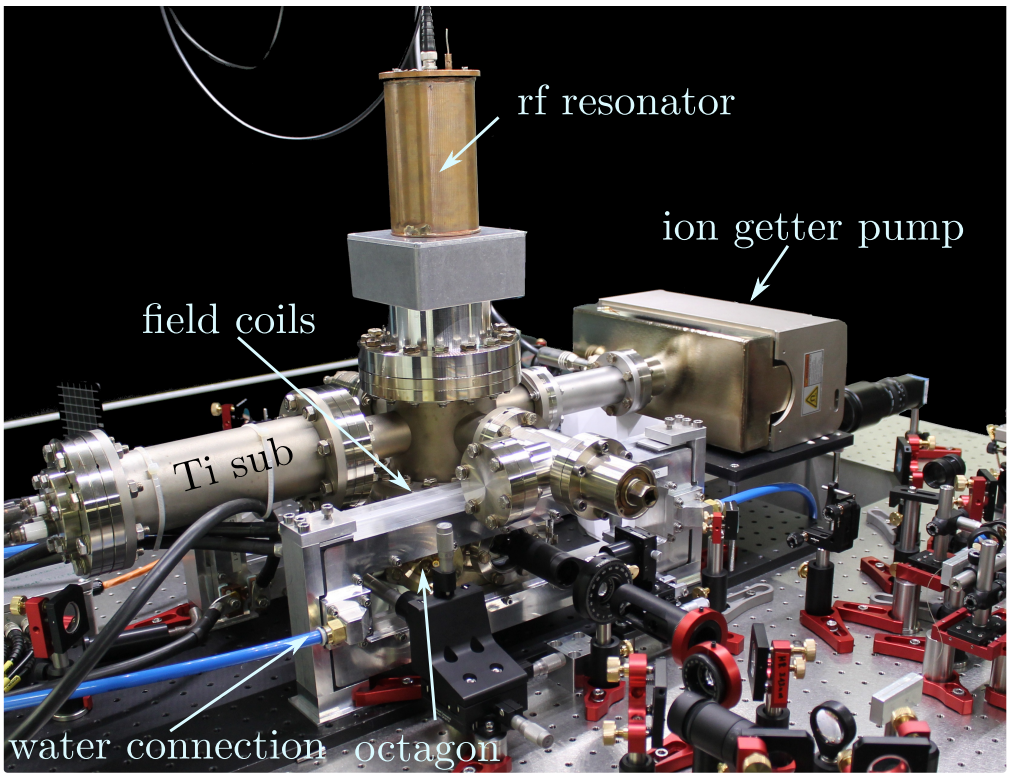

Figure 5.4: Picture of the complete vacuum chamber including rf resonator, magnetic field coils and vacuum pumps. The water connections for the field coils are visible while the octagon is hidden behind the coils.

temperature is limited to 180° C, the highest temperature the optical viewports can withstand. The baking time is two weeks. During the second baking step, the titanium sublimation pump is fired to prevent outgassing after the bake out. After cooling down the chamber to room temperature, the ion getter pump is turned on and the turbomolecular pump is disconnected. All wires of the sublimation pump are successively fired at 45 A for five minutes a couple of times until a vacuum level of 10^{-11} mbar is reached. Here, a thin titanium layer covers the walls of the chamber and acts as a getter pump. To maintain the pressure level, the layer has to be renewed every few months.

Magnetic field coils

Outside of the vacuum enclosure are the magnetic field coils used to define the quantization axis and to create the required field for the field-independent qubit (cf. chapter 3). To produce a magnetic field of 22.3 mT at the position of the ion, the coils should be as close as possible to the chamber to minimize the required current. Still, a power consumption of more than 5 kW has to be dissipated. We

use directly water-cooled magnetic field coils. The design is based on the work of [104]. Here, we use round insulated copper wires of about 2 mm diameter wound in four layers of 18 windings each on an aluminium mount. The water flows through the mount around the wires. For efficient cooling, PVC spacers are positioned between the different layers. To reach the desired field of 22.3 mT, a current of 88.6 A with a voltage of 65 V is necessary. The orientation of the magnetic field is sketched in Figure 5.5. The z-axis of the trap chip (cf. Fig. 4.12) is rotated by 12° counter-clockwise with respect to the magnetic field orientation.

5.3 Laser systems

The laser systems needed in a quantum control experiment highly depend on the level structure of the ion of choice. In the case of singly ionized beryllium we need two types of laser systems; one delivering near-resonant light around 313 nm for Doppler cooling, repumping and detection, and the other for photoionization (PI) of neutral beryllium. The setup presented here involves an ablation scheme for loading ions into the trap which requires an additional laser. Figure 5.5 illustrates the experimental beam path to the trap, including a schematic of the vacuum chamber. In the following the loading scheme, including the PI laser system, the Doppler cooling setup, and the imaging are described.

5.3.1 Loading

In general, the loading scheme for trapped ions consists of three basic steps:

- generating a neutral atom flux
- ionization either through electron impact or photoionization
- trapping and cooling the ionized atom

Starting with a neutral atom flux evaporated from the oven system, the atoms pass through the photoionization laser beam which ionizes some atoms. Oscillating and static electric fields trap the ionized atoms in all three dimensions. In the trap, the ions interact with the Doppler cooling laser which leads to a reduction of their kinetic energy. The scattered photons are detected via an imaging system.

The most common way to generate the neutral atom flux is a resistively heated oven. For example, by heating a beryllium wire[11] with an electric current, the neutral atoms evaporate and can be directed to the trap via suitable shielding. The shielding protects the trap surface from excess atom flux. Instead of using a resistively heated oven as a beryllium source, we implemented and tested an

[11] The beryllium wire is wrapped around a tungsten wire. The current runs through the tungsten wire and both wires are heated up.

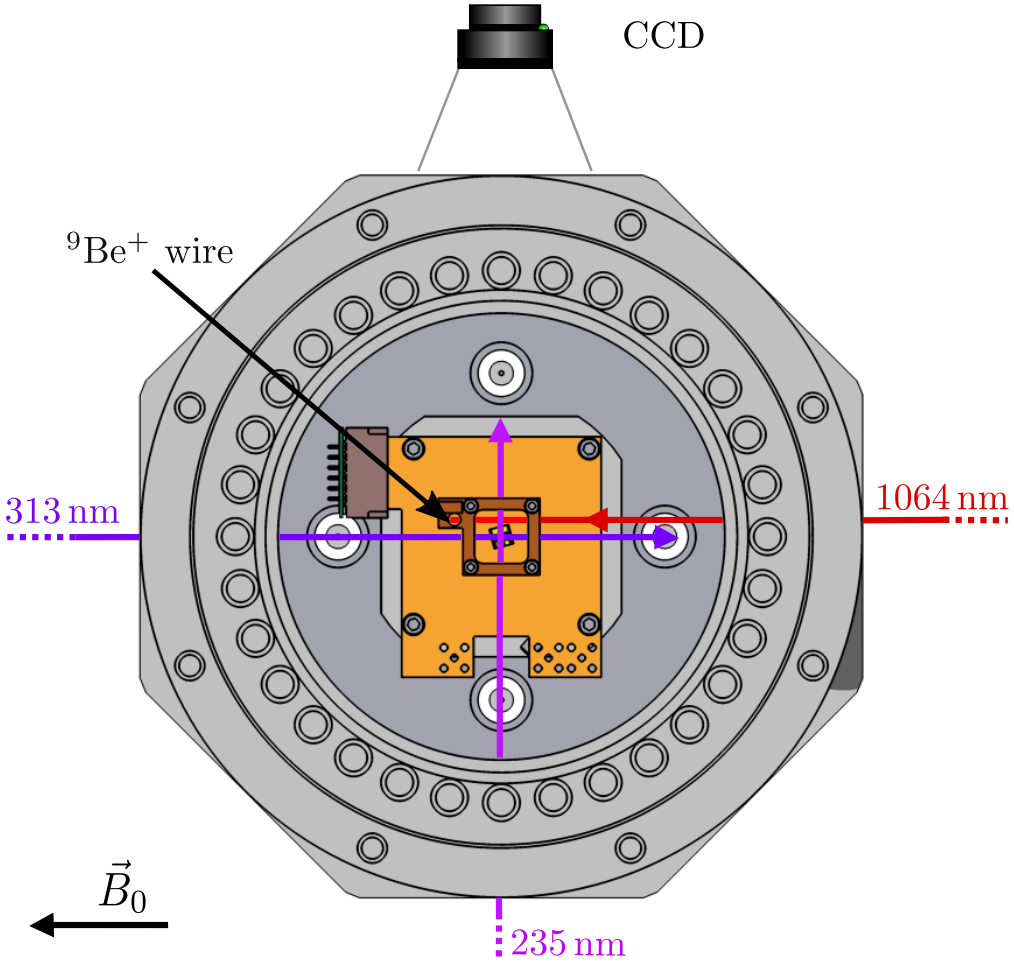

Figure 5.5: Beam paths for the 313 nm cooling and detection laser, the 235 nm photoionization laser and the 1064 nm beam for the ablation loading. The infrared beam on the beryllium wire can be observed with a CCD camera. The wire is placed in the extension of the Faraday cage.

ablation technique which produces a neutral atom flux. Similar schemes were shown for example in [105]. To start the ablation process, a 1064 nm nanosecond laser pulse[12] is focused onto a 0.5 mm diameter beryllium wire which is mounted next to the trap as shown in Figure 5.5. The beam is aligned onto the wire through a 2 mm hole in the Faraday cage. For ease of alignment, we perform the procedure with a 1051 auxiliary continuous wave (CW) laser beam first and then overlap the pulse laser with the auxiliary beam. An infrared CCD camera looking from the side images the spot of the lasers (pulsed and auxiliary) on the beryllium wire. We use the Minilite laser in single shot mode and adjust the power of the laser until a pressure change is detected on the display of the ion pump current. Typically the pressure rises up to about 5×10^{-11} mbar. At this level we can reliably trap with a few pulses within seconds. The atom beam is directed to the trap via an additional hole in the oven mount under an angle of 20 °. Above the trap center, the atom beam crosses the photoionization laser under an angle of 110 °. This configuration was chosen to minimize the Doppler-broadening as much as possible within the geometrical constraints.

The direct ionization of neutral beryllium would require a photon with a wavelength of 133 nm. Since this is in the deep UV we use a two-photon process to ionize the atoms. A first photon with an energy of 235 nm excites the neutral Be atom resonantly from the 2 $^1S_0$ to 2 $^1P_1$ level. A second photon then excites to the continuum and completes the photoionization process. The 235 nm light is provided by frequency quadrupling a commercial 940 nm diode laser/tapered amplifier system[13] with a maximum output power of 1.5 W, as described in [106]. To achieve a sufficient output power at 235 nm we set up the doubling cavities in bow-tie configurations. Both cavities are locked with the Pound-Drever-Hall method [107]. Figure 5.6 shows a simple schematic of the laser setup. An output power of about 15 mW is reached. We reduce this power to about 2 mW, an adequate power level for the ionization process. To avoid as much as possible buildup of patch charges on the ion trap due to the UV light, a computer controlled shutter is inserted into the beam path. The PI beam is only turned on during the loading procedure.

The frequency for the ionization can be determined by measuring the fluorescence from the 2 $^1S_0$ to 2 $^1P_1$ transition in neutral Be atoms. To avoid contamination of the trap with neutral beryllium, the fluorescence measurement has been done in a small vacuum cube. Since the atom flux due to laser pulses is rather small, a continuous wave source at 1550 nm heats the wire for at least ten seconds. A fraction of the 470 nm light is guided to a wavemeter to monitor the wavelength during the measurement. The detection of the fluorescence depending on the frequency around 638.0395 THz clearly shows the resonance, see Figure 5.7. Note, in the small vacuum chamber the atom beam and the photoionization laser are

[12] Minilite I from Continuum, San Jose, CA, USA
[13] TOPTICA Photonics AG, Gräfelfing, Germany

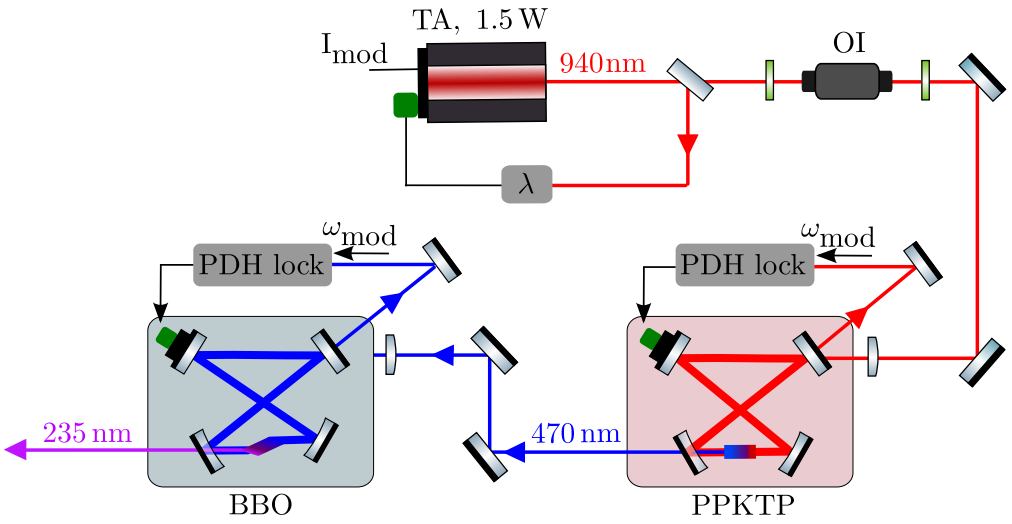

Figure 5.6: Illustration of the photoionization laser system. The 940 nm light of the Tapered Amplifier (TA) is led through an optical isolator (OI), to reduce any back reflection into the laser, to the first doubling cavity. The light is doubled in a PPKTP crystal and the length of the cavity is locked by a Pound-Drever-Hall lock (PDH). The generated 470 nm light is then doubled in a second bow-tie cavity in a BBO crystal. This cavity is again locked with a PDH lock using the modulated sidebands of the first SHG stage. The created 235 nm light is then focused into the chamber. To adjust the wavelength for the photoionization process, part of the 940 nm is measured with a wavemeter. We manually adjust the frequency to the beryllium resonance by tuning the slave laser's cavity length via a piezo (PZT). We use here a ComponentLibrary by Alexander Franzen which is licensed under a Creative Commons Attribution-NonCommercial 3.0 Unported License.

perpendicular to each other, which reduces the temperature-dependent Doppler shift.

However, in the experimental apparatus this is not the case. We have to take into account a slight change in the resonance frequency due to the Doppler effect. For the loading scheme this shift is small compared to the width of the resonance. We reliably load within a range of 1 GHz around the measured resonance. The ability to shoot only a single pulse onto the wire to achieve sufficient atom flux reduces the deposition of beryllium onto the chip surface compared to the common resistive oven technique, and it saves heating time. It also allows us to minimize the time that the photoionization laser is on and the resulting charge buildup.

5.3.2 Cooling and detection laser system

The simple level structure of beryllium ions requires only a single laser system at 313 nm for several purposes. By tuning this wavelength with acousto-optic modulators (AOM), cooling and detection as well as optical pumping can be

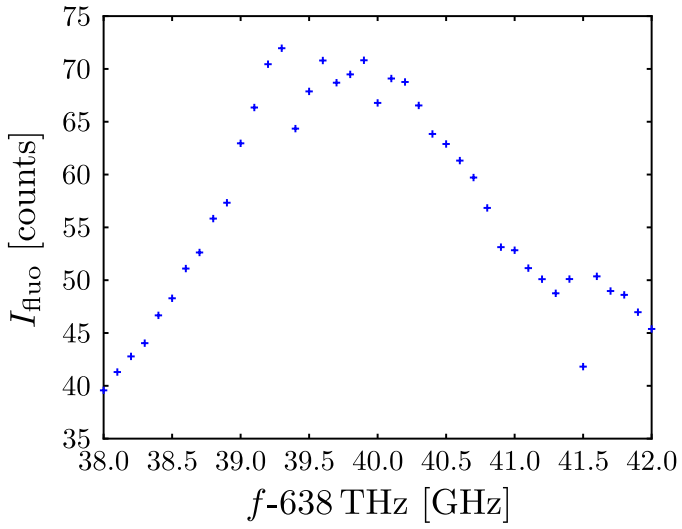

Figure 5.7: Beryllium fluorescence measured in a small test vacuum chamber as a function of the frequency of the photoionization laser. Since we lock and measure the 470 nm light instead of the 235 nm, the fluorescence is shown as a function of the corresponding frequency. We scan the laser frequency from 638.038 THz to 638.042 THz.

implemented. The complete laser system consists of three parts: generating 313 nm light, stabilizing the frequency of the 626 nm light to an iodine line and an AOM setup to produce the three different beams. The system is illustrated in Figure 5.8.

The generation of the 313 nm laser light is done according to the schemes presented in [108, 106]. Sum-frequency generation (SFG) with two near-infrared fiber lasers at 1550 nm and 1051 nm yields 626 nm light, followed by a frequency-doubling step to reach the desired wavelength of 313 nm. Each of these fiber lasers achieves an output power of 5 W. In our experiment we use only 2.2 W to obtain 0.5 W at 626 nm. For the SFG, both beams are focused into a PPLN (periodically poled lithium niobate) crystal, which is temperature stabilized to 180 °C to ensure phase matching. The polarization of the 1050 nm laser is adjusted with a half-wave plate before combining both beams with a dichroic mirror. The conversion efficiency depends on the polarization overlap and can be adjusted with the half wave plate. The optimal spot size for the SFG is achieved by focusing the beam into the crystal. With a rather large output beam only a single lens is required for the 1051 nm light, whereas two lenses are needed for the 1550 nm beam. After the SFG, a dichroic element separates the remaining infrared light from the visible 626 nm light and the infrared light is led onto a beam dump. To stabilize the frequency, we lock the 626 nm light to an iodine line via frequency-modulation spectroscopy. For this purpose, a combination of a half-wave plate and a PBS (polarizing beam splitter) picks off about 20 mW of the light, directing it to the stabilization setup. The light is shifted by 576 MHz using an AOM in double pass configuration, and an additional AOM shifts the pump light in the frequency-modulation spectroscopy

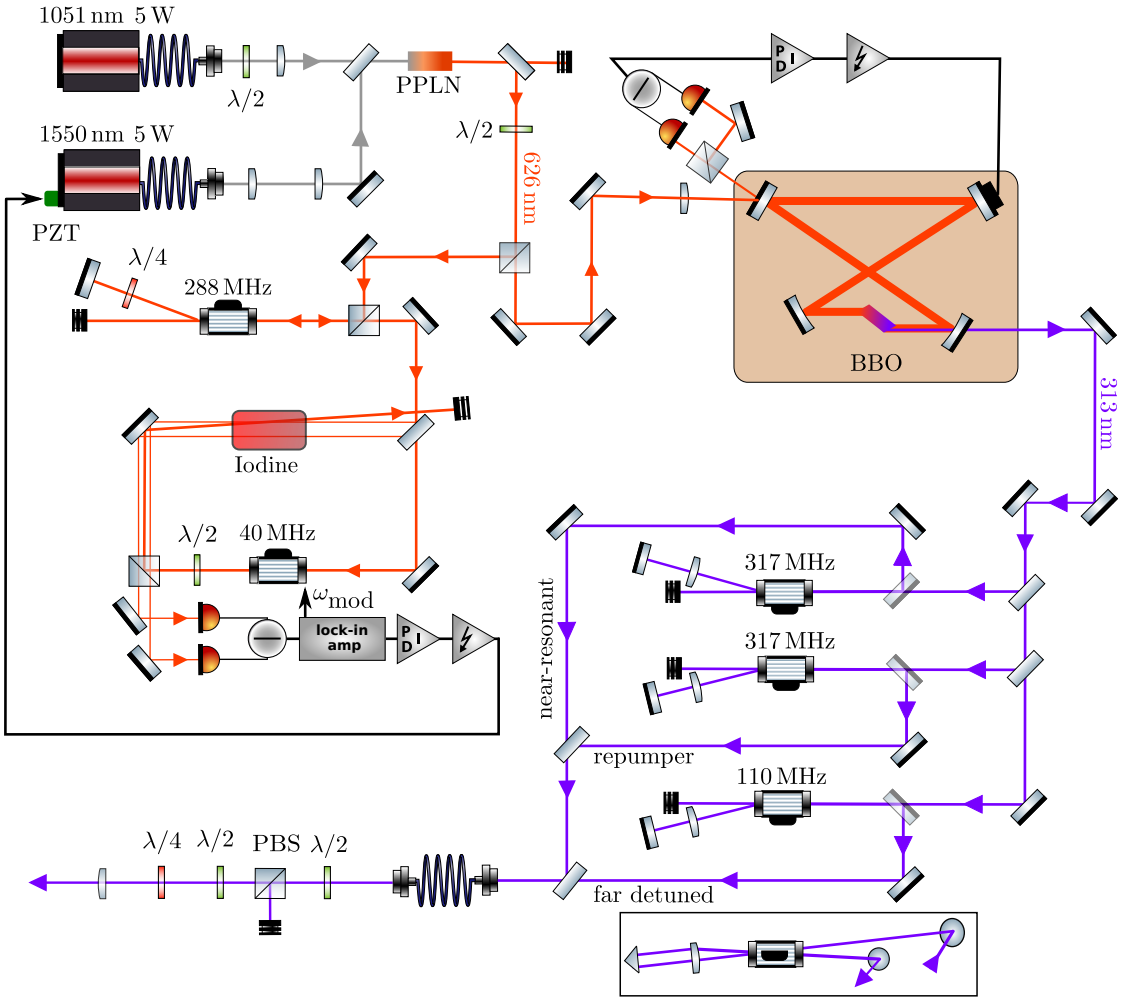

Figure 5.8: Illustration of the 313 nm laser system used to generate the cooling and detection as well as the optical pumping wavelengths. The illustration contains all three parts of the of the system. The generation of the 313 nm includes the SFG in a PPLN crystal and the SHG in a BBO crystal. This light is then divided into the three beams and shifted to the mentioned wavelengths with AOMs in double-pass configuration. A typical double-pass setup is visualized in the small black box which shows a side view of the setup. Furthermore, the frequency-modulation spectroscopy setup to lock the wavelength to one of the iodine lines is displayed. The box shows a side view of one AOM setup to visualize the beam path. We use here a ComponentLibrary by Alexander Franzen which is licensed under a Creative Commons Attribution-NonCommercial 3.0 Unported License.

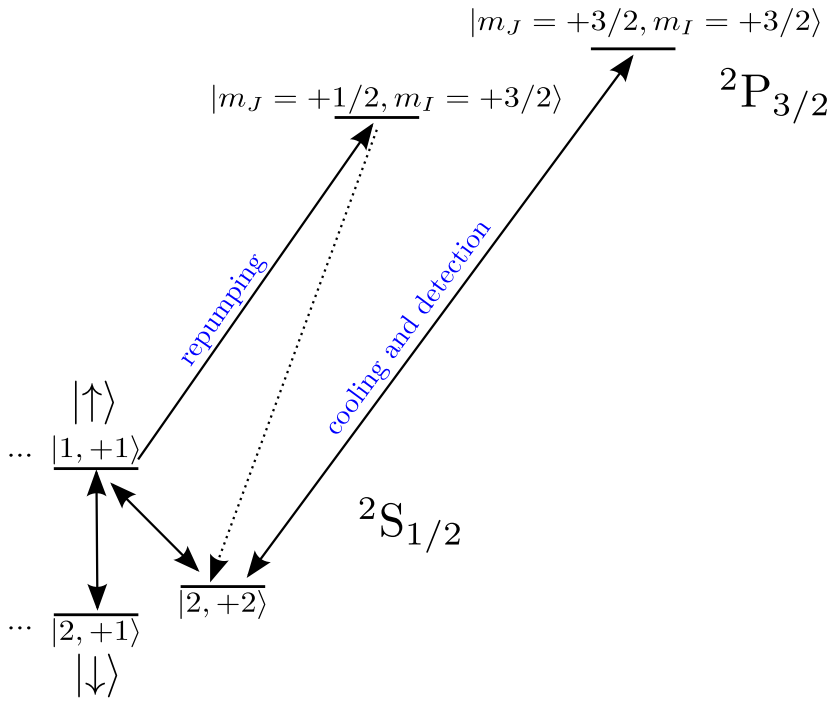

Figure 5.9: Overview of optical transitions between the $^2\mathrm{S}_{1/2}$ and the $^2\mathrm{P}_{3/2}$ manifold required for cooling, detection and repumping.

setup by an additional 40 MHz, effectively causing an additional shift of 20 MHz relative to the lock point, which is a line in the iodine spectrum. The doubled frequency of that iodine line is 1825 MHz red-detuned from the cycling transition, $^2\mathrm{S}_{1/2}$ $|F = 2, m_F = +2\rangle$ to $^2\mathrm{P}_{3/2}$ $|m_J = +3/2, m_I = +3/2\rangle$, which is used for cooling. The remaining light is frequency-doubled by a SHG process in a BBO crystal. To increase the conversion efficiency of the process, the BBO crystal is placed into an enhancement cavity in bow-tie configuration, which is resonant with the pump frequency. The locking of the length of the cavity to a multiple of the pump frequency is realized with the Hänsch-Couillaud method [109], where the feedback is sent to a piezoelectric transducer (PZT) mounted on one of the cavity mirrors. We typically operate at an output power of the enhancement cavity of about 100 mW at 313 nm, more than sufficient to supply all necessary beams. This light is now 1192 MHz blue-detuned from the doubled frequency of the iodine line and hence 633 MHz red-detuned from the cooling transition. To create all necessary frequencies for cooling, detection and optical pumping, the beam is separated into three parts: a near-resonant beam, a far-detuned Doppler beam and a repumper. Each beam is shifted using an AOM in double-pass configuration. The near-resonant beam is slightly detuned for state detection and Doppler cooling. We reach the resonance frequency by shifting the frequency-doubled beam with a 317 MHz AOM. For optimizing Doppler cooling, the frequency is red-detuned

by half of the excited state linewidth, which is 19.4 MHz. The far-detuned beam is 856 MHz red-detuned from the cycling transition, $^2S_{1/2}$ $|F = 2, m_F = +2\rangle$ to $^2P_{3/2}$ $|m_J = +3/2, m_I = +3/2\rangle$ using an AOM working at 110 MHz. This light is especially necessary during loading to efficiently Doppler cool hot ions. It is also used for repumping during the Doppler cooling. The dedicated repumper is red-detuned by 1268 MHz from the cooling transition and drives the $^2S_{1/2}$ $|\mathrm{F} = 1, \mathrm{m_F} = +1\rangle$ to $^2P_{3/2}$ $|m_J = +1/2, m_I = +3/2\rangle$ transition to deplete the $|\mathrm{F} = 1, \mathrm{m_F} = +1\rangle$ state (essential for sideband cooling). All transitions mentioned here are shown in Figure 5.9. With the experimental control unit (cf. section 5.4.1), it is possible to individually address all three beams and adjust the power of each beam. After recombining the beams, they are coupled into a UV fiber [110] (see also [111]) for mode cleaning and reduction of beam pointing effects. The beams are then aligned into the vacuum chamber. A PBS and a subsequent quarter- and half-wave plates set the polarization of the beams. The lens focuses the beams 45 μm above the ion trap surface in the trap center. Here, the beam width is about 30 μm. Aligning the beams parallel to the surface is important to avoid hitting the surface and hence creating stray light and possible patch potentials.

5.3.3 Imaging system

The state detection of the ion is performed by measuring the scattered photons from the ions. The state-dependent fluorescence is induced by the light of the near-resonant beam and is collected by our imaging system, a combination of a customized Sellmaier objective with a magnification of 13 and a numerical aperture of 0.41 and a commercially available microscope objective with a magnification of 3. The complete system is located outside of the vacuum enclosure and is illustrated in Figure 5.10. The light is either directed onto a photomultiplier module[14] (PMT) with a quantum efficiency of about 20% at a wavelength of 313 nm or onto an EMCCD camera[15]. We can switch between both detection methods with a flip mirror. For quantitative analysis, the scattered photons are collected with the PMT. Here, each detected photon produces a TTL signal counted by the experimental control unit. To obtain a low-background signal from a trapped ion, it is essential to suppress any stray light. Accordingly, an aperture is placed at the imaging plane of the first objective to reduce stray light from the chip surface. The external stray light is decreased by enclosing the whole detection beam path into a tube system and by mounting a UV transmitting filter in front of the PMT.

The Sellmaier objective is mounted onto a three-dimensional motorized stage to adjust the objective to the trap center and to change the focus position to accommodate 235 nm and 313 nm light for alignment. The camera can be used to align both beams. Using the image of the illuminated electrode structure, we can

[14] H8259-01 from Hamamatsu Photonics K.K, Japan
[15] iXonEM+ from ANDOR Technology Ltd., Belfast, UK

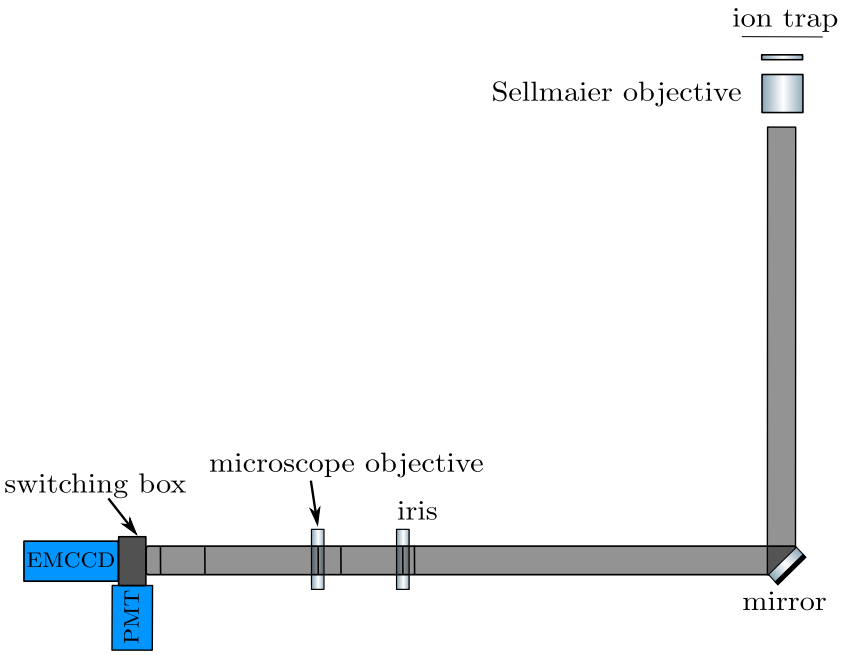

Figure 5.10: Schematic drawing of the imaging system. The whole beam path is enclosed in a tube system (black). In the imaging plane of the Sellmaier objective, an aperture reduces stray light before the second magnification stage realized with a microscope objective. The flip mirror to switch between an EMCCD camera and a PMT is placed in the "switching box".

determine the position of the trap center to which the beams should be aligned.

5.4 Trap electronics

Trapping ions in linear Paul traps is realized with two different kinds of fields. A radiofrequency potential confines the ion in the radial direction while electrostatic fields provide the axial confinement. In both cases, voltages are supplied to the electrodes of the SpyderTrap to create the fields. An oscillator induces the rf voltages, while the experimental control unit generates the dc voltages. Furthermore, this unit provides the microwave pulses and schedules the pulse sequences of each experiment, as described in the following.

5.4.1 Experimental control

The experimental control unit used in this work was developed at the National Institute of Standards and Technology (NIST) in Boulder, CO. It is described in detail in reference [103]. As part of [112], the hardware for our setup was realized and the software ported to Windows 7 and Visual C++ 2010. Furthermore, obsolete

build dependencies were removed through the introduction of a new NI-DAQ "glue layer". The unit consists of a field programmable gate array (FPGA), reconfigurable digital logic devices which are capable of generating arbitrary logic functions. It enables controlling the communication of the computer with hardware devices to create three types of output signals: TTL pulses, sinusoidal and analogue signals. With these signal forms we can control the complete experimental setup.

The TTL signals are used to execute the sequence of an experiment by switching any operation. For example, consider switching the acousto-optic modulators in beam paths to control laser interactions. Here, the FPGA switches the TTL output between two logical levels, 0 V and 3.3 V, in 16 ns. The technical realization of the experimental control limits the minimum time of such pulses, meaning any operation is turned on/off for at least 48 ns. Besides switching TTL signals, the FPGA is also able to count TTL pulses from PMTs, converting the fluorescence into a count rate.

The sinusoidal signal provides the basis for the microwave pulses driving all carrier and sideband transitions needed in the experiment. These signals are created by direct digital synthesizers (DDS). The frequencies and phases of those signals are set by the FPGA, which is synchronized with a 62.5 MHz reference which gives the limit of 16 ns, mentioned above. To create precise DDS signals, an additional 1 GHz reference is used. That reference limits the output frequency to 500 MHz according to the Nyquist-Shannon theorem [113]. Both reference frequencies are created from a module phase locked to a 10 MHz reference, which is provided by an ultra-stable maser accessible at PTB. To achieve signals in the 1 GHz regime we quadruple the frequencies after the DDS module, as described in detail in section 5.4.3.

The analogue signals provide dc voltages for the axial confinement. They are created by a module called "waveform card" developed at NIST [114, 115]. This module allows output signals between -10 V and 10 V, sufficient for the axial confinement provided by the dc electrodes. Signals can be changed almost continuously with a rate of 50 MSamples/s in discrete steps of 0.3 mV. This is important to precisely control the position of the trapped ion and hence be able to minimize micromotion by positioning the ion at the rf pseudopotential null. For more detailed information and characterization of the experimental control see [103, 112, 104].

5.4.2 Trap drive

The most common way to supply the high voltages for the radial confinement of an ion trap is by amplifying an oscillator signal with a high Q step-up resonator, enabling voltages up to several kV. In the case of surface-electrode ion traps, the required voltages are lower (up to a few hundred Volts instead of kV) compared to standard 3D ion traps and can be provided by electronic circuits. This is especially important for traps with adjustable rf voltages [116].

In our recent trap design a single split rf electrode supplies the radial confinement (cf. section 4.2). For this trap, we step up the signal of a HP 8640 oscillator[16] using a quarter-wave resonator in a coaxial design with a helical inner conductor made out of copper. The rf signal is sent via rf feed lines through the top flange of the vacuum chamber. To monitor the power, a directional coupler picks up a small part of the voltage before the resonator. From resonance measurements, we can determine the characteristics of the resonator and the trap capacitance. Here, the resonator is approximated as a parallel RLC circuit, where the drive frequency Ω_{rf} is determined through the inductance and capacitance of the system

$$\Omega_{\mathrm{rf}} = \frac{1}{\sqrt{LC}}.$$

The Q factor is then

$$Q_L = RC\ \Omega_{\mathrm{rf}},$$

where R represents the resistance of the helical resonator. Fitting the data points in Figure 5.11 leads approximately to $L = 205\,\mathrm{nH}$, $C = 1.8\,\mathrm{pF}$ and an unloaded Q factor of 424. The trap capacitance is determined to $C_T = 14\,\mathrm{pF}$ from a resonance frequency $\Omega_{\mathrm{rf}} = 2\pi \cdot 88\,\mathrm{MHz}$ while the loaded resonator has a resistance of about $R = 48\,\mathrm{k}\Omega$ and a Q factor of 212. We work at a voltage of 50 V, leading to a trap depth of approximately 39 meV and a trap frequency $\omega_{x,z}$ of about $2\pi \cdot 11\,\mathrm{MHz}$.

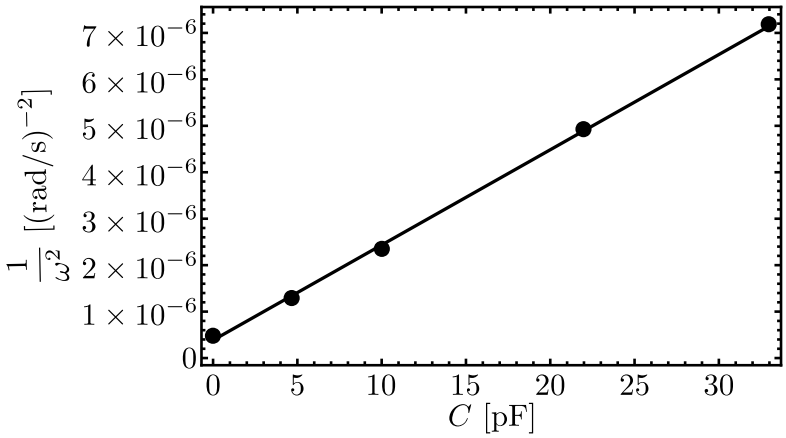

Figure 5.11: Characterization of the helical resonator by measuring the resonance frequency for different capacitive loads. A linear fit enables determining the characteristic inductance L, capacitance C and the quality factor Q for the unloaded resonator. Furthermore, the capacitance of the trap and the quality factor for that case can be determined.

To enable parametric excitation of the trapped ions, a directional coupler is added between the HP 8640 and the resonator excitation port. The coupler is

[16] Hewlett-Packard Inc, Palo Alto, CA, USA

driven in the reverse direction. A signal 10 MHz detuned from the rf drive frequency generated by a DDS module is coupled to the rf signal, which can be scanned over a range of a few tens of Megahertz. This leads to a trap potential modulated with roughly the trap frequency. A more detailed description of the parametric heating process can be found in section 6.2.2.

5.4.3 Microwave drive system

All experiments performed employ microwave pulses to address the hyperfine states in the $^2S_{1/2}$ manifold. In total four different frequencies, 853 MHz, 1083 MHz, 1240 MHz and 1398 MHz are necessary, as depicted in Figure 5.12. The experimental control unit cannot provide these frequencies directly, since the frequencies available are limited to 500 MHz. However, quadrupling the sinusoidal signals yields all required frequencies. Here, the quadrupling stage as well as the main principle of pulse generation are described.

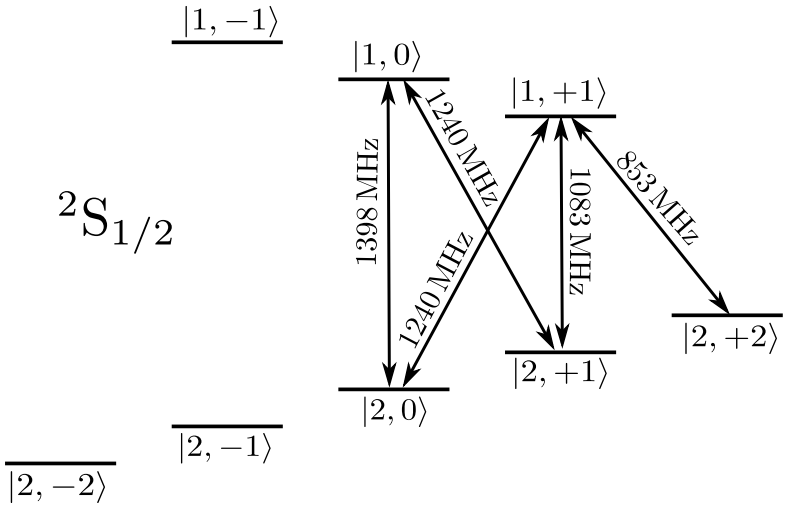

Figure 5.12: Overview of the transitions to address in the $^2S_{1/2}$ manifold. The microwave drive system is designed to supply pulses with frequencies between 800 and 1400 MHz.

The quadrupling stage consists of two frequency doublers of the type "FK-3000+", low- and high pass filters of the type SLP and SHP, attenuators and two amplifiers, ZFL − 500HLN+ and ZFL − 2000LN. All components used are commercially available Mini-Circuits[17] parts. The complete signal path is illustrated in Figure 5.13. The first filter in the signal path eliminates any image frequencies occurring in the sinusoidal signal from the DDS module. Before the signal is frequency-doubled for the first time, the power level is adjusted using a combination of attenuators and amplifiers. This is necessary, since the frequency doublers

[17]Mini-Circuits, Brooklyn, NY, USA

require an input level between +12 dBm and +15 dBm. Undesired harmonics are suppressed using high-pass and low-pass filters in combination. Then, the signal is frequency doubled. The section of the signal line to the next doubler is set up equivalently, but substituting filters and amplifiers by components with a suitable frequency range. After the last doubling stage, a final high-pass filter suppresses all lower frequency signals. The next step is to convert the sinusoidal signal into pulses with an adjustable duration. We use a switch[18] to multiply the signal with a square wave. The resulting pulses can either be used to drive sideband or carrier transitions. Depending on the application, the signals must be amplified differently. For the former, we use a 50 W amplifier[19], since the sideband electrode has an impedance of about 40 Ω and currents up to 1 A are applied. In contrast, carrier transitions need less microwave power. We use a 10 W amplifier[20]. This amplifier is not used at its maximum output power level, but is able to drive all carrier transitions within a few microseconds (cf. section 6.1.2). A detailed characterization of the microwave drive system can be found in [104]. In total, three complete signal paths are set up to provide carrier, red and blue sideband transitions simultaneously. Red and blue sideband pulses are combined before the amplifier and fed via SMA cable to the filterboard, where the signal line is in a coplanar waveguide configuration. The carrier signal line is set up equivalently.

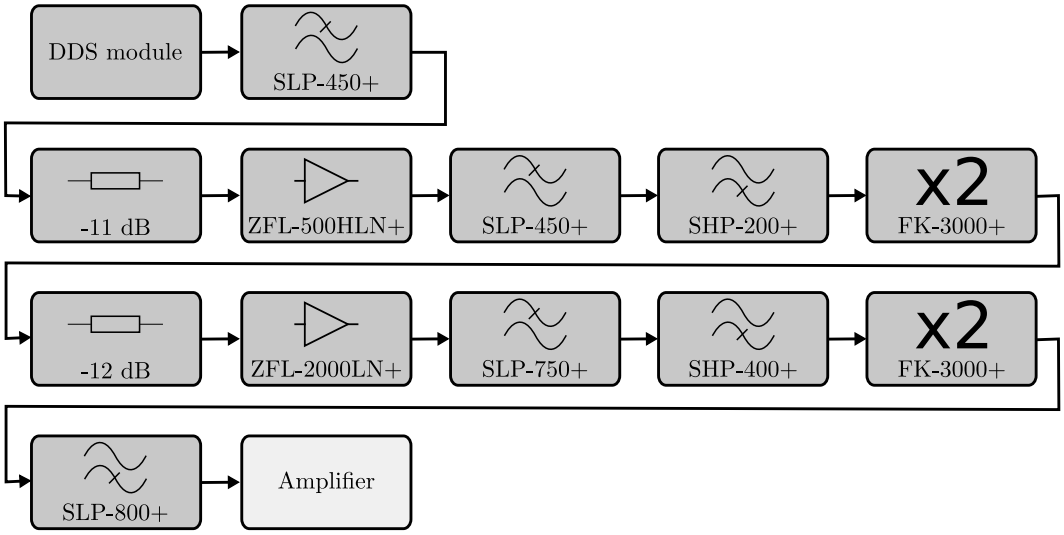

Figure 5.13: Complete signal path of the quadrupling stage for generating microwave signals with the required frequencies to address the hyperfine states in the $^2S_{1/2}$ manifold of $^9Be^+$. The input level for the frequency doublers is achieved by a combination of amplifiers and attenuators, while several filter stages eliminate undesired frequency components.

[18] ZASWA-2-50DR+ from Mini-Circuits, Brooklyn, NY, USA

[19] RUP15050-12 from RFHIC Bldg. 41-14, 170 beon-gil, Burim-ro, Dongan-gu, Anyang-si, Gyeonggi-do, 431-769 Rep. of KOREA

[20] ZRL-1150LN+ from Mini-Circuits, Brooklyn, NY, USA

Chapter 6

Probing microwave near-fields using a single ion

The surface-electrode ion trap developed in this work features a single microwave electrode embedded into the trap structure. With the electric fields creating the trapping potential and the magnetic near-field to address and control the ions given by design, it is essential to accurately predict the field configuration. By measuring the magnetic field generated by the single electrode, we are able to validate our numerical simulations. Since no measurement techniques are available to measure the near-field with a resolution below 1 μm at a frequency of around 1 GHz a few tens of microns above a surface [117], we probe the near-field using a single trapped ion. Here, the ion is displaced from its null position and the magnetic field is measured a few microns around that position. The size of the magnetic near-field map depends on the stability regions of the trap. Before performing such a measurement, it is necessary to localize the ion by reducing motional energy, and to prepare it in a well-defined state. Figure 6.1 shows the relevant transitions for probing the magnetic near-field with the ion. Micromotion compensation reveals the null position of the rf pseudopotential and by measuring the trap frequencies, we can determine the displacements as a function of the applied shim fields. To observe the complete magnetic field behavior, the AC Zeeman shifts of two transitions are measured. In this chapter, I present the experimental steps towards mapping the magnetic near-field using a single ion, the reference measurement for the comparison with the simulation. Furthermore, I show first exploratory results for manipulating the field configuration by changing the termination of the microwave carrier electrode.

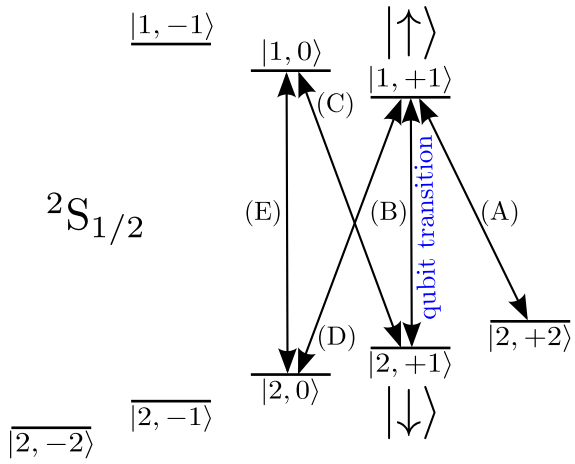

Figure 6.1: Hyperfine levels of the $^2S_{1/2}$ ground state of $^9Be^+$ with relevant transitions for state initialization and magnetic near-field measurement. We measure the AC Zeeman shift on transition (B), the qubit transition and on transition (E). The hyperfine levels are given in the $|F, m_F\rangle$ notation, as described in chapter 3.

6.1 Preparing the ion

Measuring the magnetic field created by the single meander electrode with a single ion requires initialization of the state in which the measurement is performed. The initialization includes cooling the ion to reduce its average kinetic energy. The ion is initialized in the $|F = 2, m_F = +2\rangle$ state of the $^2S_{1/2}$ manifold of $^9Be^+$. Microwave pulses transfer the population to the relevant state for the measurement.

6.1.1 Doppler cooling

Doppler cooling is an essential process for trapped-ion experiments, in which the interaction with laser light reduces the average kinetic energy. Without reducing the kinetic energy of a trapped ion, its lifetime in the trap decreases significantly; due to the high kinetic energy, it can easily escape from the trapping potential. Further, cooling strongly localizes the ion and initializes the ion's motional state.

A single laser beam is able to damp the ion's oscillations as long as each normal mode of the oscillation has a projection onto the beam. This laser beam is red-detuned from a closed two-level transition, in our case the transition $^2S_{1/2}$ $|F = 2, m_F = +2\rangle \leftrightarrow {}^2P_{3/2}$ $|m_J = 3/2, m_I = 3/2\rangle$. The interaction with the laser beam leads to absorption and emission of photons at the frequency of the transitions. Due to momentum conservation, both absorption and emission lead to a momentum kick $\Delta p = \hbar k$. While absorption gives a momentum kick in the direction of the wave-vector k, the ion scatters the emitted photons statistically in all possible directions. Hence, the emission leads to an average zero-momentum transfer.

Consider an ion moving with a velocity v_z in a laser field red-detuned by Δ from the atomic resonance ω_0. Due to the Doppler effect, an ion moving in the direction of the laser beam sees a frequency shifted by $k_z v_z$ towards the atomic resonance. In contrast, an ion moving away from the laser beam sees an even larger detuning of $\Delta + k_z v_z$ from resonance and hence scatters less photons. Thus, the ion experiences a net momentum transfer which reduces the motion. The ion's motion reaches an equilibrium when cooling and heating through the random emission of photons have the same rate. For a detuning of $\Delta = \Gamma/2$ with intensities well below the saturation intensity, the so-called Doppler limit is reached. The motion of the ion can be associated with a temperature of

$$k_B T_{min} = \frac{\hbar\Gamma}{2}, \tag{6.1}$$

where k_B is the Boltzmann constant and Γ the natural line width of the excited state. The process described here is a simplified picture; detailed information on Doppler cooling can be found in [88, 118, 119]. The first demonstration experiments for Doppler cooling of ions were performed in 1978 [12, 13].

As mentioned before, to cool the ion's motion in all directions, each normal mode must have a non-vanishing projection onto the laser beam. In the experiment, the laser beam is aligned with the quantization axis which is determined by the external magnetic field $\vec{B_0}$. Figure 6.2 illustrates the coordinate system relevant for our experiment. To cool not only the motion in the radial direction, the quantization axis is tilted relative to the xz-plane of the SpyderTrap. Ideally, the tilt would be 45°; however, then the projected parallel component of the oscillating magnetic field decreases. As a compromise, we choose a tilt of 12° to achieve a high gradient for sideband transitions. We can cool both normal modes of the radial confinement by applying a static potential which tilts the normal modes. In the present setup, the modes are tilted by $\approx 22°$. In this configuration we can cool each direction of the ion's motion.

To prepare the ion, we use two overlapping σ_+ beams for Doppler cooling on the $^2\mathrm{S}_{1/2}\ |2,+2\rangle \leftrightarrow {}^2\mathrm{P}_{3/2}\ |3/2,3/2\rangle$ cycling transition at 313 nm. The first is 856 MHz red-detuned to cool hot ions during the loading procedure and has approximately 10 μW power at a 30 μm waist. The second beam is detuned by approximately half the natural linewidth of the $^2\mathrm{P}_{3/2}$ state ($\Gamma/2 \approx 10$ MHz) and the power is about half the saturation intensity. This beam performs Doppler cooling for slower ions and initializes the ion into the $^2\mathrm{S}_{1/2}\ |2,+2\rangle$ state via optical pumping. The whole process takes about 3 ms in our experiment, mainly to limit the duty cycle for the high power applied to the meander electrode. Actual cooling times could be much shorter. The final cooling is performed during 10 μs, where only the resonant Doppler beam is applied. Working at the Doppler cooling limit is sufficient for the experiments performed in this thesis. Subsequent experiments might require cooling to the ground state, which is possible with resolved sideband cooling [120].

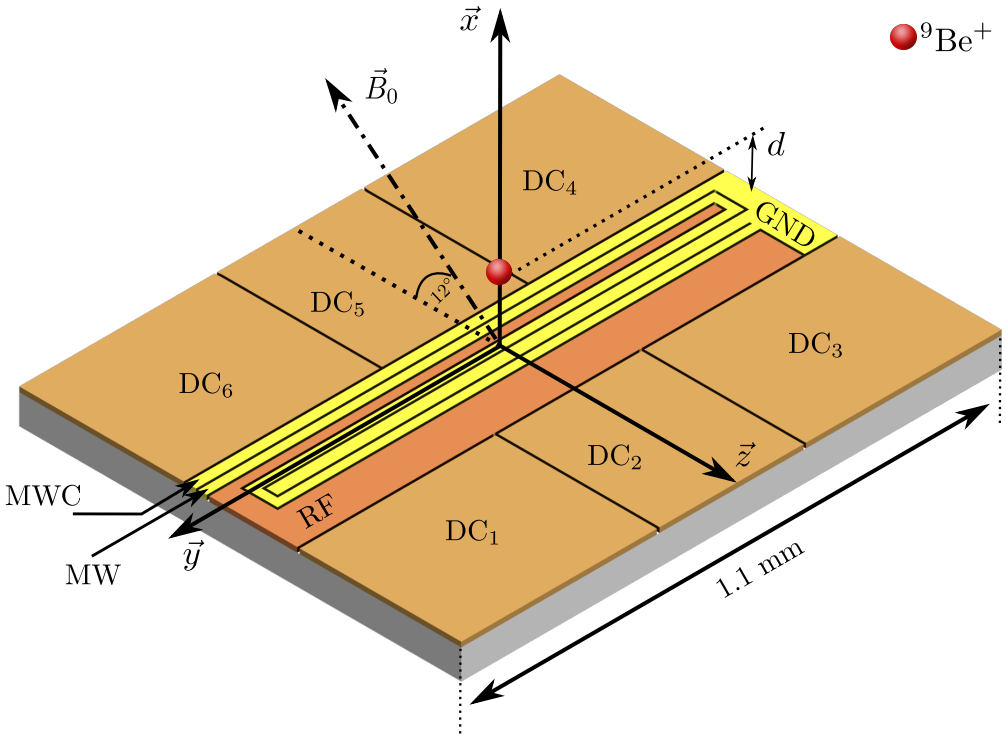

Figure 6.2: We probe the magnetic field provided by meander electrode (MW) using a single $^9Be^+$ ion trapped 45 μm above the surface. The RF and DC$_{1-6}$ electrodes define the trapping potential. Microwave transfer pulses are provided by applying a current on MWC. The quantization axis defined by $\vec{B}_0$ is tilted by 12° with respect to the radial plane, enabling laser cooling in all directions.

6.1.2 State initialization

Cooling the ions is one part of the state initialization, which prepares the ion in the $|2, +2\rangle$ state in the hyperfine manifold of the $^2S_{1/2}$ ground state (cf. Figure 6.1). This state is our initial state and is used for fluorescence detection. To perform the fluorescence detection, we tune the near-resonant Doppler beam to resonance. Through a series of suitable microwave π-pulses[1] resonant with corresponding hyperfine transitions, we can prepare any state in the hyperfine manifold. We determine the population of the prepared state by transferring the population back to the $|2, +2\rangle$ state and detecting fluorescence with a PMT (see section 5.3.3). The transfer pulses are provided by the microwave carrier electrode (cf. Fig. 6.2). The pulse lengths are typically on the order of a microsecond. For the magnetic field measurement, we are interested in two transitions in the hyperfine manifold to

[1] π-pulse refers to a pulse translating the complete population with the Rabi frequency Ω in time τ_π. For the Rabi rate, we use a convention (D. Wineland, NIST [20]) which implies $\Omega\tau_\pi = \pi/2$.

identify the parameters for the 2D quadrupole description[2] presented in section 3.3. One is the qubit transition $|2,+1\rangle \leftrightarrow |1,+1\rangle$ and the other is the transition $|2,0\rangle \leftrightarrow |1,0\rangle$[3], (B) and (E), respectively, as indicated in Figure 6.1. Figure 6.3 shows Rabi oscillations on the field-independent qubit transition with a π-time of $\tau = 0.507\,\mu$s. Using the definition of the Rabi rate for a carrier transition (Eq. 3.21), the amplitude of the magnetic field driving the transition is $B = 72\,\mu$T.

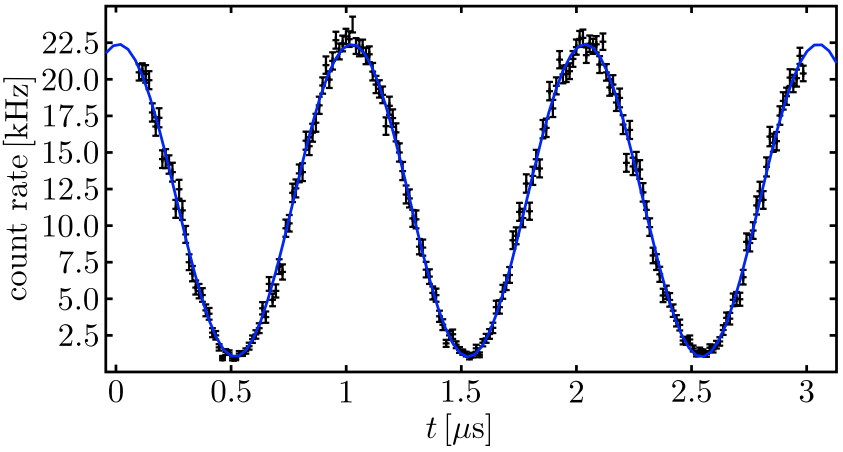

Figure 6.3: Rabi oscillation on the field-independent qubit transition induced by a magnetic field provided by the microwave carrier electrode (MWC). Here, error bars indicate the statistical uncertainties of 500 measurements.

The state initialization including shelving for the detection is schematically illustrated in Figure 6.4 for both transitions (B) and (E), respectively. To perform experiments on the qubit transition (B), we prepare the ion in the $|\uparrow\rangle = |1,+1\rangle$ state of our qubit by transferring the population from $|2,+2\rangle$ to $|1,+1\rangle$. After an experiment sequence, we detect the final state by transferring the population of the $|\uparrow\rangle$ state back to the initial state for fluorescence detection. To avoid off-resonant transitions from the $|\downarrow\rangle = |2,1\rangle$ state into the $^2\mathrm{P}_{3/2}$ manifold, its population is shelved into a far-detuned state in the $F = 1$ manifold of the $^2\mathrm{S}_{1/2}$ ground state, here into $|1,0\rangle$. Shelving increases significantly the contrast of the state detection.

For the second transition (E), the ion is prepared in the $|2,0\rangle$ state, by transferring the population from the initial state $|2,+2\rangle$ via $|1,+1\rangle$ to $|2,0\rangle$. In this case we detect the population of the lower state, reversing the preparation process to transfer its population back to the initial state for detection. Since the frequencies of transition (C) and (D), as defined in Figure 6.1, differ only by a few MHz, the

[2]This 2D model characterizes the magnetic near-field in terms of five parameters such as strength and orientation of the zero and first order terms of the magnetic near-field.

[3]As we will see later, the corresponding AC Zeeman shift exploited in the near-field measurements is significantly different for these transitions for a field with a frequency close to a sideband transitions of the qubit.

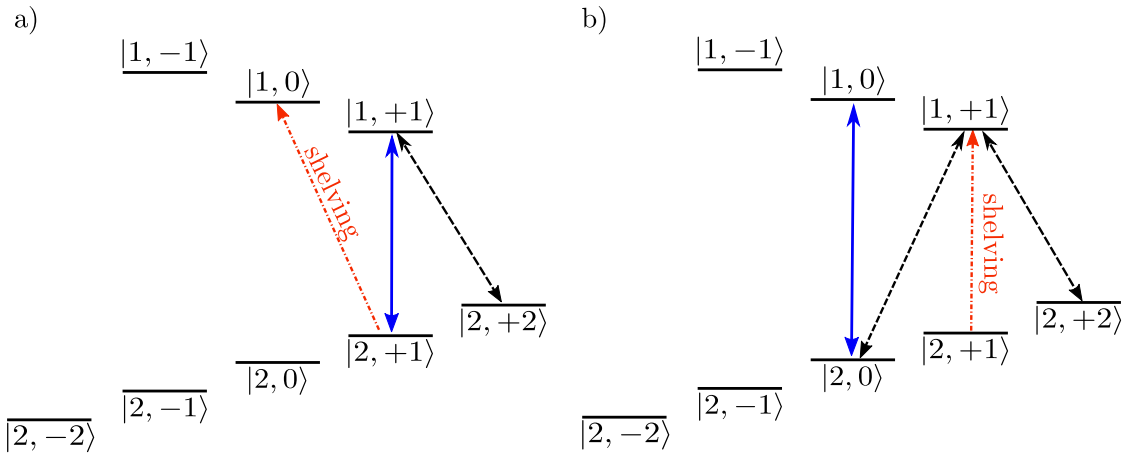

Figure 6.4: State initialization and detection sequence for the two transitions used for the magnetic field measurement. a) shows pulses needed for qubit transition (B) and b) those for the transition $|2,0\rangle \leftrightarrow |1,0\rangle$ (E). The black arrows indicate microwave π-pulses for the initialization and the transfer to $|2,+2\rangle$. The shelving pulses are illustrated with red arrows. The measured transitions are indicated with blue arrows. We shelve the population from $|2,+1\rangle$ to either $|1,0\rangle$ or $|1,+1\rangle$ to avoid off-resonant transitions and hence a loss in contrast.

population in $|1,0\rangle$ can be unintentionally transferred to $|2,+1\rangle$. We shelve this population to $|1,+1\rangle$.

6.2 Characterizing the rf pseudopotential

Measuring the magnetic near-field distribution requires a determination of the relative position of the ion. We measure the field relative to the rf pseudopotential null, which can be found by compensating micromotion (cf. chapter 2). By applying different shim fields on the dc electrodes, we are able to displace the ion in the radial plane and measure the field at different positions. We determine the relative displacement based on the trap parameters. This is only possible if the measured potential is sufficiently well described by the model. We test this by measuring the trap frequencies, which are directly related to the potential.

The potential used in the magnetic field measurement is supplied by a $2\pi\cdot 88\,\mathrm{MHz}$ rf signal with an amplitude of 50 V and a set of dc voltages determined using certain assumptions described in section 2.2.1. We reduce the remaining free parameters by setting the axial frequency to 1 MHz and one of the voltages to a fixed value, here $U_{\mathrm{DC}_4} = 2\,V$. The applied voltages are then $U_{\mathrm{DC}_1} = U_{\mathrm{DC}_3} = -2.71\,\mathrm{V}$, $U_{\mathrm{DC}_2} = 0.86\,\mathrm{V}$, $U_{\mathrm{DC}_6} = U_{\mathrm{DC}_4} = 2\,\mathrm{V}$ and $U_{\mathrm{DC}_5} = -0.47\,\mathrm{V}$. The resulting potential is shown in Figure 6.5; here the axes of the normal modes of the secular motion are indicated. The axes are tilted by 22.45° due to the applied DC potential. The combined

potential leads to radial mode frequencies of $2\pi \cdot 10.9\,\mathrm{MHz}$ and $2\pi \cdot 11.16\,\mathrm{MHz}$ for the low and high frequency mode (LF and HF), respectively. The trap depth is $\approx 39\,\mathrm{meV}$. We determine the position of the minimum of the combined potential by solving for the zero position of the gradient of the total potential. If that position coincides with the rf null position which is at $(x_{\mathrm{rf}}, z_{\mathrm{rf}}) = (45.7\,\mu\mathrm{m}, 2.9\,\mu\mathrm{m})$, the ion experiences no excess micromotion. By compensating the micromotion, we can find the position of the rf null in the experiment, as described in section 6.2.2.

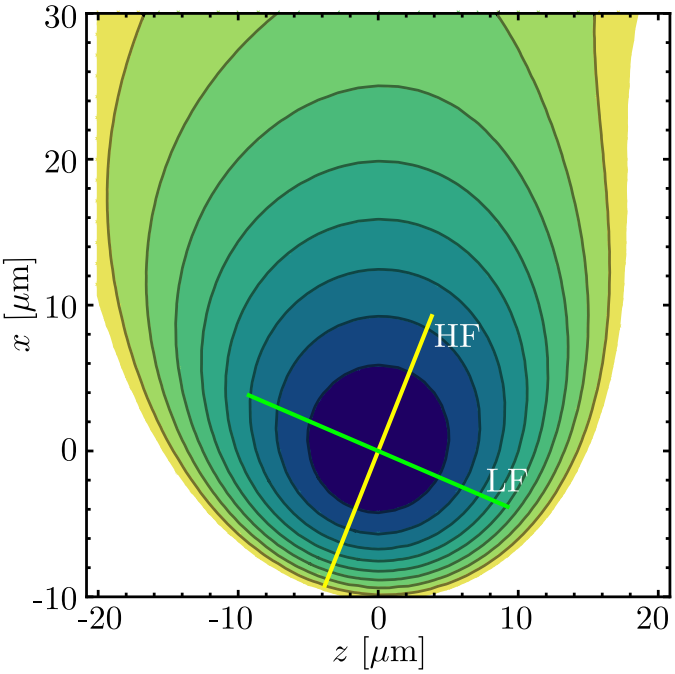

Figure 6.5: Potential of the combined dc fields and rf pseudopotential, as a function of position in x- and z-direction in relative to the position at which the rf pseudopotential is zero. The axis of the low and high frequency normal modes, LF and HF respectively, are indicated as oriented in the experiment.

To displace the ion in the radial plane, an offset field ΔE is applied which moves the ion in one of the radial directions. This offset field arises from a suitable linear combination of dc voltages added to the applied voltages $U_{\mathrm{DC}_{1-6}}$. The additional voltages are on the order of a few milliVolt. For the mapping procedure, the ion is displaced in the x- and z-direction with a fixed step width for the added shim fields ΔE_x and ΔE_z. We determine each position for its given set of shim fields by setting the resulting gradient of the potential to zero:

$$\frac{\delta\phi_{trap}(\mathbf{r}, \Delta E_x, \Delta E_z)}{\delta x} = \frac{\delta\phi_{trap}(\mathbf{r}, \Delta E_x, \Delta E_z)}{\delta z} = 0. \tag{6.2}$$

Hence, we obtain the position in the trapping potential as a function of shim field in terms of the pseudopotential null position at which the shim fields are zero.

6.2.1 Secular frequency measurement

Secular frequencies can be measured by applying an oscillatory field near the expected secular frequency to one of the dc trap electrodes. This will create an oscillatory electric field which can resonantly drive the motion of the ion and create large Doppler shifts through the resulting ion velocities. These Doppler shifts lead to a loss of count rate in the ion detection and can be observed as a dip in a frequency scan of the count rate. We measure all secular frequencies, radial and axial, with this method. Figure 6.6 shows the measurement of the high frequency radial mode. All trap frequencies differ only slightly from the predictable value. Small deviations can occur due to deviations in the rf power at the trap. The measured frequencies correspond to an rf amplitude of 48 V.

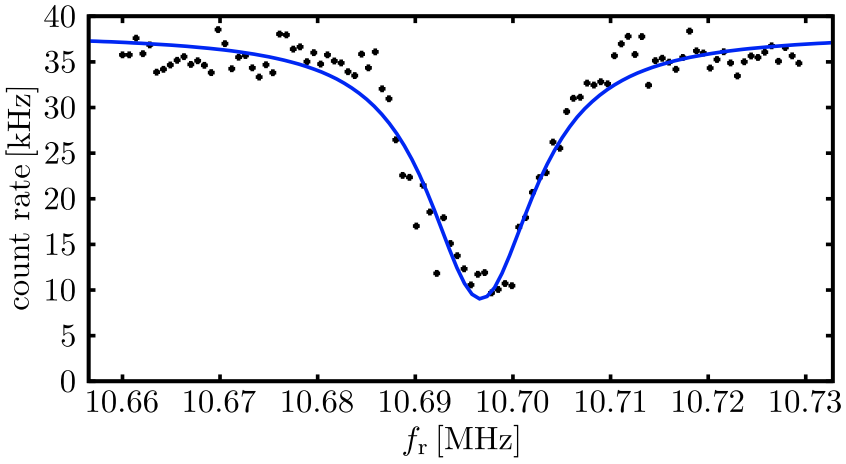

Figure 6.6: Secular frequency of the high frequency mode in the radial plane measured by resonantly driving the ion's motion. The resonances is at ≈ 10.7 MHz which correspond to an rf amplitude of 48 V.

6.2.2 Micromotion compensation

To find the rf pseudopotential null, we compensate the micromotion. As mentioned before, any displacement of the ion from the rf pseudopotential null leads to excess micromotion. This type of micromotion can be compensated by adjusting the dc potential ϕ_{DC} with shim fields. We implement two different techniques to compensate micromotion: parametric heating [121] and the microwave approach for rf micromotion compensation first demonstrated in [95].

Parametric heating

Parametric heating describes the process of heating the ion by resonantly exciting the secular motion. It is based on the the principle of a parametric oscillator

which describes the driving of an oscillation by modulating one of the characteristic parameters of the system. Here, the trap frequency is one of the characteristic parameters of the trapping potential. Hence, modulating the rf driving amplitude with the trap frequency resonantly excites the secular motion of the ion which leads to ion heating. The heating process changes the fluorescence and we can measure the parametric resonances [121], the trap frequencies. This principle can be used to compensate micromotion since the motion can only be excited if the ion is displaced from the rf null position. Hence, if the parametric resonances are detectable, the ion undergoes excess micromotion. To determine the parametric resonances, we scan over a frequency range around the estimated values and detect the ion's fluorescence. By adjusting the shim fields individually for both, high and low frequency mode, we can compensate micromotion in all radial directions. At the pseudopotential null, the parametric resonances vanish for both radial trap frequencies. Close to the rf null position we heat the ion for about 2 ms before measuring the fluorescence. Figure 6.7 shows the dips for two trap frequencies corresponding to the low frequency and high frequency radial mode, respectively.

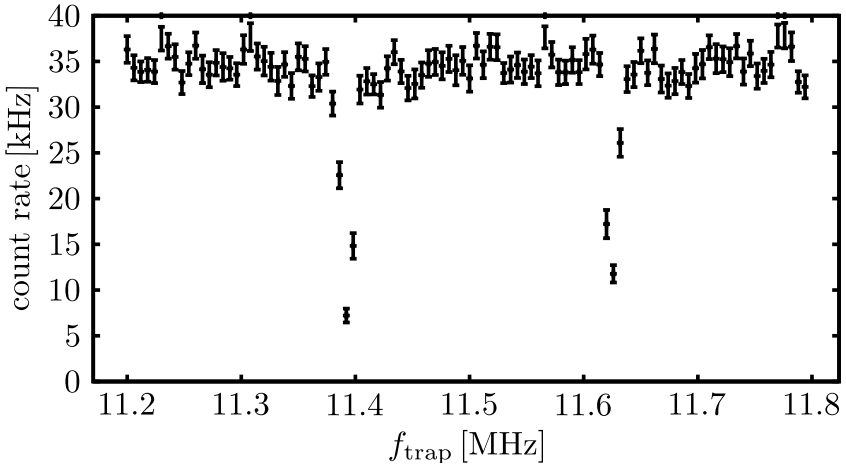

Figure 6.7: Trap frequencies in radial plane measured by parametrically heating the secular motions of the ion. The two resonances at 11.39 MHz and 11.64 MHz give the frequencies for the low and high frequency mode, respectively.

Microwave approach

The microwave approach for rf micromotion compensation [95] is based on the fact that the micromotion induces sidebands $\pm n\Omega_{rf}, n \in \mathbb{N}$ on carrier transitions in the excitation spectrum. By tuning the field to one of these sidebands, we can drive carrier transitions which depend on the amplitude of the micromotion with the gradient of the magnetic field. Using the meander electrode offers micromotion compensation in every direction in the radial plane due to the quadrupole-like field

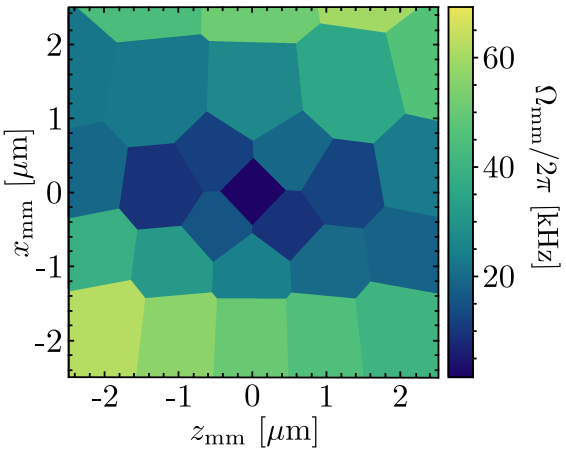

Figure 6.8: Micromotion map. Measurement of rabi rates Ω_{mm} induced by micromotion sidebands as a function of position in the radial plane. Here, the rf pseudopotential null coincides with the coordinate origin. The Rabi rate of the micromotion sidebands is proportional to the micromotion amplitude and vanishes for the compensated ion.

configuration.

The micromotion amplitude is usually described as a function of the driving frequency Ω_{rf} and the position $\mathbf{r}_{mm} = (x_{mm}\mathbf{e}_x + y_{mm}\mathbf{e}_y + z_{mm}\mathbf{e}_z) \cdot \cos(\Omega_{rf}t)$. In the specific case of applying a magnetic field gradient B' provided by the meander electrode with a frequency of $f_{\mathrm{HFS}} + f_{\mathrm{RF}}$, the ion senses a field oscillating at f_{HFS} with an amplitude $\mathbf{B}_{mm}$ given by

$$\mathbf{B}_{mm} = \frac{1}{2}B' \begin{pmatrix} \cos\beta_{mm} & \sin\beta_{mm} \\ \sin\beta_{mm} & -\cos\beta_{mm} \end{pmatrix} \begin{pmatrix} x_{mm} \\ z_{mm} \end{pmatrix}, \tag{6.3}$$

where β_{mm} describes the orientation of the magnetic field quadrupole and f_{HFS} a transition between states in the hyperfine manifold of the ground state. Here, we consider only the linear component of the 2D microwave near-field model (cf. section 3.3) and assume a linear polarization. The resulting Rabi rate for a transition in the hyperfine manifold is

$$\Omega_{mm} = \frac{1}{2}B^p_{mm}\frac{\mu}{2\hbar}, \tag{6.4}$$

where μ is the magnetic dipole matrix element of the hyperfine carrier transition involved and B^p_{mm} is the polarization component of $\mathbf{B}_{mm}$ which drives the chosen hyperfine transition. The Rabi rate is directly proportional to the field $\mathbf{B}_{mm}$ and hence to the micromotion amplitude. Therefore, we minimize micromotion by minimizing the Rabi rate. For this purpose, we measure the Rabi rate at different positions, as shown in Figure 6.8. Any radial micromotion would thus lead to an oscillatory magnetic field at f_{HFS} in the frame of the ion. This field would also be oriented in the radial plane. If we use a $\Delta m_F = \pm 1$ transition (such as

$|2,+2\rangle \leftrightarrow |1,+1\rangle$), such a radial oscillatory magnetic field will always have a finite projection on $\mathbf{B}_0$, which is oriented at 12° with respect to the radial plane. It would thus always lead to Rabi oscillations on such a transition. These Rabi oscillations can then be minimized to minimize micromotion. When using a $\Delta m_F = 0$ transition (such as $|2,+1\rangle \leftrightarrow |1,+1\rangle$), radial microwave fields perpendicular to the surface and resulting from micromotion cannot be sensed because such fields would also be perpendicular to $\mathbf{B}_0$. Nevertheless, such transitions can serve as a valid cross-check. At the rf null position the Rabi rates vanish in the ideal case. However, in the experiment, the scanning range is limited to 2 ms. Hence, any rabi rate below ≈ 80 Hz is not measurable. With a gradient as high as 50 T/m, this correspond to a micromotion amplitude below 1 nm.

Based on these measurements, the shim field settings to compensate micromotion in the SpyderTrap are known, as well as the rf null position. Next, we measure the magnetic field around the null position by exploiting AC Zeeman shifts.

6.3 Measuring the magnetic near-field

The magnetic field provided by the meander conductor is characterized by measuring the AC Zeeman shift induced on the hyperfine states of the ion by an oscillating magnetic field. Such a shift can either be measured by Rabi spectroscopy [122] or the Ramsey method presented in [95]. We employ here the latter because the required experimental sequence can be implemented in an easy automation routine.

6.3.1 Ramsey method

The Ramsey method developed in [95] is a conventional Ramsey sequence with a spin echo pulse separating the interferometer into two "slots" , an energy shift inserted into one "slot" of the interferometer, as well as a spatial displacement of the ion within each interferometer "slot" to be able to measure the influence of the near-field as a function of position. The basic procedure can be described as follows: The ion is prepared in a state $|a\rangle$ in the hyperfine manifold of the ground state $S_{1/2}$. We irradiate a $\pi/2$-pulse resonant with a transition to the state $|b\rangle$, and then apply the microwave drive on the meander electrode for a variable time $\mathrm{T_{MW}}$ at a frequency 10 MHz detuned from the qubit transition (B). Through the resulting AC Zeeman shift, the near-field will induce a dephasing of the superposition with respect to an internal clock running at the unperturbed atomic transition frequency. The dephasing can be measured with a second $\pi/2$-pulse with an appropriate phase and by measuring the population in $|a\rangle$ as a function of the drive time T_{MW}. To reduce the effect of magnetic field fluctuations slower than the experiment time of about 500 μs and only measure the dephasing due to the oscillating magnetic field, the experiment makes use of a spin echo. The sequence is illustrated in Figure 6.9 a). For measuring the magnetic field as a function of position, the sequence is

extended by adding the displacement before and after applying the microwave field of the meander (see Figure 6.9 b)). By performing cooling, preparation and detection operations as well as the π- and $\pi/2$-pulses at the rf null position, we can make sure that preparation and manipulation are always done consistently. Note that the Ramsey method does not directly reveal the sign of the AC Zeeman shift. This is not relevant for the near-field measurement; here we use the positive sign for the net shift.

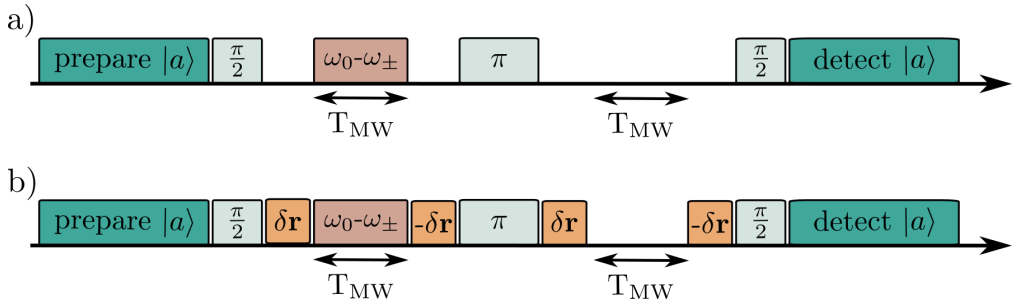

Figure 6.9: Ramsey method to measure microwave near-fields. a) Pulse sequence to measure the magnetic field of an oscillating signal through phase accumulation from the induced AC Zeeman shift while the ion is in a superposition state of $|a\rangle$ and $|b\rangle$. The first $\pi/2$-pulse sets the ion into the superposition state. The microwave pulse detuned from a transition resonance ω_0 by $\omega_\pm$ is applied for a time T_{MW}. The spin echo π-pulse reduces the influence of magnetic field fluctuations. The accumulated phase is then measured with a second $\pi/2$-pulse and by detecting the population in $|a\rangle$. b) shows the extended version, in which the displacement of the ion is included. Here, the ion is moved by $\delta\mathbf{r}$ before and after the microwave field is applied, so that the phase accumulation can be measured at different positions.

To characterize the complete field using the 2D microwave near-field model described in section 3.3, we measure the AC Zeeman shift on different transitions in the hyperfine manifold $^2S_{1/2}$. By choosing two transitions which depend differently on the field components, we are able to reconstruct the parameters of the model. The signal applied to the microwave meander electrode inducing the AC Zeeman shift is 10 MHz blue-detuned from the qubit transition. We choose to measure the induced energy shift on $|2,0\rangle \leftrightarrow |1,0\rangle$, since the corresponding shift depends nearly equally on all field components. For this transition (E) (cf. Figure 6.1), the near-field is red-detuned from all contributing transitions allowed by selection rules, leading to a blue net shift of (E). For the qubit transition, the near-field applied to MW is blue-detuned from the transition frequency, resulting in a red shift of that transition due to the π-component of the field. Since the near-fields in our experiment are mostly linearly polarized, σ^+ and σ^- contribute roughly equally. This leads to a red shift of the qubit transition as a result of the blue-detuned off-resonant coupling to (A) (cf. Figure 6.1). There will also be a strong blue

shift of the qubit transition as a result of the red-detuned off-resonant coupling to (C) and (D). Hence, the π-component of the field induces a strong red shift while the blue shift as a result of the σ-components is rather weak. The spatial structure of the AC Zeeman shift for these two transitions is significantly different. To visualize this idea, we plot the shift induced by a quadrupole field using the simulated magnetic field data. Figure 6.10 shows the pattern of the corresponding AC Zeeman shift δf_{AC} as a function of x and z. The different spatial behavior allows us to obtain complementary information about the magnetic field. Transition (E) reveals information about the strength of the gradient B' and the residual field B and the position of the minimum, whereas the qubit transition allows us to extract the spatial orientations α and β and the polarization ψ. The AC Zeeman shift of transition (E) should exhibit a minimum close to the field minimum of $|\vec{B}|$ while the qubit transition exhibits a more complex structure due to the interplay of the red and blue shifts from the π- and σ-components.

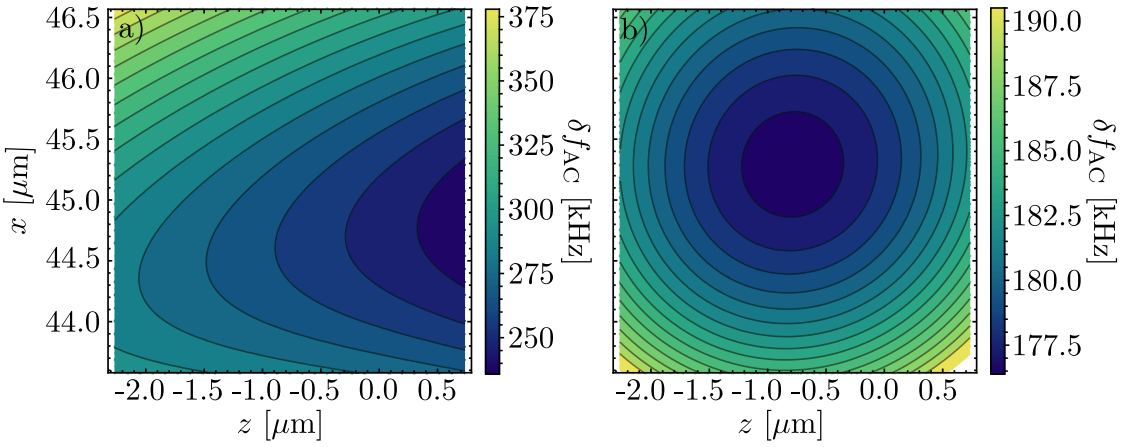

Figure 6.10: AC Zeeman shift induced on different transitions based on the field provided by the numerical simulation. a) shows the pattern for the shift induced on the qubit transition. The influence of the parallel field $B_{\parallel}$ is here predominant. The AC Zeeman shift on the transition $|2,0\rangle \leftrightarrow |1,0\rangle$ transition exhibits a clear minimum. The shifts are plotted as a function of x and z.

In the experiment, we measure the magnetic field provided by the meander electrode (MW) a few microns around the magnetic field minimum. The AC Zeeman shift on transition (E) exhibits a minimum close to that minimum. By measuring AC Zeeman shifts over a large region around the rf null position, the rough position of that transition minimum can be determined. Around the field minimum, the resolution is increased significantly to about $0.25\,\mu$m to achieve an appropriate precision concerning the strength and orientation of the applied magnetic field. The shift on the qubit transition is measured in the same region with identical step size of the electric shim fields. The measured AC Zeeman shift for both transitions

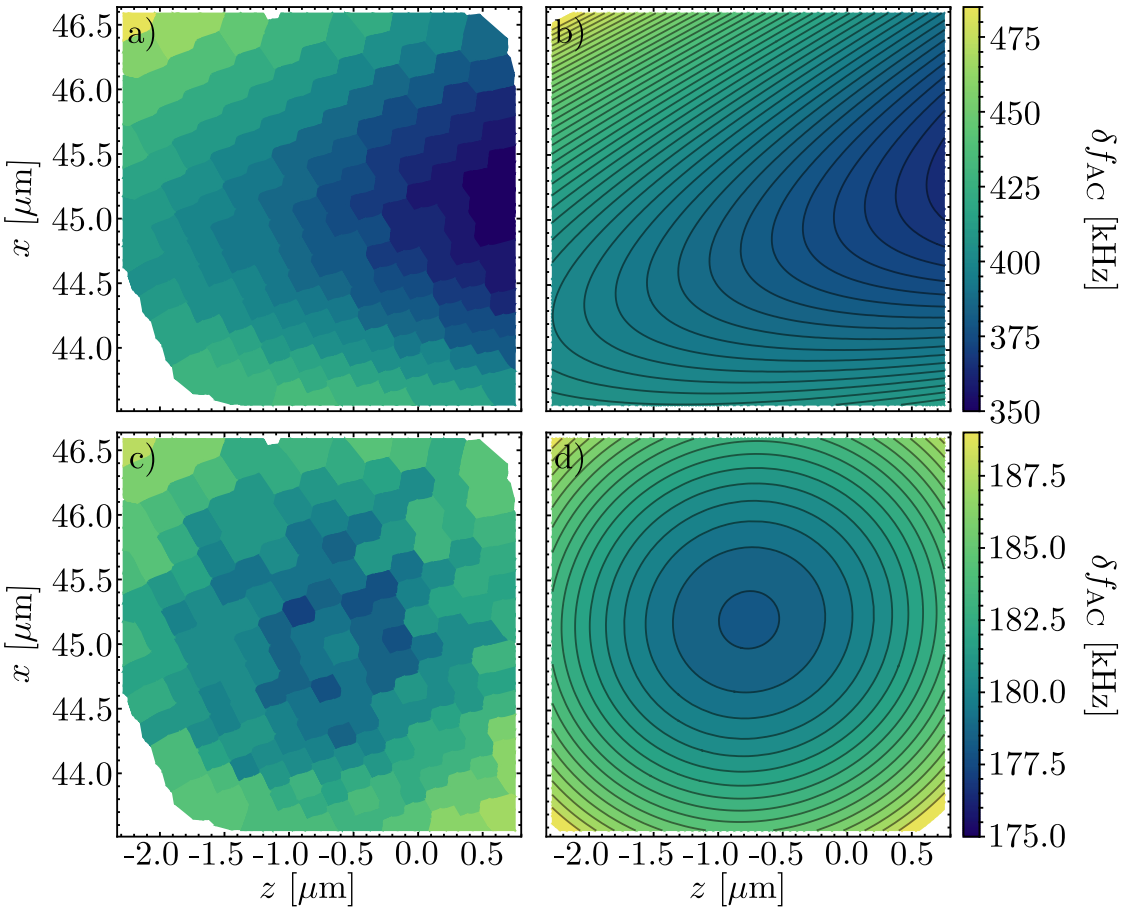

Figure 6.11: AC Zeeman shift δf_{AC} induced on a single $^9Be^+$ ion by the magnetic near-field of the meander electrode. The two rows show the data for $|2,+1\rangle \leftrightarrow |1,+1\rangle$ and $|2,0\rangle \leftrightarrow |1,0\rangle$, respectively. The first column shows the measured shift probed with a single ion. White areas indicate areas in the radial plane where we cannot stably trap ions. The second column shows the result of the least square fit based on the 2D near-field model 3.3.

is shown in Figure 6.11. The left-hand side shows the actual measured data as a function of ion position, whereas the right-hand side is the least square fit of the AC Zeeman shift resulting from the 2D near-field model. Besides the parameters in equation 3.25, in addition, we use the position of the field minimum, x_0 and z_0, as fitting parameters. The data for transition (E) was taken at a power level approximately 6 dB higher than applied for the qubit transition in order to increase AC Zeeman shifts for that level. Hence, we include the experimental power ratio between the two transition in the fitting procedure. The fitting reveals a ratio of 6.47(15) dB. We scale the measured and fitted data in Figure 6.11 to the power level of the qubit transition. For reference, the power level of the qubit transition corresponds to a magnetic field gradient of $B' \approx 45\,\mathrm{T/m}$ whereas the data for

transition (E) was taken with a gradient of $B' \approx 94\,\mathrm{T/m}$. The corresponding residual fields are $393\,\mu\mathrm{T}$ and $825\,\mu\mathrm{T}$, respectively. The figure of merit is then $\eta = 0.001$, which is power independent. This value is rather low because the trap design was not optimized for a good figure of merit. As assumed, the magnetic field is mostly linearly polarized, $\psi = 4.3(1.2)^\circ$. We extract an angle of $\alpha = 31.1(3)$ determining the orientation of the residual field and an angle of $\beta = 109.1(11.5)^\circ$ describing the orientation of the quadrupole gradient matrix in the radial plane. The field minimum is at $(x_0, z_0) = (-0.8, -45.3)\,\mu\mathrm{m}$, which deviates by approximately $0.3\,\mu\mathrm{m}$ in x and by $3.7\,\mu\mathrm{m}$ in z-direction from the rf null position which is determined with electrostatic simulations and the pseudopotential approximation. Comparing the experimental and fitted data reveals a good agreement of our 2D model with the measured data (cf. Table 6.1).

6.3.2 Termination dependence

Numerical simulations show that back-reflected currents have a huge impact on the near-field configuration, especially on the position of the field minimum. While the effect of back-reflected currents on the dc and rf electrodes is negligible, a small back-reflection on the microwave carrier electrode changes the near-field significantly (cf. section 4.2.5). To estimate the current, we measure the S-parameters on the SMA feed-throughs for the microwave carrier and the meander electrode. Specifically, the S_{12} parameter is of interest. That parameter describes the signal which is transmitted to the carrier electrode while applying a signal to the meander electrode. At the qubit frequency $f = 1082.55\,\mathrm{MHz}$, the S-parameter is $S_{12} \approx -9\mathrm{dB}$. Hence, $\approx 12.6\%$ of the power coupled into the meander is transmitted to the microwave carrier electrode. A fraction of that power is reflected back into the structure. Ideally, the feed lines for both electrodes are perfect $50\,\Omega$ line and no back reflection occurs. However, any transition can lead to a small mismatch and hence to a back-reflection. In the experiment, we assume that about 4% of the power coupled from the meander to the carrier electrode is reflected back into the structure. Numerical simulations predict that when the back-reflection changes, the position of the magnetic near-field minimum varies.

We test the position dependence by terminating the carrier electrode directly at the SMA feed-through on the vacuum chamber. The transfer π-pulses are then provided by the meander electrode. A fast switch[4] changes the signal path, so either the carrier or the sideband signal is sent to the meander electrode. This is necessary, since the power level for the two transitions differs strongly. We measure the AC Zeeman shift on transition (E) with different termination impedances of the microwave carrier electrode. The corresponding shifts exhibit minima at slightly different positions depending on the termination. To ensure that the minimum is still within the trapping potential, we choose terminations with an impedance

[4] ZASWA-2-50DR+ from Mini-Circuits, Brooklyn, NY, USA

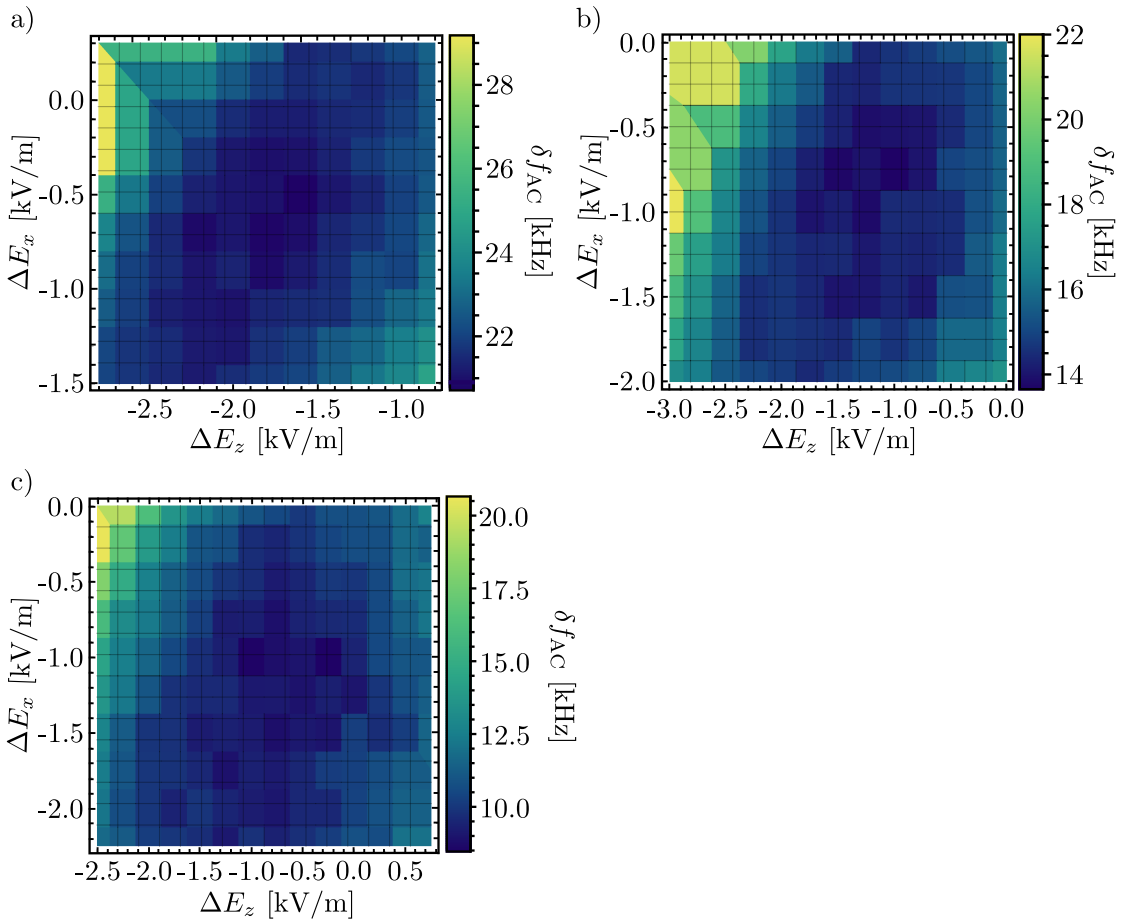

Figure 6.12: AC Zeeman shift δf_{AC} induced by the magnetic field provided by the meander electrode for different termination of the carrier electrode. The shift is given as a function of shim fields ΔE_x and ΔE_z moving the ion in the radial plane. a) is the shift for a 50 Ω termination, whereas b) is for 40 Ω and c) for 30 Ω. The carrier electrode is terminated directly at the feed-through of the vacuum chamber. For these measurements, carrier transitions for the state initialization are provided by the meander structure.

of 50 Ω, 40 Ω and 30 Ω. The resolution is chosen slightly different for these three measurements, since we are only interested in the qualitative behavior. The shifts are given as a function of shim fields relative to the rf null. A close look at the measured data, shown in Figure 6.12, indicates a variation of the position of the minimum. Decreasing the termination shifts the minimum position to the right-hand side and hence closer to the rf null position. Hence, the predicted influence of the back-reflected current on the microwave carrier electrode can also be seen in the experiment. This influence makes it difficult to predict the actual position of the near-field minimum, since the back-reflected current can only be estimated. Enhanced version of the presented trap should reduce this influence by removing the carrier electrode from the trap center. Nevertheless, in the current trap design,

we can use this aspect to our advantage by using it to overlap the electric and magnetic field by adjusting the back reflection. Inserting a switch into the feed line of the carrier electrode and driving it reverse allows for switching between the signal path and a termination. Ideally, this termination is adjustable to tune the back reflection. Double-stub tuners allow to adjust the termination and hence the back reflection. This might be necessary if in the future the trap is used to implement sideband cooling and entangling gates based on sidebands.

6.4 Comparison with simulations

Probing the magnetic near-field using a single ion allows to determine the characteristics of the field provided by a single meander electrode. Fitting the measured AC Zeeman shift of two different transitions to the 2D near-field model (cf. section 3.3) gives the five fit parameters characterizing the field. By comparing the values extracted from the fit with simulations, we are able to validate our numerical simulations. We compare the measured data with the simulated data achieved within the enhanced simulation model, described in section 4.2.5. For the simulation, we assume an electrode thickness of $h = 11\,\mu$m and a gap size of $5\,\mu$m approximated from the fabrication characterization. We further assume that about 4% of the power coupling from the meander to the microwave carrier electrode is back-reflected into the structure. Table 6.1 list the fitting parameters including the position of the near-field minimum for the experimental and the simulation data. The parameters of the simulation depend strongly on the power and the phase of the back reflected current in the microwave carrier electrode. We obtain best agreement for a phase of 110° at the lumped port. The value for the simulated data in Table 6.1 are for that specific phase. As shown in the Table, the agreement between simulation and experiment is at the sub-micron and few-degree level. The fitted and simulated data for both transitions are shown in Figure 6.13. The small deviation in position can be seen as well as the mismatch of the quadrupole orientation.

Table 6.1: Parameters of the microwave near-fields according to the 2D near-field model developed in section 3.3. The parameters are determined from simulations and from experimental measurements of the AC Zeeman shift.

Parameter	Simulation	Experimental data
B/B'	$8.5\,\mu$m	$8.7(1.0)\,\mu$m
ψ	6.4°	4.3(1.2)°
α	24.3°	31.1(3)°
β	99.9°	109.1(11.5)°
x_0	$45.5\,\mu$m	$45.3(1)\,\mu$m
z_0	$-0.8\,\mu$m	$-0.8(2)\,\mu$m

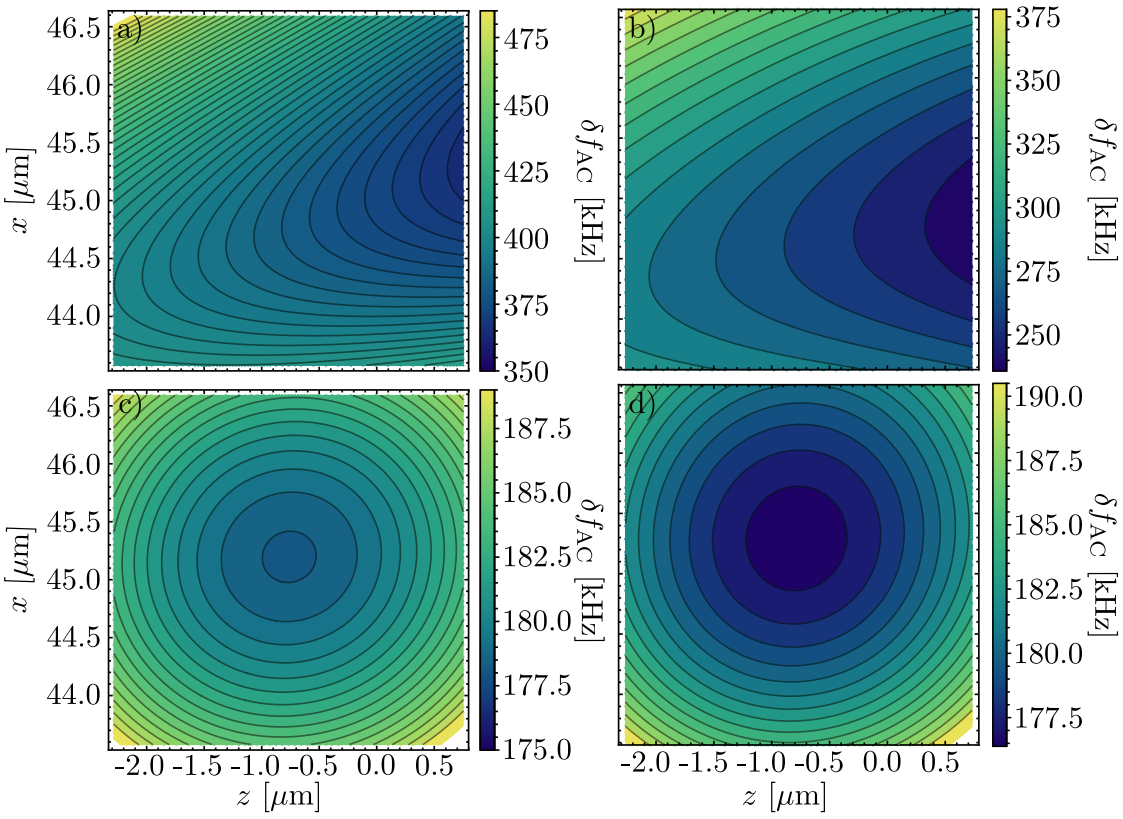

Figure 6.13: Comparison of the fitted and simulated AC Zeeman shift δf_{AC} for both measured transitions. The two rows show the data for $|2,+1\rangle \leftrightarrow |1,+1\rangle$ and $|2,0\rangle \leftrightarrow |1,0\rangle$, respectively. The fitted data is on the left-hand side (a) and c)) and the simulated on the right-hand side (b) and d)). The simulated data is scaled for comparison with the measured data.

The deviation due to the back-reflection and fabrication errors makes an accurate prediction of the position of the field minimum difficult. However, fabrication errors are easier to handle; the variation can be reduced to less than 0.5 μm by optimizing the fabrication process. The deviation in the position is then on the same order. The influence of the back reflection can be reduced by removing the microwave carrier electrode from the trap center. Another issue is the accuracy of the assumed spatial position of the ion as a function of trap voltages. The position is estimated from electrostatic simulations and the pseudopotential approximation. Taking all these effects into account, our enhanced simulation model reflects the measured data with a surprising accuracy. The quality of the prediction has to be tested by designing a successive ion trap with the same simulation model. Ideally, the position in the new design should not depend so strongly on back-reflected currents, which are difficult to estimate.

6.5 Observation of motional sideband transitions

The single meander-shaped electrode designed in chapter 4 is meant to provide the field configuration to induce the spin-motional coupling essential to carry out multi-qubit operations. Even though the magnetic field measurement reveals a rather high residual field, we are able to resolve the corresponding motional sideband frequencies very well. With a frequency of about $2\pi \cdot 11\,\mathrm{MHz}$, the sidebands can be separated from the broad carrier transition as shown in Figure 6.14 for the red sideband transition. This is the fundamental step towards entangling operations in our experiment. The next steps would be to show if we can implement sideband cooling using the meander electrode.

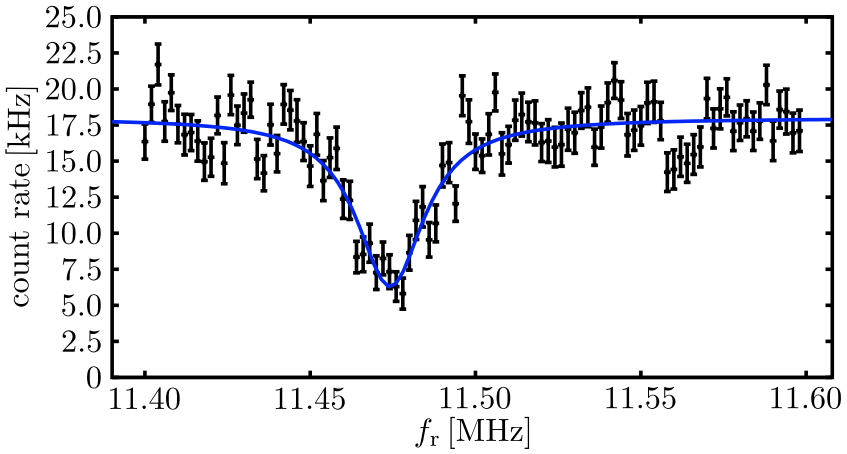

Figure 6.14: The red sideband frequency can easily be resolved at a frequency around 11.5 MHz. The deviation from the measurement in Figure 6.7 occurs due to a slightly different power level of the rf signal.

Chapter 7

Advanced designs for multi-qubit operations

The main goal of this work was to develop a surface-electrode ion trap with a single electrode providing the microwave near-field for multi-qubit operations. To achieve an overlap of the magnetic near-field with the trapping potential by design, a reliable simulation model was essential. The model presented in this work shows an excellent agreement with the experimental data. The next step towards high-fidelity gates is a new trap design optimized for sideband transitions. Based on the obtained results, an enhanced design is developed. Another step to improve the trap design is to integrate the single electrode into multi-layer traps, possibly improving the near-field due to a superior current distribution in the meander and the ground planes. The microwave control can also be improved by embedding the meander into a resonant structure. First results from an improved design are presented here.

7.1 OctoTrap

The ion trap design developed here provides the magnetic near-field configuration for inducing spin-motional coupling with a single microwave electrode, shaped as a meander. The so-called SpyderTrap is the first functional trap with such a simple electrode configuration for integrating the quantum control. However, the main purpose of that design was to validate our simulation model. It was not really optimized for the best performance in the context of motional sideband transitions and quantum logic gates. This is, in fact, only possible now, after taking into account the experimental feedback from the SpyderTrap. The challenge of overlapping the field minimum with the pseudopotential null requires an excellent prediction of both positions. Probing the magnetic field distribution shows that the enhanced model described in section 4.2.5 predicts the position of the magnetic

field minimum reasonably well. Based on these results, one can now attempt to optimize a subsequent ion trap design for sideband transitions by using the optimized parameters in section 4.2.2. By using the enhanced simulation model, the overlap of the electric and magnetic near-field should be possible within a few hundred nanometers, as long as the fabrication errors are reduced to the required level (cf. section 4.2.5). Even though this would lead to a significantly better ratio of sideband to carrier transition Rabi rates, the problem with the back-reflected currents in the microwave carrier electrode is not solved (cf. section 4.2.5). The results obtained in the magnetic near-field measurement as well as the simulations show a strong dependence on the back-reflected current from small impedance mismatches in the microwave carrier electrode feed line. A back-reflection of only 4% of the power transmitted from the microwave meander electrode to the carrier electrode shifts the magnetic near-field minimum by a few microns depending on the phase of that back reflection. Due to the poor predictability of this behaviour, the carrier electrode should be removed entirely from the chip design or moved out of the trapping center. Even though removing the microwave electrode avoids this problem entirely, we consider the latter option since it allows for driving fast carrier transitions independent of the meander electrode. Moving the carrier out of the central trap area does not affect the ability to drive carrier transitions. The resulting changes in the design require a complete analysis of the new geometry. The name of the new chip design is OctoTrap.

In the new trap geometry, the microwave carrier electrode (MWC) is moved out of the central trap area to the edge of the chip. Towards this end, part of the former ground electrode (cf. Figure 4.12) is transformed into a grounded microwave electrode by dividing the ground plane with a small gap, as shown in Figure 7.1. However, removing MWC eliminates the symmetry in the trap center and reduces the amount of available parameters for optimizing the near-field. Previous simulations show that the width in-between the meander segments has the strongest influence on the figure of merit (cf. chapter 4). For a certain value, the figure of merit is maximized. That value differs slightly for different designs. However, these simulations show that the width of that segment corresponding to the optimal figure of merit is below $8\,\mu$m (cf. chapter 4). For example, in the SpyderTrap design it is $6\,\mu$m. The fabrication process developed in this work does not allow for electrode widths below $10\,\mu$m while maintaining an electrode thickness of $h = 10\,\mu$m. However, an improvement of the fabrication process by using a different photo resist allows to set the lower fabrication limit to $8\,\mu$m width electrodes. Hence, we fix the width in-between the meander segments to $w_{\mathrm{RF}_1} = w_{\mathrm{GND}_1} = 8\,\mu$m to obtain the best figure of merit possible within the fabrication constraints. This unfortunately yields a significant problem. Only two parameters, w_{MW} and w_{RF_2}, are available to overlap the quadrupole fields and these parameters change the height of the magnetic near-field minimum and the ion-to-surface distance nearly equally. This does not allow for an overlap of both

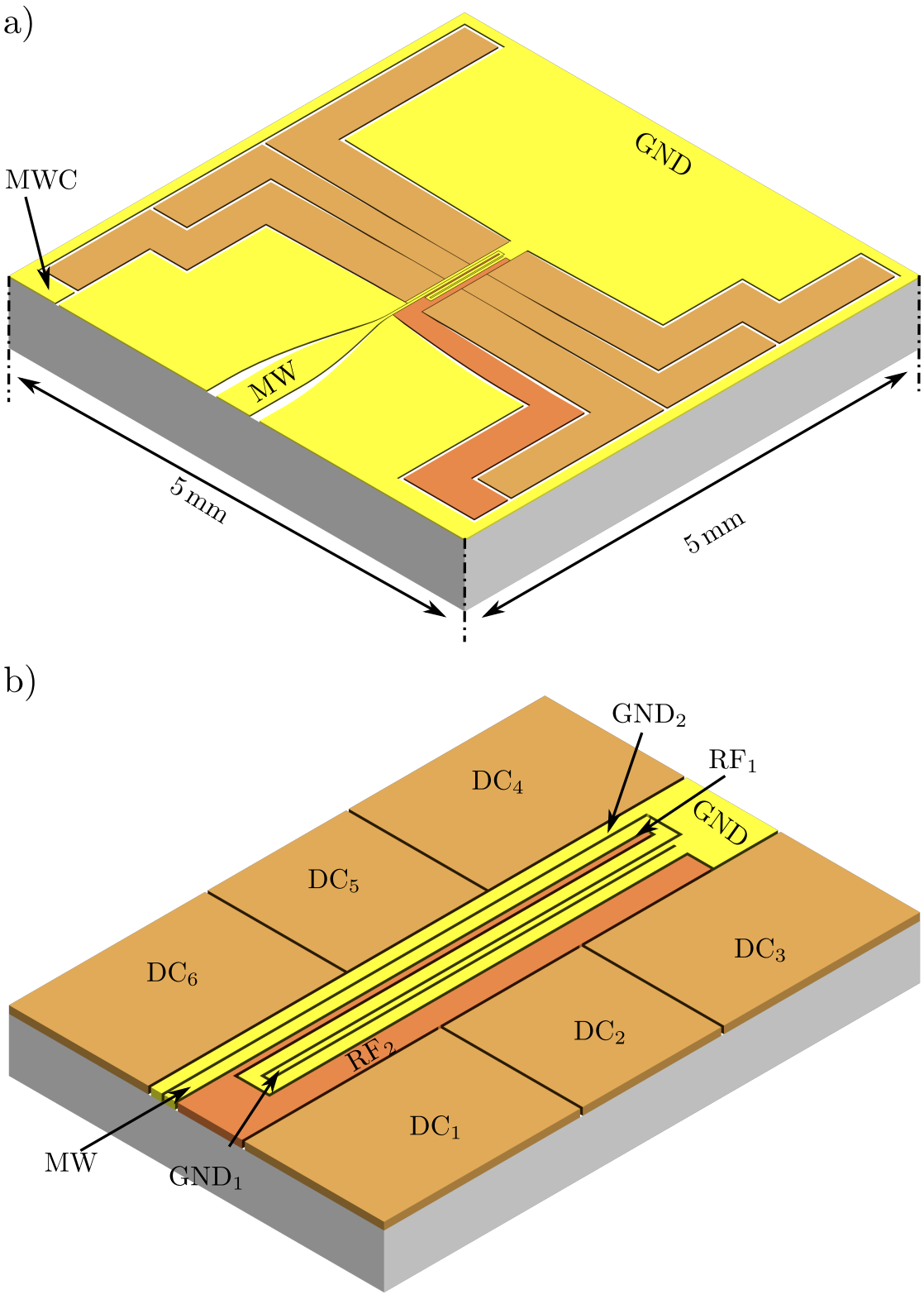

Figure 7.1: Design of an improved version of the SpyderTrap. In the so-called OctoTrap the microwave carrier electrode (MWC) is moved to the edge of the chip. To achieve an overlap of the electric and magnetic field quadrupole, an additional ground segment GND_2 is inserted in the design, shown in b).

quadrupole fields. A first parametric sweep reveals a minimum distance between the field minimum and the ion's position in the x-direction of about $3\,\mu$m. None of the available parameters can be adjusted sufficiently to compensate for that distance. Also, slightly increasing w_{RF_1} and/or w_{GND_1} does not significantly improve the overlap. Only changing the electrode thickness by about a factor of two could lead to an overlap of the fields. Although the improved fabrication process increases the aspect ratio of electrode width to thickness to about $1:2$, more than $15\,\mu$m cannot be fabricated reliably for electrode widths of $8\,\mu$m. Hence, an overlap in this design is not feasible. To overcome this issue, the symmetric design in the trap center is re-established. The former carrier electrode is now part of the ground plane. Simulation results reveal a better figure of merit by cutting the ground on one side of the central trap area (see Figure 7.1 a)). Adding an additional ground part restores the symmetry and more importantly decreases the height of the field minimum. Furthermore, adjusting the width of that electrode and the width w_{RF_2} independently enables an overlap of the fields. The final design is obtained by determining the height of the magnetic near-field minimum based on the width of the meander electrode and subsequent adjustment of w_{RF_2} and w_{GND_2}. The latter changes mainly the position of the field minimum; it does not influence the rf potential. w_{RF_2} is optimized to obtain an overlap in the z-direction. Slightly adjusting the thickness of the electrodes yields a simulated overlap within a few 100 nm. We have, however, not considered the influence of back-reflected currents on the re-designed carrier electrode yet to see if the redesign holds its promise.

In the validation of the enhanced model, we have assumed that the back-reflection amounts to 4% of the power coupled from the meander to the microwave carrier electrode. This assumption lead to an excellent agreement of simulation and measurement if the phase of that current is chosen appropriately (cf. section 6.4). Although the assumption is reasonable, the simulation model might still have slight deviations in the prediction of the position since the amplitude and phase of the back-reflected current are only estimated. Small deviations from that value lead to a significant change in position (cf. section 4.2.5). Moving the microwave carrier electrode out of the trap center to the edge of the chip reduces this influence significantly. Here, the position changes by less than $0.3\,\mu$m, assuming a current on MWC which has 1% of the power coupled to the meander. Compared to the SpyderTrap, this deviation is reduced by one order of magnitude (cf. Figure 4.21). This is mainly due to the fact that for the same nominal current on the carrier electrode, the magnetic field seen by the ion is substantially smaller than for the SpyderTrap. Moreover, the coupling between the microwave electrodes is slightly decreased, which leads to an additional factor of two in power. In total, the influence of a back-reflected signal on the microwave carrier electrode is reduced to the same level as the influence of errors in the fabrication process. Probing the near-field of the OctoTrap will give more insight about the accuracy of the simulation model.

7.2 Multi-layer traps

Multi-layer traps have a high potential for scaling up the architecture of a simple ion trap to a quantum information processor, as discussed in [28]. Although the fabrication is difficult, these traps are necessary for large-scale devices required for quantum simulation and quantum information. Multiple metal layers extend the possibilities for arranging the different electrodes for trapping and controlling ions [123]. Having multiple layers enables an improved design for the integrated microwave approach by using the lowest layer solely for delivering microwave signals to the trap center. For the single-electrode design, it can further reduce the residual field by placing the turning segments S_4 and S_5 (cf. Figure 4.2) in the lowest layer and the other parallel segment in the upper layer. The basic idea is illustrated in Figure 7.2 for a single-site ion trap. The modified current distribution in the multi-layer structure should improve the figure of merit due to a reduced residual field. Furthermore, implementing the single microwave electrode design in a scalable architecture is only possible with multiple layers; in a single layer, the rf potential is always interrupted at the turning points of the meander. In a first step, we investigate a three-layer design. Here, only the microwave feed line and the ground plane are in the lowest layer. All trapping electrodes are in the top layer. This simplifies the fabrication process.

Fabrication

There are several approaches of fabricating multi-layer ion and atom chips [124, 101, 125, 126, 127]. In a first attempt, we develop a fabrication process which extends our single-layer fabrication. The general idea is to grow each metal layer using the electroplating process for the single layer and use polyamide as an insulation layer between the first and third layer. Chemical mechanical polishing (CMP) can be used to planarize the polyamide enabling a smooth top layer. Figure 7.3 shows the first results of fabricating the multi-layer ion trap in the PTB clean room facility. The lowest layer is grown on a silicon substrate with high resistivity ($10\,\mathrm{k\Omega\,m}$) with an additional insulation layer of silicon nitride (SiN). The individual steps are similar to those for a single-layer, but they differ due to a different choice of photo resist. The second layer, mostly consisting of vias, is grown with the same process onto the first layer, repeating all of the steps. The next step is to spin on and planarize polyamide filling the gaps in the first layer and creating the insulation layer. The third layer is then grown onto that insulation. To start the electroplating process for the last layer, gold and an adhesion metal must be evaporated on the polyamide layer. In a last step, we plan to etch the polyamide in the gaps to reach high aspect ratio for the electrode heights. This reduces the effect of electric stray fields due to accumulated charges on the dielectric substrate.

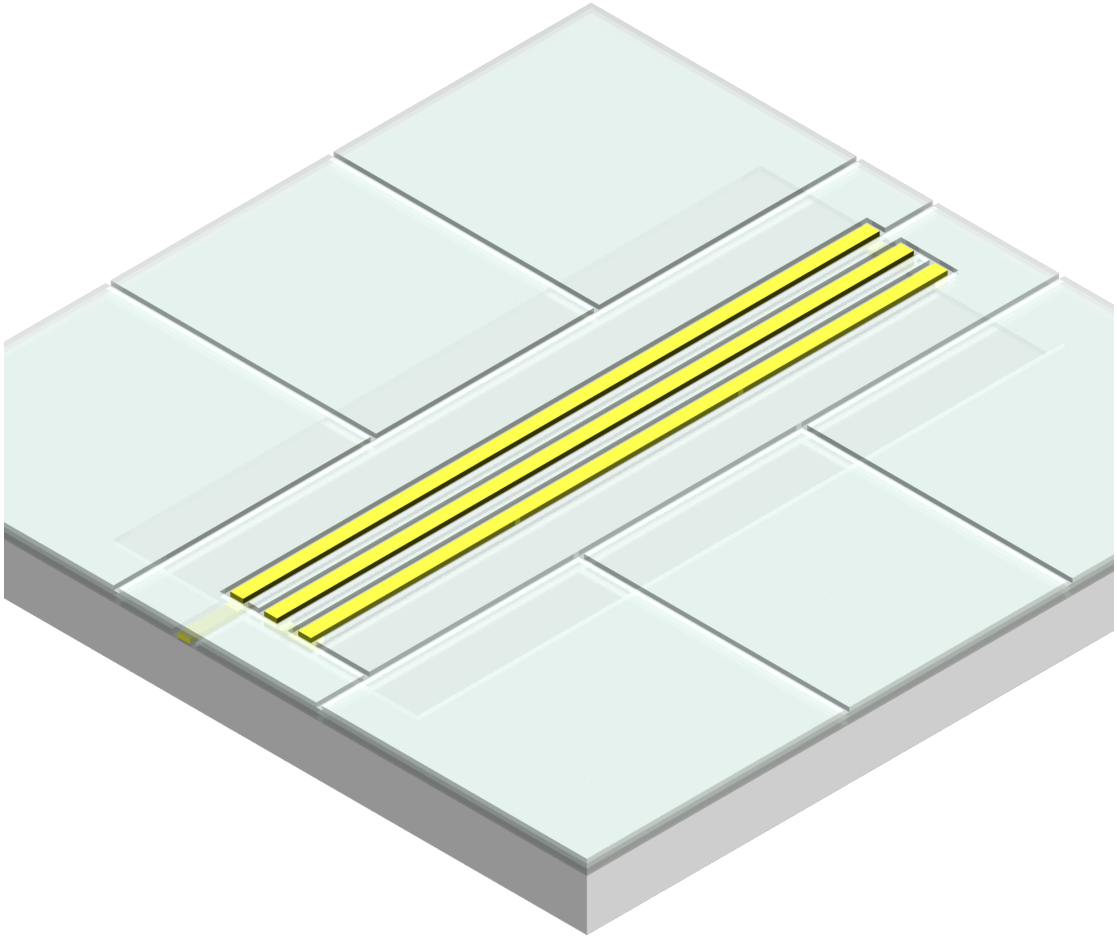

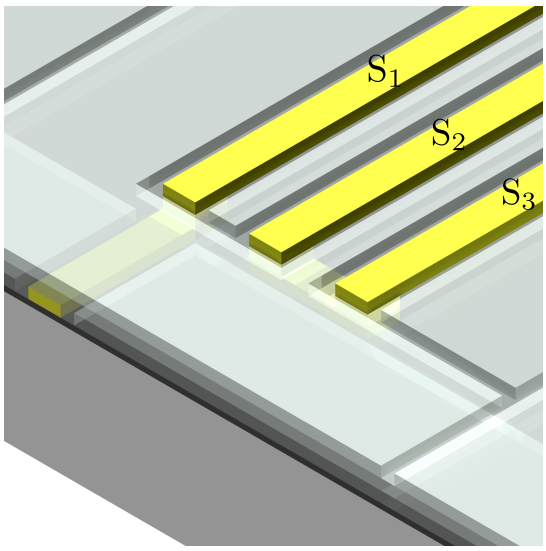

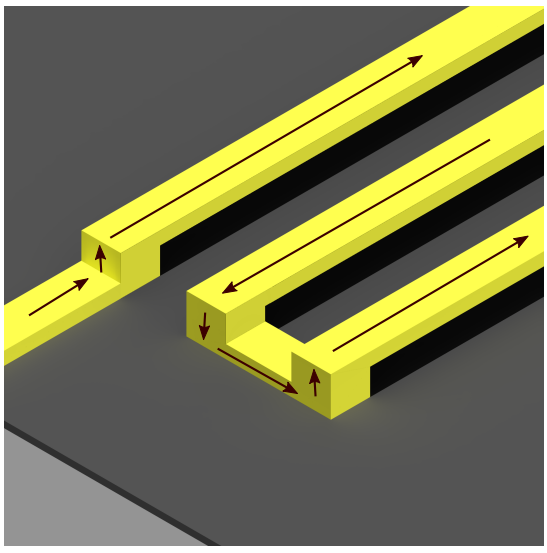

Figure 7.2: Multi-layer design for a surface-electrode ion trap with a single trapping zone and a single microwave electrode providing the near-field used to induce spin-motional coupling. The microwave electrode is highlighted in yellow. The feed line of the meander is in the lowest layer, whereas the parallel segments S_{1-3} are in the upper layer. To reduce magnetic near-field in axial direction, the turning elements are placed in the lowest layer; vias connect the upper and lower layer. Arrows indicate the current flow direction in the meander electrode.

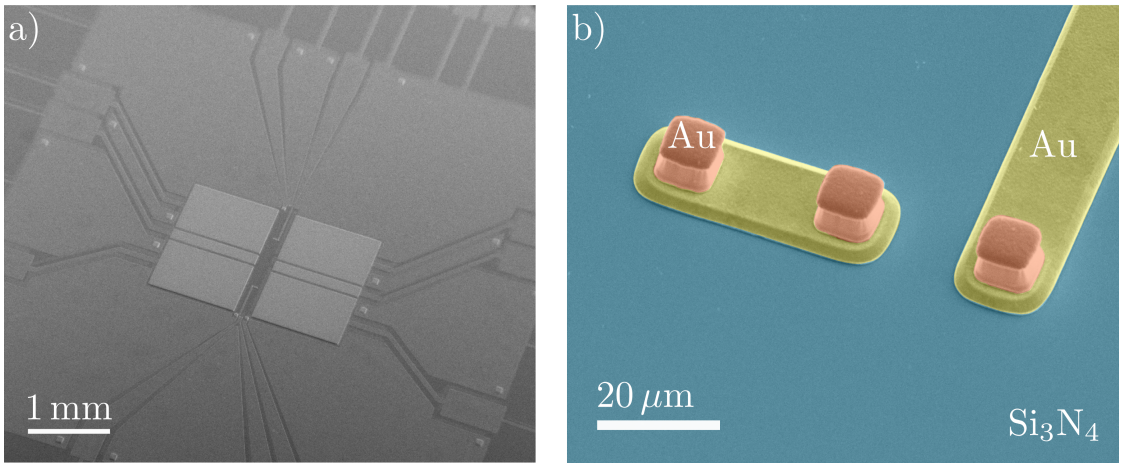

Figure 7.3: First fabrication results towards a multi-layer design. a) shows a scanning electron microscope (SEM) image from a $5 \times 5\,\mathrm{mm}^2$ ion trap chip. The two layers shown are grown using electroplating. In the zoom-in (b) the shape of the lower layer and the vias are shown. We grow the gold electrodes (Au) on silicon substrate with a Si_3N_4 insulation layer. The image is artificially coloured for clarification. SEM images are taken by Peter Hinze at the PTB clean room facility.

First simulation results

In a first simulation run, we investigate whether the proposed meander design improves the ratio of sideband to carrier transition Rabi rates (cf. Eq. (4.1)). A complete chip design is considered for the investigation. We sweep the electrode sizes in the trap center including the heights of the individual layers. Optimizing all parameters leads to a maximum figure of merit $\eta \approx 0.15$. The sweep of the parameter with the strongest influence is shown in Figure 7.4 a). For comparison, Figure 7.4 b) shows the sweep of the same parameter for the single-layer design. Although the latter reaches a better ratio of sideband to carrier transition Rabi rats, which is described by the figure of merit, the multi-layer design is advantageous. As mentioned before and discussed in section 4.1.1, the fabrication limit for the electrode width is $8\,\mu\mathrm{m}$. As a result, the optimal value for the single layer design cannot be achieved and the best ratio decreases from $\eta \approx 0.24$ to $\eta \approx 0.05$. The most interesting fact arising from using multi-layers is that the changed current distribution shifts the optimal electrode size from $w_{RF_1} = 6\,\mu\mathrm{m}$ for the single-electrode design to $w_{RF_1} = 10\,\mu\mathrm{m}$, which lies inside our fabrication range. Under these constraints, multi-layer designs are significantly better regarding efficient sideband transitions. A figure of merit three times higher can be reached. Nevertheless, the comparison was done without accounting for boundary conditions for the electrodes, and without overlapping the near-field minimum with the ion's position. To obtain a decent design, a complete simulation run including boundaries and an optimization of the aforementioned overlap has to be performed.

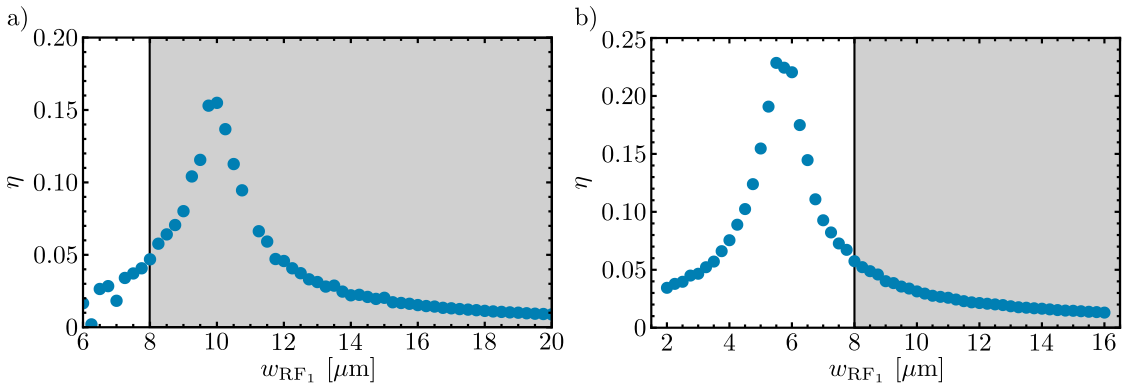

Figure 7.4: Comparison of multi- and single-layer ion trap design. After optimizing the geometry, the parameter with the most influence w_{RF_1} is swept around the optimal electrode size for both designs. a) shows the data for the multi-layer design and b) the data for the single-layer design. In general, the single-layer design reaches higher value for the figure of merit η. However, taking fabrication limits into account, the best figure of merit is reached with the multi-layer design since the lower limit for the electrode size is 8 μm. The grey area indicates feasible electrode widths.

7.3 Impedance matching

The surface-electrode ion trap developed in this work provides the microwave near-field configuration essential for multi-qubit operations through a single microwave electrode integrated into the trap design. That single electrode is grounded as close as possible to the trap center to eliminate any phase differences between the applied and the back-reflected microwave signals. The S-parameter measurement shows that at a frequency of 1082.55 MHz approximately 90% of the power is back-reflected towards the amplifier. To reduce the power loss, the microwave electrode and hence the ion trap can be embedded into a resonant structure. That structure is either realized with a half- or quarter-wave resonator [69] or using an impedance matching network. Due to the enhancement of the current in such a structure, we reach significantly higher current and thus field gradients for the same input power. With impedance-matched networks it is possible to build a resonant structure around the ion trap with lumped elements in such a way that almost the complete applied power is transmitted into the trap. In a NTH[1] project, first attempts to design such a network based on lumped elements have been investigated in cooperation with the TU Braunschweig. An interdigital gap capacitor embedded in the feed line is able to form a resonant structure with the grounded meander electrode in the ion trap, as shown in Figure 7.5. Carefully designing this capacitor yields a resonance at the qubit transition frequency for the combined system. The bandwidth of this resonance should be at least 30 MHz to account for sideband frequencies.

[1] Niedersächsische Technische Hochschule

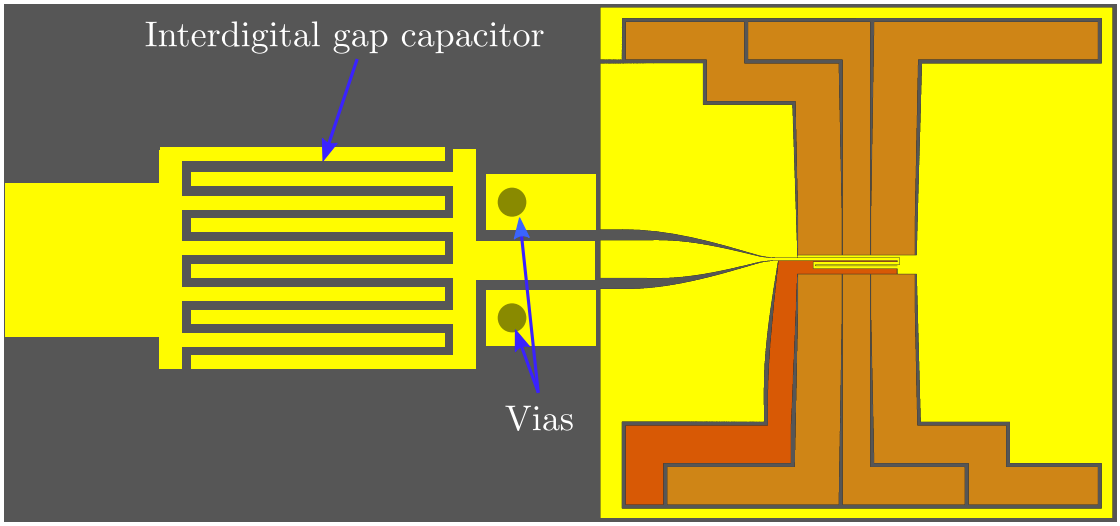

Figure 7.5: Impedance matching for an ion trap with a single microwave electrode. Embedding an interdigital gap capacitor in the feedline of the meander electrode allows for building a resonant structure with which the current in the ion trap can be enhanced. Vias connect the ground of the feed line to an underlying ground plane.

Chapter 8

Conclusion

The work presented in this thesis focuses on the integration of a single microwave electrode into the design of a surface-electrode ion trap. That electrode induces spin-motional couplings necessary to implement multi-qubit operations. The near-field approach requires a small field amplitude and a high gradient to induce such a coupling. First numerical simulations show that a single meander-shaped electrode is able to provide such a field configuration. The field amplitude is minimized for a certain geometric arrangement. To compare the near-field patterns from simulations and measurements, a 2D microwave near-field model characterizing the field pattern was developed. Our model fully describes the properties of a magnetic field near a local minimum through five parameters. These parameters characterize the strength and orientation of the residual field at the minimum as well as of the gradient. The fifth parameter describes the phase between the real and imaginary part of the field and hence the polarization. This model is the basis of the fitting procedure used for numerical and simulated data.

Numerical simulations are essential for designing ion traps with integrated microwave quantum control structures, since the electrodes are embedded in the trap structure and the qubit splitting is typically in the GHz regime. At such high frequencies, the proximity and skin effect play a significant role. State-of-the-art numerical simulation account for both effects and allow for an accurate determination of the field configuration. Several simulation models describing the trap design in different stages have been developed. All simulations presented were performed for the transition frequency of a first-order field-insensitive transition in the hyperfine manifold in the ground state of $^9Be^+$. This transition occurs at a 22.3 mT bias field between the energy levels $|F = 2, m_F = +2\rangle$ and $|F = 2, m_F = +1\rangle$, which are defined as the qubit states.

The surface-electrode ion trap design requires an overlap of the magnetic near-field minimum and the position of rf pseudopotential null by design. An additional

microwave electrode was inserted into the design to drive fast carrier transitions. To precisely determine the position of the magnetic near-field, it was necessary to include the boundary conditions for each electrode. These conditions needed to reflect the settings in the experimental setup. Due to a simplified assumption for the boundary conditions applied to the electrode, the overlap of the magnetic quadrupole field and the trapping potential in the final calibration trap, the SpyderTrap, deviates by a few microns. However, an improved model including ports for the microwave carrier electrode and rf electrodes reflected the actual experimental settings in a reasonable way. This model shows that the magnetic near-field is extremely sensitive to small back-reflected currents coming from the microwave carrier electrode. In particular, the position depends on this current, complicating an overlap of the magnetic near-field and the ion's position. To reduce this dependence, the microwave carrier electrode should be removed or moved away from of the central trap area in a subsequent design. The design of the OctoTrap is an optimized chip geometry, in which the microwave carrier electrode is moved away from the central trap area. The effect of the back-reflection is here reduced to the level of fabrication errors.

To determine how precisely the field configuration can be predicted with numerical simulations, the magnetic near-field distribution provided by the meander was measured. A single $^{9}Be^{+}$ ion served as a high-resolution quantum sensor to measure the magnetic field distribution through energy shifts induced in the hyperfine structure of the ground state. By shifting the ion in the radiofrequency potential using small electrostatic shim fields, the magnetic field within the trapping potential was measured radially. The resolution of the positioning is a few tens of nanometers. The apparatus to perform this measurement and succeeding experiments was set up during this work. One neat feature of this apparatus is the ability to load an ion with a single nanosecond pulse by ablation loading. The measured magnetic near-field agrees on the sub-micron and few-degree level with the simulation. For the simulation, we assumed that 4% of the power coupled from the meander to the microwave carrier electrode is back reflected into the structure. By changing the termination of the carrier electrode outside of the vacuum chamber, the magnetic near-field minimum was shifted towards the rf pseudopotential null. This dependence can be used as a feature with the present trap, however it should be avoided in the subsequent designs, to prevent fluctuating currents that degrade the stability of the magnetic field.

The results obtained in this thesis will inspire the design of new structures for microwave quantum logic applications used for quantum simulation and quantum information processing. Ideally, future designs would be based on a multi-layer structure, so that signals could be delivered in layers underneath the structure via embedded waveguides and only brought to the surface close to the ion. This would decouple the design of near-field structures from other trap modules in a scalable trap array. First attempts towards a multi-layer ion trap are presented in this work.

Appendix A

Commutator relations

Here, I will follow a description developed by C. E. Langer and C. Ospelkaus while at NIST.

To transform the equation of the interaction of the qubit with an oscillating field, we use the Baker-Campbell-Hausdorff formula with additional commutator relations. Assuming two linear operators $\mathbf{A}$ and $\mathbf{B}$

$$\begin{aligned} \mathbf{B}_n := [\mathbf{A},\mathbf{B}]_n &:= \left[\mathbf{A},[\mathbf{A},\mathbf{B}]_{n-1}\right] \\ \mathbf{B}_0 &:= \mathbf{B} \quad , \end{aligned}$$

the Baker-Campbell-Hausdorff formula is given by

$$e^{\tau\mathbf{A}}\mathbf{B}e^{-\tau\mathbf{A}} = \sum_n \frac{\tau^n}{n!}\mathbf{B}_n. \tag{A.1}$$

In the following, the steps to transform Equation (3.16) into the form of Equation (3.17) are shown. As a reminder, the interaction picture Hamiltonian is given by

$$\begin{aligned} \mathbf{H}'_B &= e^{\frac{i\mathbf{H}_0}{\hbar}t}\mathbf{H}_B e^{-\frac{i\mathbf{H}_0}{\hbar}t} \\ &= 2\hbar\cos(\omega t+\varphi) \\ &\quad \times e^{\frac{i\mathbf{H}_{\text{int}}}{\hbar}t}(\boldsymbol{\sigma}_+ + \boldsymbol{\sigma}_-)e^{-\frac{i\mathbf{H}_{\text{int}}}{\hbar}t} \\ &\quad \times \sum_k \frac{\Omega_k}{k!} e^{\frac{i\mathbf{H}_{\text{trap}}}{\hbar}t}(\mathbf{a}+\mathbf{a}^\dagger)^k e^{-\frac{i\mathbf{H}_{\text{trap}}}{\hbar}t}. \end{aligned}$$

For the interaction with the internal part

$$e^{\frac{i\omega_0 t}{2}\boldsymbol{\sigma}_z}(\boldsymbol{\sigma}_+ + \boldsymbol{\sigma}_-)e^{-\frac{i\omega_0 t}{2}\boldsymbol{\sigma}_z}$$

the linear operators are $\mathbf{A} := \boldsymbol{\sigma}_z$ and $\mathbf{B} := \boldsymbol{\sigma}_+ + \boldsymbol{\sigma}_-$, and $\tau := i\omega_0 t/2$. With the commutator relations

$$\begin{aligned}
[\boldsymbol{\sigma}_z, \boldsymbol{\sigma}_+ + \boldsymbol{\sigma}_-] &= [\boldsymbol{\sigma}_z, \boldsymbol{\sigma}_x] \\
&= 2i\boldsymbol{\sigma}_y \\
&= 2(\boldsymbol{\sigma}_+ - \boldsymbol{\sigma}_-) \\
[\boldsymbol{\sigma}_z, 2(\boldsymbol{\sigma}_+ - \boldsymbol{\sigma}_-)] &= [\boldsymbol{\sigma}_z, 2i\boldsymbol{\sigma}_y] \\
&= 4\boldsymbol{\sigma}_x \\
&= 4(\boldsymbol{\sigma}_+ + \boldsymbol{\sigma}_-)
\end{aligned}$$

we can set $\mathbf{B}_n = 2^n\boldsymbol{\sigma}_+ + (-2)^n\boldsymbol{\sigma}_-$. Applying Equation (A.1) leads to

$$\begin{aligned}
e^{\frac{i\mathbf{H}_{\text{int}}}{\hbar}t}(\boldsymbol{\sigma}_+ + \boldsymbol{\sigma}_-)e^{-\frac{i\mathbf{H}_{\text{int}}}{\hbar}t} &= \sum_n \frac{(i\omega_0 t/2)^n}{n!}\left(2^n\boldsymbol{\sigma}_+ + (-2)^n\boldsymbol{\sigma}_-\right) &\text{(A.2)} \\
&= \boldsymbol{\sigma}_+ e^{i\omega_0 t} + \boldsymbol{\sigma}_- e^{-i\omega_0 t}. &\text{(A.3)}
\end{aligned}$$

Using $e^{\frac{i\mathbf{H}_{\text{trap}}}{\hbar}t}e^{-\frac{i\mathbf{H}_{\text{trap}}}{\hbar}t} = 1$, the interaction with $\mathbf{H}_{\text{trap}}$ can be written as:

$$\begin{aligned}
&\sum_k \frac{\Omega_k}{k!} e^{i\omega_z t(\mathbf{a}^\dagger\mathbf{a})}(\mathbf{a} + \mathbf{a}^\dagger)^k e^{-i\omega_z t(\mathbf{a}^\dagger\mathbf{a})} \\
= &\sum_k \frac{\Omega_k}{k!}\left[e^{i\omega_z t(\mathbf{a}^\dagger\mathbf{a})}(\mathbf{a} + \mathbf{a}^\dagger)e^{-i\omega_z t(\mathbf{a}^\dagger\mathbf{a})}\right]^k. &\text{(A.4)}
\end{aligned}$$

Here, we treat the expression in the square brackets by expanding it into a sum of two terms, one with $\mathbf{a}$ and one with $\mathbf{a}^\dagger$, and then apply Eq. (A.1) individually for those terms. The linear operators are then $\mathbf{A} := \mathbf{a}^\dagger\mathbf{a}$ and $\mathbf{B} := \mathbf{a}$ with $\mathbf{B}_n = (-1)^n\mathbf{a}$ and $\mathbf{A} := \mathbf{a}^\dagger\mathbf{a}$ and $\mathbf{B} := \mathbf{a}^\dagger$ with $\mathbf{B}_n = \mathbf{a}^\dagger$. We obtain the relation for the corresponding $\mathbf{B}_n$ due to

$$\begin{aligned}
\left[\mathbf{a}^\dagger\mathbf{a}, \mathbf{a}\right] &= \mathbf{a}^\dagger\mathbf{a}\mathbf{a} - \mathbf{a}\mathbf{a}^\dagger\mathbf{a} \\
&= \left(\mathbf{a}^\dagger\mathbf{a} - \mathbf{a}\mathbf{a}^\dagger\right)\mathbf{a} \\
&= -\left[\mathbf{a}, \mathbf{a}^\dagger\right]\mathbf{a} \\
&= -\mathbf{a}
\end{aligned}$$

and

$$\begin{aligned}
\left[\mathbf{a}^\dagger\mathbf{a}, \mathbf{a}^\dagger\right] &= \mathbf{a}^\dagger\mathbf{a}\mathbf{a}^\dagger - \mathbf{a}^\dagger\mathbf{a}^\dagger\mathbf{a} \\
&= \mathbf{a}^\dagger\left(\mathbf{a}\mathbf{a}^\dagger - \mathbf{a}^\dagger\mathbf{a}\right) \\
&= \mathbf{a}^\dagger\left[\mathbf{a}, \mathbf{a}^\dagger\right] \\
&= \mathbf{a}^\dagger.
\end{aligned}$$

Applying Equation (A.1), Equation (A.4) becomes

$$\begin{aligned} & \sum_k \frac{\Omega_k}{k!} \left(e^{i\omega_z t(\mathbf{a}^\dagger \mathbf{a})} (\mathbf{a} + \mathbf{a}^\dagger) e^{-i\omega_z t(\mathbf{a}^\dagger \mathbf{a})} \right)^k \\ = & \sum_k \frac{\Omega_k}{k!} \left(\sum_n \frac{i\omega_z t}{n!} \left((-1)^n \mathbf{a} + \mathbf{a}^\dagger \right) \right) \\ = & \sum_k \frac{\Omega_k}{k!} \left(e^{-i\omega_z t} \mathbf{a} + e^{i\omega_z t} \mathbf{a}^\dagger \right) \end{aligned} \tag{A.5}$$

The complete Hamiltonian in interaction picture is then (Eq. (3.17)):

$$\mathbf{H}'_B = \hbar \left(e^{i(\omega t + \varphi)} + e^{-i(\omega t + \varphi)} \right) \left(\boldsymbol{\sigma}_+ e^{i\omega_0 t} + \boldsymbol{\sigma}_- e^{-i\omega_0 t} \right) \sum_k \frac{\Omega_k}{k!} \left(e^{-i\omega_z t} \mathbf{a} + e^{i\omega_z t} \mathbf{a}^\dagger \right)^k .$$

Appendix B

Microfabrication recipe

Our ion trap fabrication process is based on Philipp Treutlein's recipe for atom chips [101]. Because we applied several parameter changes to achieve thicker electrode structures, a detailed recipe for the microfabrication process at the PTB clean-room facility is described here. If used in a different clean room, an adjustment of the process parameters is necessary. In particular, the lithography parameters might change significantly, mainly due to different levels of humidity. The recipe is divided into the following fabrication steps.

- Deposition of adhesion (Ti) and seed layer (Au)
- Optical lithography
- Electroplating
- Etching
- Dicing

Deposition of adhesion and seed layer

We use a home-made evaporation chamber to deposit the seed and adhesion layer. The so-called CongoVac evaporator is a resistive thermal evaporator with a two boat system. Hence, both materials can be deposited consecutively without opening the vacuum chamber. The CongoVac evaporator reaches pressures on the order of 10^{-6} mbar during the process, sufficient for our purposes.

1. Vent vacuum chamber.
2. Cleaning procedure of AlN wafer.

   (a) 5 min acetone in a ultra sonic bath (USB), blow dry.
   (b) 5 min isopropanol in a USB, spin dry thoroughly.
   (c) 5 min at 200 W in oxygen plasma (1.2 mbar).
3. Mount thermal boat for gold and titanium.
   (a) If necessary refill titanium and/or gold.
4. Mount wafer in CongoVac chamber without delay and close shutter.
5. Evacuate chamber and wait until a pressure of 10^{-6} mbar is reached.
6. Deposition
   (a) Program evaporator for titanium and turn on current.
   (b) Wait until evaporation starts and titanium starts gettering.
   (c) Open shutter and deposit 2 nm Ti with a rate of 0.1 nm/s.
   (d) Close shutter and switch current supply to gold thermal boat.
   (e) Program evaporator for gold and turn on current.
   (f) Wait till evaporation starts and a stable pressure is reached.
   (g) Open shutter and deposit 50 nm gold with a rate of 0.2 nm/s.
7. Remove all items and evacuate chamber to ensure a clean environment for successive operations.

Optical lithography

Lithography is usually done directly after evaporation. If this is not possible and the coated wafer is stored for a short time, the cleaning procedure described above is repeated. The lithography steps are divided into spinning on the resist, pre-bake, exposure and development. We spin on the resist with a standard spin coater in a two-step process to reduce a possible edge bead. After the coating, a relaxation step is included to avoid any defects coming from outgassing in the resist film. For thin films, this is not necessary. A pre-bake stabilizes the resist and prevents sticking of the resist to the mask. The following waiting period is used to rehydrate the resist. Without this step, the development time might be increased significantly; furthermore, steep edges cannot be achieved. The exposure is done with a MA6 Mask aligner. With our thick film resist, we can achieve a line resolution of roughly 4 μm for an electrode thickness of 10 μm. Smaller structure cannot be resolved in our process.

1. Spin on resist

(a) Heat wafer for 5 minutes on a hotplate at 100 °C.

(b) Place wafer centered onto the spin coater chuck.

(c) Dispense 2.5 ml of ma-P 1275 resist carefully on the surface.

(d) Avoid or rather remove any bubbles in the resist.

(e) Spin on the resist for 30 s at 1800 rpm, then 5 s at 3000 rpm

(f) Final film thickness: 10 μm.

2. Pre-bake and waiting times.

(a) Let the resist relax for 10 min

(b) Pre-bake wafer 10 min at 100 °C on a hotplate (likewise 90 °C for 12 min).

(c) Let the wafer rehydrate for 15 min

3. Exposure

(a) Place mask into mask holder and fix it.

(b) Place wafer carefully onto wafer chuck.

(c) Use low vacuum mode for exposure.

(d) Expose wafer for 35 s to reach an exposure dose of 420 mJ/cm^2.

4. Development

(a) Develop resist in ma-D 331 developer for 80 s. Move wafer the whole time.

(b) Stop development in a water bath.

(c) Rinse thoroughly with water.

(d) Spin the wafer dry.

(e) Inspect wafer with an optical microscope and potentially continue development.

5. Clean mask

(a) 30 min in acetone in a USB, blow dry.

(b) 10 min in isopropanol in a USB, blow dry thoroughly.

Electroplating

During the electroplating, the wafer is moved up and down linearly with an electric motor. The rotation is transferred into a linear movement due to the construction. The speed should be on the order of a few 10 rpm. To avoid high voltages we include a series resistance of 100 Ω in the electrical path.

1. Preparation
   (a) Heat electroplating water bath for 2 h.
   (b) Put gold bath[1] into water beaker. Wait another $30 - 45$ min until a stable temperature of 58 °C is reached.
   (c) Remove resist residues in gaps in oxygen plasma (60 s, 60 Watts, 1.2 mbar)
   (d) Mount and contact wafer.
   (e) Rinse with water to avoid air bubbles on the surface.
   (f) Place wafer on holder into gold bath and connect the holder to the electrical motor.
   (g) Connect electric motor to power supply, turn on at 3.5 V.
   (h) Wait a few minutes until the temperature is stable again.
   (i) Connect anode and wafer to a power supply. Turn on power supply with 0 V.
2. Electroplating process
   (a) Try to avoid any voltage peaks while slowly turning on voltage to 9.2 V, corresponding to a current of 84.4 mA for a 100 Ω resistance.
   (b) Agitate solution with magnetic stirrer at 600 rpm.
   (c) Electroplate the whole 3 inch wafer in 75 min with a rate of 2.2 nm/s to a thickness of 10 μm.
3. After Electroplating
   (a) Slowly turn off current and electrical motor
   (b) Immediately place wafer into a water bath, wait a couple of minutes
   (c) Demount wafer from holder
   (d) Rinse with DI water thoroughly, at least 5 min
   (e) Spin dry
   (f) Rinse equipment with water and filter gold solution.

[1] Gold-SF solution from METAKEM GmbH, Usingen, Germany

Etching

In the etching process, we use two chemicals, Piranha etch and Aqua regia. The former removes residual resist and slowly etches titanium. The latter etches the gold seed layer. The chemical composition of Piranha is H_2SO_4:H_2O_2, in general used in the ratio 3 : 1 and 4 : 1. In big quantities, the solution can explode. We mix piranha in small amounts (40 ml : 10 ml). It can be used for roughly 10 min. The etching rate of piranha for titanium is 240 nm/min.

Aqua regia is mixed out of H_2O:HCl(30%):HNO_3(65%) in a ratio 1 : 3 : 1. The ordering of mixing is from left to right. Aqua regia reaches an etching rate for gold of 680 nm/min.

1. Remove resist
   (a) 5 min acetone in a USB, blow dry
   (b) 5 min isopropanol in a USB, spin dry thoroughly
2. Clean with fresh piranha etch
   (a) Agitate for 60 s
   (b) Place in water bath for a couple of minutes, rinse thoroughly with water, blow dry.
3. Etch gold seed layer (50 nm)
   (a) Place wafer for 40 s in aqua regia and pivot the beaker.
   (b) Place in water bath for a couple of minutes, rinse thoroughly with water, blow dry
4. Etch titanium adhesion layer (2 nm)
   (a) Place wafer in piranha and pivot the beaker until AlN clears up (30 s).
   (b) Place in water bath for a couple of minutes, rinse thoroughly with water, blow dry
5. Cover with protection resist after characterizing the wafer.

Dicing

The wafer is diced using a diamond blade P1A Mesch 400 with a width of 150 μm in a standard wafer saw. To avoid cracks we dice only three-quarter through the substrate. We can then easily divide the individual traps by carefully breaking the wafer along the dicing lines. An additional lamination foil stabilizes the wafer during the dicing process. The protection resist is removed using the standard

cleaning procedure with an additional etching step for 60 s. Piranha etch removes the remaining resist in the gaps.

One possibility to improve the electroplating process concerning the homogeneity of the gold thickness is to use smaller substrates or to quarter the wafer. The latter can be done by dicing only half through the wafer from the backside before the first coating. We tested this approach. However, the stability of the wafer is reduced and might break apart during the process.

Bibliography

[1] Seth Lloyd.
Universal Quantum Simulators.
Science, 273(5278):1073 –1078, 1996.
DOI: 10.1126/science.273.5278.1073.

[2] Richard P. Feynman.
Simulating physics with computers.
International Journal of Theoretical Physics, 21(6-7):467–488, June 1982.
DOI: 10.1007/BF02650179.

[3] David P. DiVincenzo.
The Physical Implementation of Quantum Computation.
Fortschritte der Physik, 48(9-11):771–783, September 2000.
DOI: 10.1002/1521-3978(200009)48:9/11<771::AID-PROP771>3.0.CO;2-E.

[4] David P. DiVincenzo.
Two-bit gates are universal for quantum computation.
Physical Review A, 51(2):1015–1022, February 1995.
DOI: 10.1103/PhysRevA.51.1015.

[5] Jerry M Chow, Jay M Gambetta, A. D Corcoles, Seth T Merkel, John A Smolin, Chad Rigetti, S. Poletto, George A Keefe, Mary B Rothwell, J. R Rozen, Mark B Ketchen, and M. Steffen.
Complete universal quantum gate set approaching fault-tolerant thresholds with superconducting qubits.
arXiv:1202.5344, February 2012.

[6] M. Saffman, T. G. Walker, and K. Mølmer.
Quantum information with Rydberg atoms.
Reviews of Modern Physics, 82(3):2313, 2010.
DOI: 10.1103/RevModPhys.82.2313.

[7] John J. L. Morton, Dane R. McCamey, Mark A. Eriksson, and Stephen A. Lyon.
Embracing the quantum limit in silicon computing.

Nature, 479(7373):345–353, November 2011.
DOI: 10.1038/nature10681.

[8] Gavin K Brennen, Guido Pupillo, Ana Maria Rey, Charles W Clark, and Carl J Williams.
Scalable register initialization for quantum computing in an optical lattice.
Journal of Physics B: Atomic, Molecular and Optical Physics, 38(11):1687–1694, June 2005.
DOI: 10.1088/0953-4075/38/11/010.

[9] H.-J. Briegel, T. Calarco, D. Jaksch, J. I. Cirac, and P. Zoller.
Quantum computing with neutral atoms.
Journal of Modern Optics, 47(2-3):415–451, February 2000.
DOI: 10.1080/09500340008244052.

[10] Antonio Negretti, Philipp Treutlein, and Tommaso Calarco.
Quantum computing implementations with neutral particles.
Quantum Information Processing, 10(6):721–753, December 2011.
DOI: 10.1007/s11128-011-0291-5.

[11] J. I. Cirac and P. Zoller.
Quantum Computations with Cold Trapped Ions.
Physical Review Letters, 74(20):4091, May 1995.
DOI: 10.1103/PhysRevLett.74.4091.

[12] D. J. Wineland, R. E. Drullinger, and F. L. Walls.
Radiation-Pressure Cooling of Bound Resonant Absorbers.
Physical Review Letters, 40(25):1639–1642, June 1978.
DOI: 10.1103/PhysRevLett.40.1639.

[13] W. Neuhauser, M. Hohenstatt, P. Toschek, and H. Dehmelt.
Optical-Sideband Cooling of Visible Atom Cloud Confined in Parabolic Well.
Physical Review Letters, 41(4):233–236, July 1978.
DOI: 10.1103/PhysRevLett.41.233.

[14] Steven Chu, L. Hollberg, J. E. Bjorkholm, Alex Cable, and A. Ashkin.
Three-dimensional viscous confinement and cooling of atoms by resonance radiation pressure.
Physical Review Letters, 55(1):48–51, July 1985.
DOI: 10.1103/PhysRevLett.55.48.

[15] J Dalibard and C Cohen-Tannoudji.
Atomic motion in laser light: connection between semiclassical and quantum descriptions.
Journal of Physics B: Atomic and Molecular Physics, 18(8):1661–1683, April 1985.
DOI: 10.1088/0022-3700/18/8/019.

[16] William D. Phillips and Harold J. Metcalf.

Cooling and Trapping Atoms.
Scientific American, 256(3):50–56, March 1987.
DOI: 10.1038/scientificamerican0387-50.

[17] D. J. Wineland and D. Leibfried.
Quantum information processing and metrology with trapped ions.
Laser Physics Letters, 8(3):175, March 2011.
DOI: 10.1002/lapl.201010125.

[18] R. Blatt and C. F. Roos.
Quantum simulations with trapped ions.
Nature Physics, 8(4):277–284, April 2012.
DOI: 10.1038/nphys2252.

[19] C. Monroe and J. Kim.
Scaling the Ion Trap Quantum Processor.
Science, 339(6124):1164–1169, August 2013.
DOI: 10.1126/science.1231298.

[20] D. J. Wineland, C. R. Monroe, W. M. Itano, D. Leibfried, B. E. King, and D. M. Meekhof.
Experimental Issues in Coherent Quantum-State Manipulation of Trapped Atomic Ions.
J. Res. NIST, 103(3):259, 1998.

[21] D. Kielpinski, C. Monroe, and D. J. Wineland.
Architecture for a large-scale ion-trap quantum computer.
Nature, 417(6890):709–711, June 2002.
DOI: 10.1038/nature00784.

[22] R. B. Blakestad, C. Ospelkaus, A. P. VanDevender, J. M. Amini, J. Britton, D. Leibfried, and D. J. Wineland.
High-Fidelity Transport of Trapped-Ion Qubits through an X-Junction Trap Array.
Physical Review Letters, 102(15):153002, April 2009.
DOI: 10.1103/PhysRevLett.102.153002.

[23] R. Bowler, J. Gaebler, Y. Lin, T. R. Tan, D. Hanneke, J. D. Jost, J. P. Home, D. Leibfried, and D. J. Wineland.
Coherent Diabatic Ion Transport and Separation in a Multizone Trap Array.
Physical Review Letters, 109(8):080502, August 2012.
DOI: 10.1103/PhysRevLett.109.080502.

[24] A. Walther, F. Ziesel, T. Ruster, S. T. Dawkins, K. Ott, M. Hettrich, K. Singer, F. Schmidt-Kaler, and U. Poschinger.
Controlling Fast Transport of Cold Trapped Ions.
Physical Review Letters, 109(8):080501, August 2012.
DOI: 10.1103/PhysRevLett.109.080501.

[25] Ludwig de Clercq, Hsiang-Yu Lo, Matteo Marinelli, David Nadlinger, Robin Oswald, Vlad Negnevitsky, Daniel Kienzler, Ben Keitch, and Jonathan P. Home.
Parallel transport quantum logic gates with trapped ions.
arXiv:1509.06624 [physics, physics:quant-ph], September 2015.

[26] J. Chiaverini, RB. Blakestade, J. Britton, JD. Jost, C. Langer, D. Leibfried, and DJ Wineland.
Surface-electrode architecture for ion-trap quantum information processing.
Quantum Information \& Computation, 5(6):419–439, 2005.

[27] S. Seidelin, J. Chiaverini, R. Reichle, J. J. Bollinger, D. Leibfried, J. Britton, J. H. Wesenberg, R. B. Blakestad, R. J. Epstein, D. B. Hume, W. M. Itano, J. D. Jost, C. Langer, R. Ozeri, N. Shiga, and D. J. Wineland.
Microfabricated Surface-Electrode Ion Trap for Scalable Quantum Information Processing.
Physical Review Letters, 96(25):253003, June 2006.
DOI: 10.1103/PhysRevLett.96.253003.

[28] J M Amini, H Uys, J H Wesenberg, S Seidelin, J Britton, J J Bollinger, D Leibfried, C Ospelkaus, A P VanDevender, and D J Wineland.
Toward scalable ion traps for quantum information processing.
New Journal of Physics, 12(3):033031, March 2010.
DOI: 10.1088/1367-2630/12/3/033031.

[29] D. L. Moehring, C. Highstrete, D. Stick, K. M. Fortier, R. Haltli, C. Tigges, and M. G. Blain.
Design, fabrication and experimental demonstration of junction surface ion traps.
New Journal of Physics, 13(7):075018, 2011.
DOI: 10.1088/1367-2630/13/7/075018.

[30] A. Friedenauer, H. Schmitz, J. T. Glueckert, D. Porras, and T. Schaetz.
Simulating a quantum magnet with trapped ions.
Nat Phys, 4(10):757–761, October 2008.
DOI: 10.1038/nphys1032.

[31] B. P. Lanyon, C. Hempel, D. Nigg, M. Müller, R. Gerritsma, F. Zähringer, P. Schindler, J. T. Barreiro, M. Rambach, G. Kirchmair, M. Hennrich, P. Zoller, R. Blatt, and C. F. Roos.
Universal Digital Quantum Simulation with Trapped Ions.
Science, 334(6052):57 –61, October 2011.
DOI: 10.1126/science.1208001.

[32] Ch Schneider, Diego Porras, and Tobias Schaetz.
Experimental quantum simulations of many-body physics with trapped ions.
Reports on Progress in Physics, 75(2):024401, February 2012.
DOI: 10.1088/0034-4885/75/2/024401.

[33] Rainer Blatt and David Wineland.
Entangled states of trapped atomic ions.
Nature, 453(7198):1008–1015, June 2008.
DOI: 10.1038/nature07125.

[34] I. M. Georgescu, S. Ashhab, and Franco Nori.
Quantum simulation.
Reviews of Modern Physics, 86(1):153–185, March 2014.
DOI: 10.1103/RevModPhys.86.153.

[35] D. Porras and J. I. Cirac.
Effective Quantum Spin Systems with Trapped Ions.
Physical Review Letters, 92(20):207901, May 2004.
DOI: 10.1103/PhysRevLett.92.207901.

[36] K. R. Brown, C. Ospelkaus, Y. Colombe, A. C. Wilson, D. Leibfried, and D. J. Wineland.
Coupled quantized mechanical oscillators.
Nature, 471(7337):196–199, 2011.
DOI: 10.1038/nature09721.

[37] M. Harlander, R. Lechner, M. Brownnutt, R. Blatt, and W. Hansel.
Trapped-ion antennae for the transmission of quantum information.
Nature, 471(7337):200–203, March 2011.
DOI: 10.1038/nature09800.

[38] A. C. Wilson, Y. Colombe, K. R. Brown, E. Knill, D. Leibfried, and D. J. Wineland.
Tunable spin-spin interactions and entanglement of ions in separate potential wells.
Nature, 512(7512):57–60, August 2014.
DOI: 10.1038/nature13565.

[39] Roman Schmied, Janus H Wesenberg, and Dietrich Leibfried.
Quantum simulation of the hexagonal Kitaev model with trapped ions.
New Journal of Physics, 13(11):115011, November 2011.
DOI: 10.1088/1367-2630/13/11/115011.

[40] Manuel Mielenz, Henning Kalis, Matthias Wittemer, Frederick Hakelberg, Roman Schmied, Matthew Blain, Peter Maunz, Dietrich Leibfried, Ulrich Warring, and Tobias Schaetz.
Freely configurable quantum simulator based on a two-dimensional array of individually trapped ions.
arXiv:1512.03559 [physics, physics:quant-ph], December 2015.

[41] C. D. Bruzewicz, R. McConnell, J. Chiaverini, and J. M. Sage.
Scalable Loading of a Two-Dimensional Trapped-Ion Array.
arXiv:1511.03293 [physics, physics:quant-ph], November 2015.

[42] D.F.V. James.
Quantum dynamics of cold trapped ions with application to quantum computation.
Applied Physics B: Lasers and Optics, 66(2):181–190, February 1998.
DOI: 10.1007/s003400050373.

[43] J. Chiaverini and W. E. Lybarger.
Laserless trapped-ion quantum simulations without spontaneous scattering using microtrap arrays.
Physical Review A, 77(2):022324, February 2008.
DOI: 10.1103/PhysRevA.77.022324.

[44] A. M. Steane.
Error Correcting Codes in Quantum Theory.
Physical Review Letters, 77(5):793–797, July 1996.
DOI: 10.1103/PhysRevLett.77.793.

[45] D. J Wineland, M. Barrett, J. Britton, J. Chiaverini, B. DeMarco, W. M Itano, B. Jelenković, C. Langer, D. Leibfried, V. Meyer, T. Rosenband, and T. Schätz.
Quantum information processing with trapped ions.
Philosophical Transactions of the Royal Society of London. Series A: Mathematical, Physical and Engineering Sciences, 361(1808):1349–1361, July 2003.
DOI: 10.1098/rsta.2003.1205.

[46] Florian Mintert and Christof Wunderlich.
Ion-Trap Quantum Logic Using Long-Wavelength Radiation.
Physical Review Letters, 87(25):257904, November 2001.
DOI: 10.1103/PhysRevLett.87.257904.

[47] C. Ospelkaus, C. E. Langer, J. M. Amini, K. R. Brown, D. Leibfried, and D. J. Wineland.
Trapped-Ion Quantum Logic Gates Based on Oscillating Magnetic Fields.
Physical Review Letters, 101(9):090502, 2008.
DOI: 10.1103/PhysRevLett.101.090502.

[48] Hans Dehmelt.
Experiments with an isolated subatomic particle at rest.
Reviews of Modern Physics, 62(3):525, July 1990.
DOI: 10.1103/RevModPhys.62.525.

[49] K. R. Brown, A. C. Wilson, Y. Colombe, C. Ospelkaus, A. M. Meier, E. Knill, D. Leibfried, and D. J. Wineland.
Single-qubit-gate error below 10^{-4} in a trapped ion.
Physical Review A, 84(3):030303, 2011.
DOI: 10.1103/PhysRevA.84.030303.

[50] T. P. Harty, D. T. C. Allcock, C. J. Ballance, L. Guidoni, H. A. Janacek, N. M. Linke, D. N. Stacey, and D. M. Lucas.
High-Fidelity Preparation, Gates, Memory, and Readout of a Trapped-Ion Quantum Bit.
Physical Review Letters, 113(22):220501, November 2014.
DOI: 10.1103/PhysRevLett.113.220501.

[51] C. Ospelkaus, U. Warring, Y. Colombe, K. R. Brown, J. M. Amini, D. Leibfried, and D. J. Wineland.
Microwave quantum logic gates for trapped ions.
Nature, 476(7359):181–184, 2011.
DOI: 10.1038/nature10290.

[52] U. Warring, C. Ospelkaus, Y. Colombe, R. Jördens, D. Leibfried, and D. J. Wineland.
Individual-Ion Addressing with Microwave Field Gradients.
Physical Review Letters, 110(17):173002, April 2013.
DOI: 10.1103/PhysRevLett.110.173002.

[53] D. P. L. Aude Craik, N. M. Linke, M. A. Sepiol, T. P. Harty, C. J. Ballance, D. N. Stacey, A. M. Steane, D. M. Lucas, and D. T. C. Allcock.
High-fidelity spatial addressing of Ca-43 qubits using near-field microwave control.
arXiv:1601.02696 [physics, physics:quant-ph], January 2016.

[54] Q. A. Turchette, Kielpinski, B. E. King, D. Leibfried, D. M. Meekhof, C. J. Myatt, M. A. Rowe, C. A. Sackett, C. S. Wood, W. M. Itano, C. Monroe, and D. J. Wineland.
Heating of trapped ions from the quantum ground state.
Physical Review A, 61(6):063418, May 2000.
DOI: 10.1103/PhysRevA.61.063418.

[55] L. Deslauriers, S. Olmschenk, D. Stick, W. K. Hensinger, J. Sterk, and C. Monroe.
Scaling and Suppression of Anomalous Heating in Ion Traps.
Physical Review Letters, 97(10):103007, 2006.
DOI: 10.1103/PhysRevLett.97.103007.

[56] Jaroslaw Labaziewicz, Yufei Ge, Paul Antohi, David Leibrandt, Kenneth R. Brown, and Isaac L. Chuang.
Suppression of Heating Rates in Cryogenic Surface-Electrode Ion Traps.
Physical Review Letters, 100(1):013001, January 2008.
DOI: 10.1103/PhysRevLett.100.013001.

[57] Shannon X. Wang, Jaroslaw Labaziewicz, Yufei Ge, Ruth Shewmon, and Isaac L. Chuang.
Demonstration of a quantum logic gate in a cryogenic surface-electrode ion trap.

Physical Review A, 81(6):062332, June 2010.
DOI: 10.1103/PhysRevA.81.062332.

[58] J. Chiaverini and J. M. Sage.
Insensitivity of the rate of ion motional heating to trap-electrode material over a large temperature range.
Physical Review A, 89(1):012318, January 2014.
DOI: 10.1103/PhysRevA.89.012318.

[59] D T C Allcock, L Guidoni, T P Harty, C J Ballance, M G Blain, A M Steane, and D M Lucas.
Reduction of heating rate in a microfabricated ion trap by pulsed-laser cleaning.
New Journal of Physics, 13(12):123023, December 2011.
DOI: 10.1088/1367-2630/13/12/123023.

[60] D. A. Hite, Y. Colombe, A. C. Wilson, K. R. Brown, U. Warring, R. Jördens, J. D. Jost, K. S. McKay, D. P. Pappas, D. Leibfried, and D. J. Wineland.
100-Fold Reduction of Electric-Field Noise in an Ion Trap Cleaned with In Situ Argon-Ion-Beam Bombardment.
Physical Review Letters, 109(10):103001, September 2012.
DOI: 10.1103/PhysRevLett.109.103001.

[61] K. S. McKay, D. A. Hite, Y. Colombe, R. Jördens, A. C. Wilson, D. H. Slichter, D. T. C. Allcock, D. Leibfried, D. J. Wineland, and D. P. Pappas.
Ion-trap electrode preparation with Ne+ bombardment.
arXiv:1406.1778 [physics, physics:quant-ph], June 2014.

[62] M. Brownnutt, M. Kumph, P. Rabl, and R. Blatt.
Ion-trap measurements of electric-field noise near surfaces.
arXiv:1409.6572 [quant-ph], September 2014.

[63] N. Daniilidis, S. Gerber, G. Bolloten, M. Ramm, A. Ransford, E. Ulin-Avila, I. Talukdar, and H. Häffner.
Surface noise analysis using a single-ion sensor.
Physical Review B, 89(24), June 2014.
DOI: 10.1103/PhysRevB.89.245435.

[64] C. D. Bruzewicz, J. M. Sage, and J. Chiaverini.
Measurement of ion motional heating rates over a range of trap frequencies and temperatures.
Physical Review A, 91(4), April 2015.
DOI: 10.1103/PhysRevA.91.041402.

[65] Muir Kumph, Carsten Henkel, Peter Rabl, Michael Brownnutt, and Rainer Blatt.
Electric-field noise above a thin dielectric layer on metal electrodes.
New Journal of Physics, 18(2):023020, February 2016.

DOI: 10.1088/1367-2630/18/2/023020.

[66] Klaus Mølmer and Anders Sørensen.
Multiparticle Entanglement of Hot Trapped Ions.
Physical Review Letters, 82(9):1835, March 1999.
DOI: 10.1103/PhysRevLett.82.1835.

[67] E. Solano, R. L. de Matos Filho, and N. Zagury.
Deterministic Bell states and measurement of the motional state of two trapped ions.
Physical Review A, 59(4):R2539, April 1999.
DOI: 10.1103/PhysRevA.59.R2539.

[68] Anders Sørensen and Klaus Mølmer.
Quantum Computation with Ions in Thermal Motion.
Physical Review Letters, 82(9):1971–1974, March 1999.
DOI: 10.1103/PhysRevLett.82.1971.

[69] D. T. C. Allcock, T. P. Harty, C. J. Ballance, B. C. Keitch, N. M. Linke, D. N. Stacey, and D. M. Lucas.
A microfabricated ion trap with integrated microwave circuitry.
Applied Physics Letters, 102(4):044103–044103–4, January 2013.
DOI: doi:10.1063/1.4774299.

[70] Wolfgang Paul.
Electromagnetic traps for charged and neutral particles.
Reviews of Modern Physics, 62(3):531–542, 1990.

[71] J. R. Castrejón-Pita and R. C. Thompson.
Proposal for a planar Penning ion trap.
Physical Review A, 72(1):013405, July 2005.
DOI: 10.1103/PhysRevA.72.013405.

[72] S. Stahl, F. Galve, J. Alonso, S. Djekic, W. Quint, T. Valenzuela, J. Verdú, M. Vogel, and G. Werth.
A planar Penning trap.
The European Physical Journal D, 32(1):8, 2005.
DOI: 10.1140/epjd/e2004-00179-x.

[73] F. Galve and G. Werth.
Confinement study in a planar Penning trap.
AIP Conference Proceedings, 862(1):313–318, October 2006.
DOI: doi:10.1063/1.2387938.

[74] J Verdú.
Theory of the coplanar-waveguide Penning trap.
New Journal of Physics, 13(11):113029, November 2011.
DOI: 10.1088/1367-2630/13/11/113029.

[75] Samuel Earnshaw.

On the nature of the molecular forces which regulate the constitution of the luminiferous ether.
Trans. Camb. Phil. Soc, 7:97–112, 1842.

[76] D. Leibfried, R. Blatt, C. Monroe, and D. Wineland.
Quantum dynamics of single trapped ions.
Reviews of Modern Physics, 75(1):281, March 2003.
DOI: 10.1103/RevModPhys.75.281.

[77] Gaston Floquet.
Sur les équations différentielles linéaires à coefficients périodiques.
In *Annales scientifiques de l'École normale supérieure*, volume 12, pages 47–88, 1883.

[78] H.G. Dehmelt.
Radiofrequency Spectroscopy of Stored Ions I: Storage.
In *Advances in Atomic and Molecular Physics*, volume 3, pages 53–72. Elsevier, 1968.

[79] P. K. Ghosh.
Ion Traps.
Clarendon, Oxford, UK, 1995.

[80] Fayaz A. Shaikh and Arkadas Ozakin.
Stability analysis of ion motion in asymmetric planar ion traps.
Journal of Applied Physics, 112(7):074904, 2012.
DOI: 10.1063/1.4752404.

[81] J. H. Wesenberg.
Electrostatics of surface-electrode ion traps.
Physical Review A, 78(6):063410, December 2008.
DOI: 10.1103/PhysRevA.78.063410.

[82] W. S. Hall.
Boundary Element Method.
In G. M. L. Gladwell, editor, *The Boundary Element Method*, volume 27, pages 61–83. Springer Netherlands, Dordrecht, 1994.

[83] Klaus-Juergen Bathe and Edward L. Wilson.
Numerical Methods in Finite Element Analysis.
Prentice-Hall, 1976.

[84] Mário H Oliveira and José A Miranda.
Biot-Savart-like law in electrostatics.
European Journal of Physics, 22:31, 2001.
DOI: 10.1088/0143-0807/22/1/304.

[85] John David Jackson.
Classical electrodynamics.
Wiley, New York, 3rd ed edition, 1999.

[86] Roman Schmied.
Electrostatics of gapped and finite surface electrodes.
New Journal of Physics, 12(2):023038, February 2010.
DOI: 10.1088/1367-2630/12/2/023038.

[87] C. Langer, R. Ozeri, J. D. Jost, J. Chiaverini, B. DeMarco, A. Ben-Kish, R. B. Blakestad, J. Britton, D. B. Hume, W. M. Itano, D. Leibfried, R. Reichle, T. Rosenband, T. Schaetz, P. O. Schmidt, and D. J. Wineland.
Long-Lived Qubit Memory Using Atomic Ions.
Physical Review Letters, 95(6):060502, 2005.
DOI: 10.1103/PhysRevLett.95.060502.

[88] Theo Mayer-Kuckuk.
Atomphysik.
Teubner, Stuttgart, 1997.

[89] M. Wahnschaffe, H. Hahn, G. Zarantonello, T. Dubielzig, S. Grondkowski, A. Bautista-Salvador, M. Kohnen, and C. Ospelkaus.
Exploring and understanding 2d microwave near-fields using a single ion.
arXiv:1601.06460 [physics, physics:quant-ph], January 2016.

[90] J. J. Bollinger, J. S. Wells, D. J. Wineland, and Wayne M. Itano.
Hyperfine structure of the $2p^2P_{\frac{1}{2}}$ state in $^9Be^+$.
Physical Review A, 31(4):2711–2714, April 1985.
DOI: 10.1103/PhysRevA.31.2711.

[91] Mariusz Puchalski and Krzysztof Pachucki.
Fine and hyperfine splitting of the $2p$ state in Li and Be^+.
Physical Review A, 79(3):032510, March 2009.
DOI: 10.1103/PhysRevA.79.032510.

[92] D. M. Harber, H. J. Lewandowski, J. M. McGuirk, and E. A. Cornell.
Effect of cold collisions on spin coherence and resonance shifts in a magnetically trapped ultracold gas.
Physical Review A, 66(5):053616, November 2002.
DOI: 10.1103/PhysRevA.66.053616.

[93] Chu Xin-zhao, Liu Shu-qin, and Dong Tai-qian.
Experimental study of ac zeeman effect in ^{87} Rb atomic frequency standard.
Acta Physica Sinica (Overseas Edition), 5(6):423–430, June 1996.
DOI: 10.1088/1004-423X/5/6/003.

[94] M. Carsjens, M. Kohnen, T. Dubielzig, and C. Ospelkaus.
Surface-electrode Paul trap with optimized near-field microwave control.
Applied Physics B, 114(1-2):243–250, 2014.
DOI: 10.1007/s00340-013-5689-6.

[95] U. Warring, C. Ospelkaus, Y. Colombe, K. R. Brown, J. M. Amini, M. Carsjens, D. Leibfried, and D. J. Wineland.

Techniques for microwave near-field quantum control of trapped ions.
Physical Review A, 87(1):013437, January 2013.
DOI: 10.1103/PhysRevA.87.013437.

[96] P F Herskind, A Dantan, M Albert, J P Marler, and M Drewsen.
Positioning of the rf potential minimum line of a linear Paul trap with micrometer precision.
Journal of Physics B: Atomic, Molecular and Optical Physics, 42(15):154008, August 2009.
DOI: 10.1088/0953-4075/42/15/154008.

[97] Tony Hyun Kim, Peter F. Herskind, and Isaac L. Chuang.
Surface-electrode ion trap with integrated light source.
Applied Physics Letters, 98(21):214103, 2011.
DOI: 10.1063/1.3593496.

[98] Muir Kumph, Philip Holz, Kirsten Langer, Michael Niedermayr, Michael Brownnutt, and Rainer Blatt.
Operation of a planar-electrode ion trap array with adjustable RF electrodes.
arXiv:1402.0791 [physics, physics:quant-ph], February 2014.

[99] Brian C Wadell.
Transmission line design handbook.
Artech House Publishers, 1991.

[100] David M Pozar.
Microwave engineering.
John Wiley & Sons, 2009.

[101] Philipp Treutlein.
Coherent manipulation of ultracold atoms on atom chips.
PhD thesis, Ludwig-Maximilians-Universität München, 2008.

[102] T. Yu. Chemekova, O. V. Avdeev, I. S. Barash, E. N. Mokhov, S. S. Nagalyuk, A. D. Roenkov, A. S. Segal, Yu. N. Makarov, M. G. Ramm, S. Davis, G. Huminic, and H. Helava.
Sublimation growth of 2 inch diameter bulk AlN crystals.
physica status solidi (c), 5(6):1612–1614, May 2008.
DOI: 10.1002/pssc.200778534.

[103] Christopher E. Langer.
High Fidelity Quantum Information Processing with Trapped Ions.
PhD Thesis, University of Colorado, Boulder, Colorado, 2006.

[104] Sebastian Grondkowski.
Quantenkontrolle von $^9Be^+$ Hyperfein-Qubits.
Master's Thesis, Gottfried Wilhelm Leibniz Universität Hannover, Hannover, 2014.

[105] R. J. Hendricks, D. M. Grant, P. F. Herskind, A. Dantan, and M. Drewsen.
An all-optical ion-loading technique for scalable microtrap architectures.
Applied Physics B, 88(4):507–513, June 2007.
DOI: 10.1007/s00340-007-2698-3.

[106] Hsiang-Yu Lo, Joseba Alonso, Daniel Kienzler, Benjamin C. Keitch, Ludwig E. de Clercq, Vlad Negnevitsky, and Jonathan P. Home.
All-solid-state continuous-wave laser systems for ionization, cooling and quantum state manipulation of beryllium ions.
Applied Physics B, 114(1-2):17–25, September 2013.
DOI: 10.1007/s00340-013-5605-0.

[107] R. W. P. Drever, J. L. Hall, F. V. Kowalski, J. Hough, G. M. Ford, A. J. Munley, and H. Ward.
Laser phase and frequency stabilization using an optical resonator.
Applied Physics B, 31(2):97–105, June 1983.
DOI: 10.1007/BF00702605.

[108] A. C. Wilson, C. Ospelkaus, A. P. VanDevender, J. A. Mlynek, K. R. Brown, D. Leibfried, and D. J. Wineland.
A 750-mW, continuous-wave, solid-state laser source at 313 nm for cooling and manipulating trapped $^{9}Be^{+}$ ions.
Applied Physics B, 105(4):741–748, October 2011.
DOI: 10.1007/s00340-011-4771-1.

[109] T.W. Hänsch and B. Couillaud.
Laser frequency stabilization by polarization spectroscopy of a reflecting reference cavity.
Optics Communications, 35(3):441–444, December 1980.
DOI: 10.1016/0030-4018(80)90069-3.

[110] F. Gebert, M. H. Frosz, T. Weiss, Y. Wan, A. Ermolov, N. Y. Joly, P. O. Schmidt, and P. St. J. Russell.
Damage-free single-mode transmission of deep-UV light in hollow-core PCF.
Optics Express, 22(13):15388, June 2014.
DOI: 10.1364/OE.22.015388.

[111] Yves Colombe, Daniel H. Slichter, Andrew C. Wilson, Dietrich Leibfried, and David J. Wineland.
Single-mode optical fiber for high-power, low-loss UV transmission.
Optics Express, 22(16):19783, August 2014.
DOI: 10.1364/OE.22.019783.

[112] Sebastian Grondkowski.
Pulsgenerator für die Quanteninformationsverarbeitung mit einzelnen gespeicherten Ionen.
Bachelor's Thesis, Gottfried Wilhelm Leibniz Universität Hannover, Hannover, 2012.

[113] C.E. Shannon.
Communication in the Presence of Noise.
Proceedings of the IRE, 37(1):10–21, January 1949.
DOI: 10.1109/JRPROC.1949.232969.

[114] R. Bowler, U. Warring, J. W. Britton, B. C. Sawyer, and J. Amini.
Arbitrary waveform generator for quantum information processing with trapped ions.
Review of Scientific Instruments, 84(3):033108–033108–6, March 2013.
DOI: doi:10.1063/1.4795552.

[115] Ryan Bowler.
Coherent Ion Transport in a Multi-electrode Trap Array.
PhD thesis, University of Colorado, 2015.

[116] Muir Kumph, Michael Brownnutt, and Rainer Blatt.
Two-dimensional arrays of radio-frequency ion traps with addressable interactions.
New Journal of Physics, 13(7):073043, July 2011.
DOI: 10.1088/1367-2630/13/7/073043.

[117] Pascal Böhi, Max F. Riedel, Theodor W. Hänsch, and Philipp Treutlein.
Imaging of microwave fields using ultracold atoms.
Applied Physics Letters, 97(5):051101, 2010.
DOI: 10.1063/1.3470591.

[118] Jürgen Eschner, Giovanna Morigi, Ferdinand Schmidt-Kaler, and Rainer Blatt.
Laser cooling of trapped ions.
Journal of the Optical Society of America B, 20(5):1003–1015, May 2003.
DOI: 10.1364/JOSAB.20.001003.

[119] C. J. Foot.
Atomic Physics.
Oxford Master Series in Atomic, Optical and Laser Physics. Oxford University Press, Oxford, 2005.

[120] F. Diedrich, J. C. Bergquist, Wayne M. Itano, and D. J. Wineland.
Laser Cooling to the Zero-Point Energy of Motion.
Physical Review Letters, 62(4):403, January 1989.
DOI: 10.1103/PhysRevLett.62.403.

[121] Y. Ibaraki, U. Tanaka, and S. Urabe.
Detection of parametric resonance of trapped ions for micromotion compensation.
Applied Physics B, 105(2):219–223, March 2011.
DOI: 10.1007/s00340-011-4463-x.

[122] I. I. Rabi, N. F. Ramsey, and J. Schwinger.

Use of Rotating Coordinates in Magnetic Resonance Problems.
Reviews of Modern Physics, 26(2):167–171, April 1954.
DOI: 10.1103/RevModPhys.26.167.

[123] D. R. Leibrandt, J. Labaziewicz, R. J. Clark, I. L. Chuang, R. J. Epstein, C. Ospelkaus, J. H. Wesenberg, J. J. Bollinger, D. Leibfried, D. J. Wineland, D. Stick, J. Sterk, C. Monroe, C.-S. Pai, Y. Low, R. Frahm, and R. E. Slusher.
Demonstration of a scalable, multiplexed ion trap for quantum information processing.
Quantum Information & Computation, 11 & 12:0901, 2009.

[124] M. Trinker, S. Groth, S. Haslinger, S. Manz, T. Betz, S. Schneider, I. Bar-Joseph, T. Schumm, and J. Schmiedmayer.
Multilayer atom chips for versatile atom micromanipulation.
Applied Physics Letters, 92(25):254102, 2008.
DOI: 10.1063/1.2945893.

[125] Ho-Chiao Chuang, Evan A. Salim, Vladan Vuletic, Dana Z. Anderson, and Victor M. Bright.
Multi-layer atom chips for atom tunneling experiments near the chip surface.
Sensors and Actuators A: Physical, 165(1):101–106, January 2011.
DOI: 10.1016/j.sna.2010.01.003.

[126] Marcus D. Hughes, Bjoern Lekitsch, Jiddu A. Broersma, and Winfried K. Hensinger.
Microfabricated ion traps.
Contemporary Physics, pages 1–25, September 2011.
DOI: 10.1080/00107514.2011.601918.

[127] R. C. Sterling, H. Rattanasonti, S. Weidt, K. Lake, P. Srinivasan, S. C. Webster, M. Kraft, and W. K. Hensinger.
Fabrication and operation of a two-dimensional ion-trap lattice on a high-voltage microchip.
Nature Communications, 5:3637, April 2014.
DOI: 10.1038/ncomms4637.

List of Figures

List of Tables

List of publications

- U. Warring, C. Ospelkaus, Y. Colombe, K. R. Brown, J. M. Amini, M. Carsjens, D. Leibfried, and D. J. Wineland.
  Techniques for microwave near-field quantum control of trapped ions.
  Physical Review A, 87(1):013437, January 2013.
  DOI: 10.1103/PhysRevA.87.013437.
- M. Carsjens, M. Kohnen, T. Dubielzig, and C. Ospelkaus.
  Surface-electrode Paul trap with optimized near-field microwave control
  Applied Physics B, 114(1-2):243–250, 2014.
  DOI: 10.1007/s00340-013-5689-6.
- M. Wahnschaffe, H. Hahn, G. Zarantonello, T. Dubielzig, S. Grondkowski, A. Bautista-Salvador, M. Kohnen, and C. Ospelkaus.
  Exploring and understanding 2d microwave near-fields using a single ion.
  arXiv:1601.06460 [physics, physics:quant-ph], January 2016.

Acknowledgements

Without the help and guidance of a lot of people, this work would not have been possible.
First, I would like to thank my advisor Christian Ospelkaus, who gave me the opportunity to work in the vibrant and lively scientific research area of quantum information and quantum simulation. Christian, thanks for the faith and the support during the last 5 years. It was a pleasure working with and for you.
I would like to express my sincere gratitude to Piet O. Schmidt, not only for being my second referee, but also for the help and encouragement during my time at PTB. Thanks for letting me and my Hannover colleagues being part of the QUEST group. I'm looking back to a great time with lots of fun activities, fruitful discussions and advice, and too many cakes. Thanks also to all members of Piet's and Tanja's group, especially to Jonas Keller, Sana Amairi Pyka, and Heather Partner.
Starting as an engineer, the world of quantum physics was something I had only a rough idea about. However, Christian and especially Timko Dubielzig, Malte Niemann, Torben Schulze, and Matthias Kohnen helped me through a tough time of understanding the physics behind our and other quantum simulation and information projects. I really appreciate all of your effort trying to teach me physics, for example in a café in Paris.
My special thanks go to both of my Post-Docs Matthias Kohnen and Amado Bautista-Salvador. Without Matthias the experiment would not be where it is now. Thanks for setting up the laser systems, the immense help with the vacuum chamber and letting me in the colourful world of simulations while you were fixing "lab problems". Without your support I would not have had the time to tackle the simulations in such a detail. I will never forget our time in the lab, desperately trying to trap an ion or taking "gradmaps" while slowly getting crazy. I properly ruined "What shall we do with the drunken sailor?" for you for all times. Amado brought the multi-layer process to our group, which is for me one of the most interesting projects for the future. Amado, thanks a lot for your support, guidance and the fun in and out of the clean room. Without you we would have never pushed the fabrication to such a high level. Thank you both for being great friends and colleagues.
I want to thank everyone involved in this project: Timko Dubielzig and Sebastian Grondkowski for all their support and contributions in terms of electronics, the vacuum chamber, field coils and imaging; Henning Hahn and Giorgio Zarantonello for taking over the experiment and all their help and contributions during the last

months of this work, especially for taking “just” a few more “gradmaps”. I wish them the best for the future, in particular for going towards high-fidelity gates.
Thanks to David Allcock, Marcus Laudin and Jörg Schöbel for the support and advice considering the numerical simulations.
Furthermore, I want to thank the staff at the PTB clean room facility and at the LNQE for their support. In particular I want to thank Thomas Weimann, Peter Hinze, Rüdiger Wendisch, Brigitte Mackrodt and Kathrin Störr for a special and refreshing time.
Thanks to all members of the machine shop at PTB and at the Institut für Quantenoptik for the support and for dealing with all our special requirements.
I thank Jörg Schöbel and Karsten Schubert for a productive cooperation towards an impedance matching network and their help measuring the S-parameters at the Institut für Hochfrequenztechnik.
Thanks to Matthias, Henning, Giorgio, Timko, Amado and in particular to Heather Partner for reviewing this manuscript. I really appreciate that all of you spent so much time reading and correcting this work. It helped me a lot.
I also want to thank all members of the Ospelkaus’ groups and Erik Schwanke for a great time. It was a pleasure being part of your group and spending time with you guys. AGP and Matthias Gempel, thanks for being such good friends in the last years and for listing me whining about being a PhD student.
I want to thank everyone in the group of Wolfgang Ertmer, Carsten Klempt and Ernst Rasel for a great time, and helpful discussions, in particular Stephan Tobias Seidel with whom I set up the fabrication process at PTB and LNQE.
Big thanks go to Sandra Ludwig and the secretaries at the IQ in Hannover for the support, help and asked-for distractions.
Besides physics, thanks to all my friends for a great time in Braunschweig, Hannover and Berlin and for your understanding during the last year of this work.
I would like to express my deepest gratitude to my husband, Martin, without whom, I would have gone insane in the last few months. Thanks for everything, especially for being there whenever I need you.
Last but not least, I would like to thank my parents and my stepfather. Ich kann nicht in Worte fassen, wie dankbar ich Euch bin, dass Ihr mir diesen Weg bereitet habt. Ohne Eure Unterstützung und Euren Glauben an mich wäre all dies nicht möglich gewesen. Ich möchte mich an dieser Stelle nochmal ausdrücklich dafür bedanken, dass Ihr es mir trotz aller Umstände ermöglicht habt in Braunschweig zu studieren und meinen eigenen Weg zu gehen. Es war mir immer eine Freude Euch zu erklären, was ich denn nun eigentlich genau mache. Dank auch an meine Brüder und meine Großeltern, die immer für mich da waren. Opa, ich würde auch als Doktor noch mit Dir reden.

Martina Wahnschaffe

née Carsjens
Herrendorftwete 1
38100 Braunschweig

Research

May 2011 - June 2016

Doctoral Studies

Leibniz Universität Hannover
Institut für Quantenoptik
PhD student in the group of Prof. Dr. Christian Ospelkaus

- Engineered Microwave Control for Trapped Ions

University

Oct. 2005 - Jan. 2011

Diplom Elektrotechnik

Technische Universität Braunschweig
Institut für Halbleitertechnik
Diploma thesis in the group of Prof. Dr. Andreas Waag, realized in the group of Prof. Steven Cundiff at Jila, Boulder, CO, USA

- Implementation of crossed-beam interferometry for 2DFT spectroscopy

"Studienarbeit" in the group of Prof. Dr. Andreas Waag

- Modellierung modengekoppelter Halbleiterscheibenlaser

School

Aug. 1998 - June 2005

Abitur

Gymnasium am Treckfahrtstief, Emden